Simulation of Wave Spray Cloud

By © **Armin Bodaghkhani**

A thesis submitted to the School of Graduate Studies in partial fulfillment of the requirements for the degree of

Doctor of Philosophy in Mechanical Engineering

Department of Mechanical Engineering/Faculty of Engineering and Applied Science

Memorial University of Newfoundland

May 2018

St. John's - Newfoundland and Labrador

Abstract

Wave impacts on vessels and offshore structures can induce significant spray. This process leads to topside icing in sufficiently cold and windy conditions. This study establishes the current state of the art understanding of the physical behavior of wave impact and the process of spray cloud formation upstream of a ship or marine structure. The process of spray formation is related to several complicated phenomena including wave slamming, jet formation after impact, sheet and droplet breakup, and production of the spray cloud on the top surface of the ship bow. The process of spray-cloud production and flow kinematics arising from breaking wave impact on a lab-scaled model is investigated using the Bubble Image Velocimetry (BIV) method to measure the wave run-up velocity. In addition to the BIV method, spray characteristics were examined using the Digital Particle Image Velocimetry (DPIV) method. Measurements of droplet size, and velocity, as well as wave run-up velocity, were major elements of this study. Progress has been made in modeling wave spray phenomena, including numerical methods for modeling the free surface, and consideration of slamming, air entrainment, and water breakup. Further, the interaction of single nonlinear wave with a solid vertical surface was numerically simulated in three dimensions. Complex behavior of the wave impact as well as the resulting water sheet and high-speed jet were captured in the numerical model. The maximum wave run-up velocity, instant wave run-up velocity in front of the vertical surface, the break-up length of the water sheet, and the maximum impact pressure were all computed for several input wave characteristics. In addition to the experimental and

numerical work, conservation constraints that govern the flow behavior, which is important in the process of spray cloud formation resulting from wave impact, were developed. The size and velocity distribution of spray droplets arising from the maximization of the entropy is subject to these constraints. The prediction is based on a statistical tool called the Maximum Entropy Principle (MEP), and the resulting droplet size distribution is in agreement with the general empirical distributions. The prediction distribution applied to both one- and two-dimensional cases. Finally, four stages of wave spray production are added together to produce a more comprehensive analytical model for predicting the final average droplet diameter from the information related to the inlet wave conditions. These mathematical stages are; 1) the formulation of wave impact velocities based on the input wave characteristics, 2) the formulation of air entrapment at the moment of impact based on the Bagnold-Mitsuyasu scaling law, which calculates the maximum impact pressure, 3) a mathematical relationship between the maximum wave impact pressure and the maximum wave run-up velocities, and finally, 4) the breakup phenomena.

Acknowledgments

I would like to gratefully acknowledge the joint financial support of Statoil (Norway), MITACS, American Bureau of Shipping (ABS), and Petroleum Research Newfoundland & Labrador (PRNL) with the grant number IT03198.

The experiment was carried out in the tow tank located in the Ocean Engineering Research Centre of the Memorial University of Newfoundland, and I gratefully appreciate the faculty and staff for their cooperation during the experiment. The numerical simulation was accomplished on the ACENET platform, and I am grateful for all the staff for their help during the parallel computing simulations. I'm also grateful to Dr. Ronald Haynes and Dr. Scott MacLachlan for their guidance and advice concerning the MEP methods' mathematical procedures.

I would like to express my heartfelt gratitude to my supervisors: Dr. Yuri S. Muzychka and Dr. Bruce Colbourne for the continuous support of my Ph.D. study and related research, for their patience, motivation, and immense knowledge. Their guidance helped me in all the time of research and writing of this thesis. I could not have imagined having better advisors and mentors for my Ph.D. study. Besides my advisors, I would like to thank Dr. Kevin Pope of my thesis committee, for his insightful comments and encouragement.

Last but not the least, I would like to thank my family: my wife and my parents for supporting me spiritually throughout writing this thesis and my life in general.

Table of Contents

List of Figures

List of Tables

Nomenclature

Chapter 1

w	kg/m^3	LWC
ξ	$\mathrm{kg/m^4}$	Constant equal to 10^{-3}
α	°	Heading angle
h	m	Elevation of an object above the deck of the MFV
H	m	Wave height
V_r	m/s	Ship speed relative to a wave
H_0	m	Wave height from the Borisenkov and Pichelko (1975)
V_0	m/s	Ship speed relative to the wave from the Borisenkov and Pichelko (1975)
V_s	m/s	Ship speed in knots
T_w	$1/s$	Period of the wave
α	°	Heading angle,
z	m	Elevation above sea level.
$\bar{H}$	m	Mean wave height
h'	m	Height of the bulwark (0.75 m)
V_w	m/s	Wave speed
Z_{max}	m	Maximum height of the spray with respect to the ship deck
a	$-$	Empirical constant
c	$-$	Empirical constant based on the shape and size of the ship hull
U_{10}	m/s	Wind speed
Δt	s	Total duration of the spray cloud
K_1	$-$	Empirical constants.
K_2	$-$	Empirical constants.
$H_{1/3}$	m	Significant wave height
τ_{per}	$1/s$	Wave period
τ_{dur}	s	Duration of spray events
ρ_w	kg/m^3	Water density
A	$-$	Non-dimensional constant, dependent on the relative wind
B	$-$	Non-dimensional constant, dependent on the relative wind
α	°	Spray heading angle
W	m/s	Vessel speed.
u	m/s	Horizontal (x) velocity component
w	m/s	Vertical (z) velocity components

τ	$1/s$	Wave period
k	$1/m$	Wavenumber
z	m	Wave amplitude of the wave at zero force
θ	°	Phase angle of the wave at zero force
C	m/s	Wave celerity
z_r	m	Wave run-up height at maximum force
t_r	s	Rise-time of the force
$F(x, y, t)$	$-$	Fluid fraction function
p_{max}	Pa	Maximum pressure
T	$1/s$	Wave period
c_b	m/s	Wave phase speed
λ	s^{-1}	Constant parameter
Eu	$-$	Euler number
Ka	$-$	Cavitation number
K	m	Initial amplitude of the impacting water wave
D	m	Diameter of the trapped air pocket
u_0	m/s	Fluid velocity
p_{ullage}	pa	Ullage pressure
p_v	pa	Vapour pressure
p_0	pa	Initial pressure
Bg	$-$	Bagnold Number
$\beta_0(x)$	$-$	Initial aeration

Chapter 2

H_t	m	Maximum depth of wave tank
H	m	Water depth
h_f	m	Plate model height
b_f	m	Plate model width
h_b	m	Bow model height
b_b	m	Bow model width
$O(0, 0, 0)$	$-$	Origin coordinates
T	$1/s$	Wave period
λ	m	Wavelength
g	m/s^2	Gravity acceleration
$U_{x,i}$	%	Uncertainties
V_c	m/s	Wave phase velocity
R	m	Nearest limit for camera aperture
S	m	Farthest limit for camera aperture
D	m	Depth of field (DOF)
ε	%	Error associated by the DOF
l	m	Distance between the camera and the center of the camera's focal plane

h	m	Free surface elevation
t	s	Time

Chapter 3

ρ	kg/m^3	Water density
$\vec{v}$	m/s	Three-dimensional velocity field
$x_i = (x, y, z)$	$-$	Three-dimensional space
T	s	Time
$\vec{g}$	m/s^2	Gravitational body force
$\vec{F}$	N	External body force
$\vec{\tau}$	N/m^2	Stress Tensor
ν	m^2/s	Kinematic viscosity
I	$-$	Unit tensor
ε	$J/(Kg \cdot s)$	Dissipation rate
G_k	J/m	Generation of turbulence kinetic energy
μ_t	$Pa \cdot s$	Turbulent viscosity
μ	$Pa \cdot s$	Viscosity
a_p	$-$	p^{th} fluid's volume fraction in the cell
φ	$-$	Level set function
d	m	Signed distance from the interface
ψ	$-$	Scalar quantity
$\vec{v}$	m/s	Velocity Vector
$\vec{A}$	m^2	Surface area vector
Γ_ψ	m^2/s	Diffusion coefficient for ψ
M_{faces}	$-$	The number of faces of the cell
ψ_h	$-$	The value of scalar ψ on face h
H	$-$	Specific quantity at the h^{th} cell
α_f	$-$	Linearized coefficient of ψ,
α_{nb}	$-$	Linearized coefficient of ψ_{nb}
nb	$-$	Neighboring cell.
$p + 1$	$-$	Symbol for the current time step
p	$-$	Previous time step
$a_{q,h}$	$-$	Face value of the q^{th} volume fraction
V	m^3	Volume of the cell
U_h	m^3/s	Volume flux through the cell h
a_{mn}	m	Variable functions of wavelength
b_{mn}	m	Variable functions of liquid heights
A	m	Wave amplitude
k	$1/m$	Wave number
ω	$1/s$	Wave frequency
h	m	Liquid depth.

S	$-$	Damping sink term
$\hat{z}$	$-$	Vertical direction
$\hat{x}$	$-$	Flow direction
C_1	$1/s$	Linear damping resistance coefficients
C_2	$1/m$	Quadratic damping resistance coefficients
x	m	Distance in the flow direction,
x_s	m	Start points of the damping zone in the $\hat{x}$ direction
x_e	m	Endpoints of the damping zone in the $\hat{x}$ direction
z	m	Distance from the free-surface level
z_{fs}	m	The free-surface level along the $\hat{z}$ direction
z_b	m	Bottom level along the $\hat{z}$ direction
V	m/s	Velocity along the $\hat{z}$ direction.

Chapter 4

f	$-$	Probability density function
D		Droplet diameter
V_d	m^3	Droplet volume
v_d	m/s	Droplet velocity
U_0	m/s	Average initial velocity of the water sheet at the moment of impact with the wall
D_{30}	m	Mass mean diameter of droplets
$\bar{S}_m$	$-$	Non-dimensional mass source term
C_D	$-$	Drag coefficient for flow over a flat plate
A_f	m^2	Flat plate area
A_d	m^2	Area of a spherical droplet with a constant size.
F	N	Drag force
$\dot{j}_0$	$kg \cdot m/s^2$	Initial momentum flow rate
L_b	m	Breakup length
t	m	Breakup thickness
b	m	Initial edge of the impact
c	m	Distributed edge of the water sheet
$\bar{S}_e$	$-$	Nondimensional sources of energy
H	$-$	Shape factor
We	$-$	Weber number
λ_{0-5}	$-$	Lagrange multipliers
N	$-$	Normalized droplet numbers
$\bar{S}_m$	$-$	Nondimensional mass source term
$\bar{S}_{ke}$	$-$	Nondimensional kinetic energy source term
η	m	Initial disturbance amplitude
D_{32}	m	Sauter mean diameter
Ω_r	rad/s	Real part of the dispersion relation

Chapter 5

k	$1/m$	Wavenumber
ξ_a	m	Wave amplitude
V_w	m/s	Wave velocity
L_w	m	Wavelength
T_w	s	Wave period
$\Psi(x, y, t)$	m/s	Velocity potential
d	m	Constant water depth of the undisturbed medium
ξ_a	m	Wave amplitude
p_0	Pa	Atmospheric pressure
ρ_w	kg/m^3	Density of unaerated water
V_0	m^3	Volume of the air pocket at atmospheric pressure
γ	$-$	Heat capacity ratio of air
u	m/s	Velocity magnitude at the moment of impact.
H_{m0}	m	Significant wave height
c_i	$-$	Impact coefficient
U_{max}	m/s	Maximum wave run-up velocity
F_p	N	Pressure force
F_σ	N	Surface tension force
F_I	N	Inertial force,
F_μ	N	Viscous force
h	m	Sheet thickness
τ	s	Break-up time
D_L	m	Ligament diameter
D_D	m	Final average droplet diameter
K	$-$	Spray parameter
τ_n	m	Sheet thickness at the moment of impact
W	m	Width of wave impact
σ	N/m	Water surface tension
μ	$Pa \cdot s$	Kinematic viscosity of water
ρ_a	kg/m^3	Air density

This chapter is written based on: Armin Bodaghkhani, Saeed-Reza Dehghani, Yuri S. Muzychka, Bruce Colbourne, Understanding spray cloud formation by wave impact on marine objects, In Cold Regions Science and Technology, Volume 129, 2016, Pages 114-136.

Chapter 1 Introduction

Offshore oil exploration and other developments in cold ocean regions are becoming more common. The safety and security of fixed and floating platforms and vessels in these regions are receiving increased industry attention. Understanding the problem of marine icing, one of the environmental hazards, is important. The effect of icing on shipping and offshore exploration and production has been well documented (Roebber and Mitten, 1987; Lozowski and Zakrzewski, 1993; Ryerson, 2013). Studies show that icing in Arctic conditions on offshore structures and vessels arises from two major causes, categorized as atmospheric conditions and sea-water spray (Brown and Roebber 1985). The sea-water spray is produced in two different ways, from wind and waves. Wind spray is a spray cloud drawn from the sea surface by wind, and wave spray is the upstream spray cloud caused by a wave impact on a vessel's bow or marine structure. More than 3000 observations from ships in different sea conditions show that more than 90 percent of icing on vessels results from wave spray (Borisenkov and Pichelko, 1975). Wave spray is produced after the impact of vessels with waves, and this impact produces a cloud of water, which leads to impingement of droplets on the ship's deck and bow. In cold conditions, these droplets turn into ice, which is a hazard to crew operations and to vessel stability. Similar effects are observed in offshore structures.

Although wave spray is the major cause of icing on the vessels, the physical behavior of wave impact is still poorly understood (Hendrickson *et al.*, 2003). Besides a few observational studies, which provide a rough understanding of spray cloud Liquid Water

Content (LWC) and spray heights, little research on this subject is available in the literature (Borisenkov and Pichelko 1975; Ryerson, 2013). In recent years, efforts to model marine icing phenomena using numerical methods have shown progress, but the multi-scale nature and complexity of the problem necessitate separation of the problem into smaller single-phenomenon steps. The generation of spray is divided into several stages, including free surface modeling, wave slamming on the bow, the air entrainment process during impact, water sheet and jet formation on a wall after wave slamming, water sheet and droplet breakup caused by wind, and droplet trajectories when they meet the surface of the ship's deck (Hendrickson *et al*., 2003; Dommermuth *et al*., 2007).

This chapter is focused on a review of the state of the art in direct and related work on spray cloud formation after the wave impact. Field observations that have considered the spray flux spray heights and other specific characteristics of spray clouds are covered in the first subsection. Experimental studies on wave-vessel interactions are addressed in the next subsection followed by the numerical background. The numerical part of this chapter covers numerical methods for modeling the free surface, wave slamming, air entrainment, and turbulence related to the proposed problem. Further, the literature review regarding the Maximum Entropy Principle (MEP) for predicting the droplet size and velocity after the wave impact is presented. Finally, a background review regarding the analytical approach that combine several mathematical models of physical behaviour procedure of wave spray formation is listed and reviewed.

Although this thesis focuses on several individual methods for different stages of the complete spray generation phenomena, it is the combination of the models for the various stages that provides a full model of the process leading to a broader contribution and fuller understanding of the marine wave spray problem. Linking these subjects and covering the gaps are crucial for progress in this field.

1.1 Field Observation

Water droplets are dispersed into the atmosphere and carried by the wind after waves hit a structure. Observations of the phenomena establish the importance of this aspect, but unfortunately, there is a relatively small body of literature that contributes to physical understanding or provides measurements of wave spray phenomena.

Field data available from vessels are limited, and thus analytical formulations are based on a few field observations (Borisenkov and Pichelko 1975, Ryerson 1990). These observations mostly report a vertical distribution of the Liquid Water Content (LWC) above the ship's bow. The LWC is defined as the volume of liquid water per unit volume of air. Generally, these observations do not include information about the velocity of the water droplets or the size distribution of droplets. Information about the position of the measurement instruments on the ship's deck and the geometry of ship's bow are also unknown in most of the cases. Effective measurements of a spray cloud from field observations should contain the following factors which are categorized into five groups and are shown in Table 1-1.

Table 1-1 Effective Parameters in the study of spray cloud formation for field observation

Effective Parameters	Parameter Name
Ship Parameters	Ship Speed Ship Bow Geometry Ship Movement (Acceleration, Pitch, and Heave)
Wind Parameters	Wind Speed Wind Direction
Wave Parameters	Wave Height Wave Length Frequency distribution (Wave Spectra) Wave Propagation Direction Wave Speed Wave profile relative to bow
Spray Cloud Information	Droplet Size Distribution Velocity Distribution of Droplet Distribution of Droplet Concentration
Time	Frequency of Spray Cloud Generation Duration of Spray Cloud
Meteorological Factors	Air and Ocean Surface Temperature Relative Humidity Barometric Pressure Water Salinity

Most of the parameters in Table 1-1 are well-recognized, except for droplet information, such as their size and velocity distribution in front of the vessels or offshore structures. These parameters are crucial for understanding the amount of spray flux and are addressed briefly in the paper by Lozowski and Zakrzewski (1990) as significant

parameters. Information about droplets such as size and velocity guide the estimation of the spray flux, vertical distribution and maximum height of the spray cloud.

A few previous studies focused on defining a relationship for measuring the vertical distribution of the LWC and the amount of water delivered to topside from the spray cloud. Zakrzewski (1985), who used the data from the Borisenkov and Pichelko (1975) observations, reports some of the parameters listed in Table 1-1, such as ship speed, ship heading angle, wind parameters, wave parameters and time. Information about droplet size and droplet velocity distribution which lead to the calculation of the LWC and a maximum height of the spray cloud are not reported. The LWC and a maximum height of the spray cloud are calculated based on the empirical formulation by Zakrzewski (1985). The following two sections review the previous research for understanding the LWC formulations for both vessels and offshore structures.

1.1.1 Spray Cloud Formulation for Vessels

The most significant parameters for modeling spray cloud formation are thought to be the LWC, maximum vertical height of spray cloud, and duration time. This section reviews studies that have proposed formulations for the LWC, the maximum vertical height of a spray cloud and the spray cloud duration.

1.1.1.1 Liquid Water Content (LWC) Formulations

The first and simplest LWC equation for the water cloud after wave impact on a ship is defined by the formula (Katchurin *et al.*, 1974):

$$w = \xi H \qquad \left(\frac{kg}{m^3}\right) \tag{1-1}$$

where w is LWC, H is the wave height, and ξ is a constant equal to $10^{-3}\ kgm^{-4}$. This formula was proposed based on measurements from a Medium-sized Fishing Vessel (MFV), where the ship moves relative to waves with the heading angle of $\alpha \geq 140^{\circ}$, at speeds of 6 – 8 knots. Unfortunately, information about the techniques and locations of the measuring facilities on the ship was not reported. Comparison of the data from Katchurin *et al.* (1974) with the listed factors and parameters in Table 1 shows that some of the essential parameters in the study of the LWC or spray cloud are not reported.

Another empirical formulation for the vertical distribution of the LWC based on field data for an MFV (*Narva*) in the Sea of Japan was introduced by Borisenkov and Pichelko (1975) and calculated by the formula:

$$w = 2.36 \times 10^{-5} \exp(-0.55h) \qquad \left(\frac{kg}{m^3}\right) \tag{1-2}$$

where h is the elevation of an object above the deck of the MFV, and the freeboard height of the MFV is 2.5 m. The LWC is based on the volume of water (w) in a unit volume of air

(a). The MFV moves into the waves with an angle of $\alpha = 90^{\circ} - 110^{\circ}$ with a speed of $5 - 6$ knots. The wind speed reported is $10 - 12\ ms^{-1}$. This formulation is limited to the specific type of ship under certain sea conditions, and cannot be used to calculate the vertical distribution of LWC for different type of ships and different sea conditions.

Zakrzewski (1986) extended this formulation to other types of ship's geometry and other sea conditions leading to the following formulation for the vertical distribution of the LWC:

$$w = 2.032 \times 10^{-2} \cdot \left(\frac{H}{H_0}\right) \cdot \left(\frac{V_r}{V_0}\right)^2 \cdot \exp(-0.55h) \qquad \left(\frac{kg}{m^3}\right) \tag{1-3}$$

where H and V_r are the wave height and the ship speed relative to a wave, respectively. H_0 and V_0 are the wave height, and ship speed relative to the wave from the Borisenkov and Pichelko (1975). Zakrzewski (1986) attempted to calculate the values of H_0 and V_0 based on approximations of the wind speed and fetch values in the Sea of Japan, which cannot be found in the Borisenkov and Pichelko (1975) paper. Based on these approximations, the values of the two parameters are calculated as $H_0 = 3.09\ m$ and $V_0 = 11.01\ ms^{-1}$. V_r in Eq. (1-3), which is the ship speed relative to the surface of the wave, suggested by Zakrzewski (1986) as:

$$V_r = 1.559\ T_w - 0.514\ V_s\ cos\alpha \qquad \left(\frac{m}{s}\right) \tag{1-4}$$

where V_s , T_w and α are ship speed, period of the wave, and heading angle, respectively.

The Horjen and Vefsnmo (1987) model, which is based on the spray measurement on a Japanese ship, is defined by the following formula:

$$w = 0.1\ H \exp(H - 2z) \qquad \left(\frac{kg}{m^3}\right) \tag{1-5}$$

where H is the wave height and z is the elevation above sea level.

Another model is proposed by Brown and Roebber (1985) based on the Borisenkov and Pichelko (1975) work. This model incorporates the statistical behavior of the wave height distribution, and defines the LWC using the following formula:

$$w = 4.6 \cdot \exp\left(\frac{2z}{\bar{H}}\right)^2 \qquad \left(\frac{kg}{m^3}\right) \tag{1-6}$$

where z is the elevation above mean sea level and $\bar{H}$ is the mean wave height.

Ryerson's (1995) observations of spray events on a U.S. Coast Guard cutter show new results, compared with previous observations, which were for small trawlers or Medium-sized Fishing Vessels (MFV). The spray flux was measured in six different parts of the ship, various distances behind the bow, such as the starboard, main port deck, first level bulkhead surfaces, second level bulkhead and flying bridge deck surfaces, but is reported for only one location in the paper. Frequency, location, height, duration, and size distribution of spray clouds were recorded by the camera. The weather conditions, ship position, speed, and heading angle were recorded every hour. Several events of spray on

the ship were observed, and the results of the LWC, spray duration, droplet size, and droplet number concentration were reported. Mean droplet concentration in all events is about 4×10^5 droplets per m^3 and average cloud droplet concentration is 1.05×10^7 droplets per m^3. These observation data show that the spray droplet size varies from 14 to 7700 μm. The average spray event duration was reported as 2.73 seconds which is longer than the results measured from the Soviet MFV, which was 2 s (Borisenkov and Panov 1972). Ryerson (1995) tried to formulate the LWC but his comparison between his reported measurements and previous LWC formulations was not satisfactory.

1.1.1.2 Maximum Height of Spray Cloud

The maximum height of the spray cloud is the highest elevation that spray droplets can reach above the ship deck. It was determined with a simple geometric model by Zakrzewski and Lozowski (1988). This calculation was based on field data from Kuzniecov *et al.* (1971) which was reported for an MFV. This model was tested for several moving ships and sea conditions. The formula for the calculation of the maximum height of spray above the ship's deck is:

$$Z_{max} = 0.65\, V_r + h' \tag{1-7}$$

where h' is the height of the bulwark (0.75 m), the unit of constant 0.65 is in time (s) and V_r is the ship speed relative to the wave speed V_w. This formulation is based on the data

observation from *Jan Turlejski*, which is an MFV, although the size of this vessel is larger than the typical Soviet MFV. The spray height is influenced by the ship size and bow geometry but because of the complexity of calculation, these factors were neglected in most of the studies. It was suggested by Zakrzewski (1987) that there is a need to have a relation between the air-sea and ship motion parameters and the maximum height of spray flight for calculating the vertical extent of the collision-generated spray (Zakrzewski and Lozowski 1988). The authors used the results from Kuzniecov *et al.* (1971), who published the relation between the maximum height of ice accretion on the MFV and the relative wind speed, for defining the relation between the maximum height of spray and the ship motion parameters. Subsequently, equations of droplet motion were used in their paper to calculate the trajectory of droplets which hit the vessel's foremast.

Zakrzewski (1987) reported a formula for the relationship between the maximum height of the spray jet and the air-sea and ship motion which is defined as:

$$Z_{max} = aV_r \tag{1-8}$$

where Z_0 is the maximum height of the spray with respect to the ship deck, and a is an empirical constant, which is calculated from the data in Kuzniecov *et al.* (1971) and is equal to 0.535 with time (s) unit. They calculated the heights of the upper limit of ice accretion on the foremast of a MFV and reported parameters such as the ship heading angle, ship speed and the velocity of wind for 13 different cases of icing.

Sharapov (1971) reported several observations for the maximum height of spray for different parts of the MFV, such as the foremast, rigging, front side of the superstructure, and roof of the superstructure. The results show a maximum height of spray for different wind speeds in 5 – 10 in Beaufort scale, which is equivalent to 8 – 32 ms^{-1}. The ship heading angle for most of the values is $\alpha = 180^{\circ}$ but for some of the values is $\alpha = 135^{\circ}$. The original data from the Sharapov (1971) observations are shown in Table 1-2.

Table 1-2 Observed Height of Spray over the ship moving through waves (Sharapov 1971).

Wind Force in Beaufort	**Wind Speed** $(\boldsymbol{m\ sec^{-1}})$	**Foremast Rigging**	**Front side of Super-structure**	**Roof of Super-structure**	**Boat Deck**
5 B	8-10	Up to 5.5 m above deck	No spray	No spray	No spray
6 B	11-13	Up to 7.9 m above deck	Spray hits object	No spray	No spray
7 B	14-17	Up to 10.5 m above deck	Spray hits object	Spray hits object	No spray
8 B	18-20	10.5 m above deck	Objects entirely sprayed	Objects entirely sprayed	No spray
$\geq$ 10 B	25-32	10.5 m above deck	Objects entirely sprayed	Objects entirely sprayed	Boat deck hit by spray

1.1.1.3 Spray Cloud Duration

Another significant parameter is the duration of the spray cloud formation from the wave-vessel impact through to the fully expanded spray above the ship's bow. Zakrzewski (1987) defines the total duration of the spray cloud as:

$$\Delta t = c\frac{HV_r}{U_{10}^2} \quad (1\text{-}9)$$

where c is an empirical constant based on the shape and size of the ship hull, H is the wave height, V_r is the ship velocity relative to wave speed, and U_{10} is the wind speed. The empirical constant c is equal to 20.62, under specific conditions of a wave length equal to 3.09 m, wind speed of 11 ms^{-1} and ship velocity of 2.83 ms^{-1}.

The duration of the spray event from the Lozowski *et al.* (2000) model was computed with the empirical constant c equal to 10. This empirical constant value was changed for the United States Coast Guard Cutter (USCGC) based on the Ryerson (1995) observations, which indicated that the spray duration is about 3 to 5 s. Ryerson (1995) computed the spray event duration by subtracting the time frame of the first event from the time frame of the last event. It was shown that the minimum spray duration was 0.47 s and the maximum was 5.57 s with the mean cloud duration of 2.73 s over a total of 39 events. Horjen (2013) used the same formulation and suggested that the mean duration of each spray cloud is 2.9 s based on his personal communication with Zakrzewski and his measurements from the MFV *Zandberg*.

1.1.2 LWC formula for offshore structures

Different field observations and empirical formulations have been reported for calculation of the spray mass flux and icing on offshore rigs and structures. Several computer models have been produced to model icing on these structures. The major

differences between vessels and offshore structures are their geometries (impact and droplet impingement areas), heights, and their relative velocities. Offshore structures are generally higher in height compared with vessels. The shape, impact areas, and droplet impingement areas vary widely between structures and vessels and shape factor should be taken into account. Because the geometry and height differences the duration and amount of spray are also different. Forest *et al.* (2005) worked on the RIGICE code and upgraded a previous version of this code to RIGICE04, which is a program for simulating ice accretion on offshore structures due to spray generation from wave impact. A new Liquid Water Content formula is derived for a height of 10 meters, which is in agreement with the data from the *Tarsiut Island* field data. The LWC is based on the work of Borisenkov and Pichelko (1975) and Zakrzewski (1987). The data from the *Tarsiut Island* (Muzik and Kirby, 1992) field observations were used and the original formula changed to a new model for offshore structures as:

$$w = K_1 \cdot H_{1/3}^2 \cdot \exp(-K_2 h) \qquad kgm^{-3} \tag{1-10}$$

where K_1 and K_2 are the empirical constants based on the field data. $H_{1/3}$ is the significant wave height. This formula represent the LWC above the top of the wave-wash zone. Both the vertical and horizontal spray distribution was reported and derived analytically by Forest *et al.* (2005). They reported the LWC for one field observation on *Tarsiut Island* and for one single spray event which can be calculated as:

$$w = 1.35 \cdot H_{1/3}^2 \exp(-0.53h) \qquad kgm^{-3} \tag{1-11}$$

These LWC formulas are based on one specific field observation, and the results and formulations of these observations only match their own data, and cannot be used for other conditions (Roebber and Mitten, 1987; Forest *et al.,* 2005). Forest *et al.* (2005) compared different LWC formulas from different authors, such as Horjen and Vefsnmo (1984), Brown and Roebber (1985), and Zakrzewski (1986) with the data from the semi-submersible drilling platform, *Ocean Bounty*, which experienced several icing events. Spray flux calculated for the amount of icing on this structure was reported as 5 to 10 $kg\ m^{-2}\ hr^{-1}$ (Roebber and Mitten 1987). This calculation was based on the average wind speed of 45 ms^{-1}, the mean significant wave height of 3.8 m, and the deck level of 10 - 15 m. The results conclude that the LWC calculation from the Zakrzewski (1986) and Forest *et al.* (2005) models are in agreement with the field observations from the *Ocean Bounty*, but the other models do not show comparably accurate results.

Roebber and Mitten (1987) reported the number of significant waves which produced significant spray clouds as 24 waves per hour for the *Tarsiut Island*, and the vertical height of these spray clouds was estimated as 10 m. As noted, these data were calculated for an artificial island and assumed the same as for offshore rigs. However, other researchers expressed uncertainty about this correlation.

Horjen and Vefsnmo (1987) introduced an empirical formula, which was used by Kulyakhtin and Tsarau (2014). This formula modeled the spray on a semi-submersible oil rig, to model the spray flux for further calculation of icing. This formula for spray flux is:

$$F_{HV}(z) = \frac{M_{HV} U_{10} T_w}{\tau_{dur}} \frac{1-\left(1-10^{-2}U_{10}\right)\exp\left(-\left(\frac{4z_{HV}+2}{9}\right)^2\right)}{\exp\left(k_{HV} U_{10}^{0.667} z_{HV}^2\right)} \cos\alpha \quad (1\text{-}12)$$

where $M_{HV} = 6.28 \times 10^{-4}\ kgm^{-3}$, $k_{HV} = 0.0588\ s^{0.667}m^{-0.667}$, $z_{HV} = (2z/H_s) - 1$, H_s is the significant wave height, z is the height above mean sea level, α is the angle between the normal vector to a surface and the wind direction, U_{10} is the wind speed at $z = 10\ m$, T_w is the wave period, and τ_{dur} is the duration of spray events.

1.1.3 Usage of LWC Equations

Several models were made to calculate the icing rate on different kinds of ships and most of them use the Zakrzewski (1987) LWC model to calculate the spray rate after wave-ship impact. Lozowski and Zakrzewski (1993) developed the icing model for ships. A larger sized ship, the United States Coast Guard Cutter (USCGC) *Midgett* model, rather than an MFV, was considered in their simulation, and the spray model of Zakrzewski (1987) was modified. Chung and Lozowski (1999) improved this methodology and developed the new model based on data from the Canadian fishing trawler, *MV Zandberg*.

Lozowski *et al.* (2000) reviewed the computer models for the icing on vessels and offshore rigs. The four computer models simulating topside icing included RIGICE,

ICEMOD, Ashcroft (1985), and Romagnoli (1988). These models compute ice accretion for each forecasting time-step caused by a single spraying event. Lozowski *et al.* (2000) reported the formulation of the wave-ship spray model based on the Zakrzewski (1987) model. It was reported that an increase in fetch causes increasing wave heights, which increases spray flux on the ship. An increase in ship speed into the waves causes more spray flux on ships. The consequent influence of fetch and ship speed on the ice load was reported as well.

The ICEMOD model was produced at the Norwegian Hydrodynamic Laboratories (NHL) and calculated icing on structural segmentations of offshore rigs. This model was introduced by Horjen and Vefsnmo (1986a; 1986b; 1987). ICEMOD can compute ice weight and thickness along horizontal and vertical planes and cylinders in one dimension for two modes, categorized as ship mode and rig mode. The recently published paper by Horjen (2013) described the improved model of ICEMOD2, which is a two-dimensional code. The mass flux of sea spray is calculated based on the following formula:

$$\dot{M}_c = f(U_{10}, H_s, T_s, W, \alpha) \cdot (AZ + B) \qquad (kgm^{-2}s^{-1}) \tag{1-13}$$

where Z is the height above the mean sea level and H_s and T_s are the significant wave height and period, respectively. H_s and T_s are introduced as empirical relations for Norwegian waters and calculated based on Eqs. (1-14) and (1-15) respectively:

$$H_s = 0.752 \cdot U_{10}^{0.723} \qquad (m) \tag{1-14}$$

$$T_s = 6.16 \cdot H_s^{0.252} \qquad (s) \tag{1-15}$$

A and B are non-dimensional constants, dependent on the relative wind and spray heading angle α, and W is the vessel speed.

These constants were reported for different heading angles based on the field data from the vessel *Endre-Dyroy* for the specific wave height and period of a specific wave spectrum. f in Eq. (1-13), is defined by the formula:

$$f(U_{10}, H_s, T_s, W, \alpha) = \left(\frac{\rho_w H_s^2}{T_s^2 U_{10}^2}\right)\left(\frac{gT_s}{4\pi} + W cos\alpha\right) \qquad (kgm^{-2}s^{-1}) \tag{1-16}$$

where U_{10} is the wind speed at $Z = 10\ m$, which is the height above the mean sea level, ρ_w is the water density, and α is the heading angle.

A similar formula was introduced by Horjen and Carstens (1989), which was presented based on field observation from various test objects that were attached to the front mast of the *Endre Dyroy* vessel, operating in the Barents Sea. The formula is presented as:

$$\dot{M}_c = A \cdot f(U_{10}, H_s, T_s, W, \alpha) \cdot (Z^*)^B \qquad (kgm^{-2}s^{-1}) \tag{1-17}$$

$$Z^* = \frac{2Z}{H_s} - 1 \tag{1-18}$$

where $\dot{M}_c$ is the mass flux of sea spray.

Comparing the parameters' reported in the field observations of Horjen and Carstens (1989), with the parameters listed in Table 1-1, shows that the only oceanographic parameter was the significant wave height. The spray flux was measured by spray collectors at the front mast, which was located 14 m from the front of the bow and placed at elevations of 1.10, 2, 3.60 and 5.35 m above the base of the mast. The height of the bow from the waterline was reported as 5.5 m. The spray frequency and the duration of spray were not evaluated but, it was stated that duration of spray and median droplet diameter can be calculated based on the data from the *Zandberg*, which were equal to 2.9 s and 1.8 mm, respectively.

RIGICE is another computer model for the calculation of icing, produced by Roebber and Mitten (1987). They reported that spray flux varies strongly as a function of wave steepness, wave energy flux, and structural shape of impact surface. Wave-generated LWC was calculated as:

$$w = 1.31715 \times 10^{-3} \cdot H^{2.5} \cdot \exp(-0.55h) \qquad (kgm^{-3}) \qquad (1\text{-}19)$$

where H is wave height, and h is elevation above the deck. The constant has the unit of $kgm^{-6.5}$. The LWC vertical distribution is assumed to be equal to the Borisenkov and Pichelko (1975) model. The model was compared with the Zakrzewski (1987) model with

several wind and wave conditions and shows an agreement with that model. However, models were compared with results from the *Treasure Scout* field program, but an adequate agreement was not reached, most likely due to scaling issues.

Lozowski *et al.* (2000) described the spray formulation improvement of the RIGICE code and discussed the simulation of spray generation as a result of wave impact for both vessels and offshore structures. Lozowski *et al.* (2000) worked on improving the spray model and the LWC formulation. In the RIGICE code, it was assumed that the vertical distribution of the LWC does not vary exponentially when a point of interest, close to the ejection point of droplets, is considered. The vertical distribution of the LWC is assumed to be a thin liquid sheet (spray jet) that is already broken up due to wave-vessel impact. Droplet impingement strongly depends on the distance between the ejection point and the point of interest on the structure.

The new spray algorithm, which was used in RIGICE, calculates the flux distribution based on droplet trajectories. It depends on wave period, wave height, wave spectrum, wave run-up on the structure, and consideration of wave force for analysis of the droplet trajectory. The new spray algorithm defines horizontal and vertical velocity components of the droplet for the calculation of droplet trajectory as the following formulas, respectively:

$$u = \frac{\pi H}{T_w} e^{kz} \sin\theta + C \tag{1-20}$$

$$w = \frac{\pi H}{T_w} e^{kz} \cos\theta + \frac{z_r - z}{t_r} \quad (1\text{-}21)$$

where u and w are the horizontal (x) and vertical (z) components, respectively. H is the height of the wave at zero force, T_w is the wave period, k is the wave number, z is the amplitude of the wave at zero force, θ is the phase angle of the wave at zero force, C is the wave celerity, z_r is the wave run-up height at maximum force, and t_r is the rise-time of the force. In this model wave diffraction theory is used to calculate wave run-up on the structure and the deep water linear wave theory is used to find the component of droplet velocity with the wave at the zero-force point. This situation happens at $\pi/2$ radians before the maximum force point. The vertical and horizontal velocity components are calculated based on the wave run-up on the structure and the wave celerity, respectively. The spray jet is assumed to start at the tip of the bow and extend symmetrically along both sides of the ship to a distance x, which is given by:

$$x = 2\,H + 0.04\,v_r^2 - 10 \quad (1\text{-}22)$$

where H is the significant wave height, the constant 0.04 has the unit of time (s) and v_r is the ship velocity relative to wind velocity and is calculated as:

$$v_r = 1.56\,\tau_w + v_s \cos(\pi - \alpha) \quad (1\text{-}23)$$

where τ_w is the significant wave period, v_s is the ship speed and α is the ship heading angle, which is equal to zero when the vessel is heading directly into the waves or wind. Lozowski *et al.* (2000) used the LWC formulation that is reported in Lozowski and Zakrzewski (1993).

Another computer simulation code for ice accumulation on offshore structures, called MARICE, was described by Kulyakhtin and Tsarau (2014). The code is a 3-dimensional, time-dependent model and uses Computational Fluid Dynamic (CFD) techniques to estimate icing formation on an offshore structure caused by sea spray. The spray part of this code can solve the spray flux on the surface in two ways: first, introduce spray flux formulation on the structure, and second, calculate spray flux based on the droplet trajectories using the Discrete Phase Model (DPM). DPM is a Lagrangian method that allows the simulation of a discrete second phase consisting of spherical particles dispersed in the continuous phase. The spray model in this simulation was introduced by Horjen and Vefsnmo (1985). The spray flux duration and wave period in this study were assumed as $2\ s$ and $3\ s$ for two wave periods, respectively. However, they reported limitations due to uncertainty in the spray generation because of the unknown droplet-size distribution and droplet trajectories.

Shipilova *et al.* (2012) used the LWC model of Zakrzewski (1987) to generate droplet clouds in front of two types of ships in order to calculate the icing rate. Mean Volume Diameter (MVD) is used to characterize the spray cloud in front of the ships and was set to 250 and 2000 μm. It was assumed in this computational model that the droplet cloud

was generated in the form of a square, and the spray cloud widths in front of the two types of ships, the *Skandi Mongstad* and *Geosund*, were assumed to be equal to 21 and 19 m, respectively. Kulyakhtin *et al.* (2012) used a mixed Eulerian-Lagrangian approach with the commercial software, FLUENT, to model the distribution of spray flow rate per unit area on the vessel surface. Similarly to Shipilova *et al.* (2012), they used the Zakrzewski (1987) LWC formulation for defining a spray distribution in front of the vessel.

Shipilova *et al.* (2012) validated their results, by conducting a series of simple on ground spray measurements. They modeled the simple experiment with CFD and compared the results of the computational and experimental models of ice accretion. The spray period and duration of spray were set according to the values from the Lozowski *et al*. (2000) model with the assumption of ship speed was 5 ms^{-1} and wind speeds were 10 and 20 ms^{-1}. The spray period values for two different wind speeds are assumed to be 17.7 and 25.4 s, respectively, and spray durations are chosen as 4.06 and 3.73 s, respectively. The authors considered two different vessels, the *Geosund* and *Skandi Mongstad*. The amounts of ice accretion for different wind velocities, droplet sizes, and temperatures was predicted for these vessels, which showed higher ice accretion with conditions of higher wind velocities and smaller droplet sizes. The authors indicated that the results show that the total amount of icing from smaller droplets is higher than that from larger droplets.

All of the main field observation studies are compared with the ideal requirements outlined in Table 1-1, and the differences are depicted in Table 1-3. This indicates the need for more detailed observation for better comprehension of this phenomenon.

Table 1-3 Available field observation compared with the categorized factors for effective field observation.

Field observation	Ship Parameters	Wind	Wave	Droplet Information	Time
Borisenkov and Pichelko (1975) (Russian MFV)	Ship speed and ship heading angle	Wind velocity	Only wave velocity	No information related to droplets (Empirical Formula for LWC)	Spray duration for only one event. (No Frequency)
Horjen and Vefsnmo (1986) (*Endre Dyroy* trawler)	Ship speed and ship heading angle	Wind velocity	Only wave velocity	No information related to droplets (Empirical Formula for LWC)	-
Ryerson (1995) (U.S. Coast Guard Cutter)	Ship speed and ship heading angle – Bow geometry is available	Wind velocity	Only wave velocity	Droplet Size, No information related to droplet velocity, calculation of LWC for each event	Spray duration, No frequency

1.2 Experimental Simulation

Seawater has been determined to be the primary source of icing in cold and harsh conditions. Therefore, the behavior of wave-ship and wave-structure interactions need to be considered as part of the icing process. The rate of spray freezing and ice growth on vessels or offshore structures correlates with water delivery rates due to spray arising from wave impact.

Previous studies correlated the amount of spray cloud and water delivery to several parameters, such as marine object geometries, wave characteristic, ship velocity, etc. (Horjen and Vefsnmo 1984; Zakrzewski 1987; Ryerson 1995). Aside from the field observation approach, several researchers have explored different techniques, such as analytical, numerical, and experimental methods, for a better understanding of the marine icing. There is limited information in the literature related particularly to wave spray formation. Further, new studies in this field indicate that droplet size and velocity distribution in a spray cloud are significant factors that result in the shape and extent of the spray cloud over vessels or an object (Dehghani *et al*., 2016a; 2016b). Past studies mostly focused on mono-size models that do not consider the spatial distribution of droplets and the lack of spatial distribution models forced researchers to use mono-size and mono-velocity models (Shipilova *et al.,* 2012; Horjen, 2013; Dehghani-sanij *et al*., 2017a; 2017b).

Aside from the parameters above, more recent studies indicate that the process of spray-cloud formation happens in stages—wave slamming, water sheet formation, air entrainment, primary droplet breakup, and secondary droplet breakup—which were not thoroughly examined before (Hendrickson *et al*., 2003; Bodaghkhani *et al*., 2016; 2017). Better field observation data, combined with the experimental and numerical modeling of wave spray, are all necessary to better understand these complicated phenomena. Knowledge of some stages of spray-cloud formation, such as wave slamming, is well developed (Peregrine 2003), but flow kinematics and fluid behavior during most of the

other stages are unknown, and experimental measurements in this field are limited. The geometry and height of the impact zone (vessels or structures) in full scale are large enough that water goes through all the aforementioned spray-cloud-formation stages. One important factor is that the wind quickly and randomly accelerates the rising water sheet through this process, which makes study in this field challenging.

Laboratory-scale experiments directly related to wave-spray behavior and spray characteristics due to wave impact are very limited in the literature. Chung and Lozowski (1998) derived a full-scale spray flux equation for a ship-generated spray for the stern trawler *Zendberg*. This model related the spray flux to ship speed and wave heights. Past studies by Watanabe and Ingram (2015, 2016) analyzed the effects of jet and spray formation due to wave impact with a wall in shallow water. A linear stability analysis was used to analyze the behavior of a sheet arising from the wave impact. Several statistical models of polydisperse spray were used to investigate the behavior of droplet size distributions.

Since there are not enough quantitative velocity measurements of jet and spray after the wave impact with the structure, we thus review the measurement of wave impingement on the surface and wave impact pressure with an object. A principal step for analyzing the wave-body interaction is to understand the physical behavior of a wave slamming on a wall or body in deep water. The wave-body impact process produces high impulsive pressure on the wall, and some air that is trapped in this process creates higher pressure, which is called an air-pocket or air-entrainment.

Chan and Melville (1987) reported that breaking-wave impacts created higher pressure on the object. Chan and Melville (1987) experimentally investigated the dynamics of trapped air at the moment of impact on a surface-piercing plane wall by making an accurate simulation of the plunging wave. The deep-water wave plunging in this experiment was similar to the work of Longuet-Higgins (1974) and Greenhow *et al.* (1982). In this experiment, impact pressure, fluid velocity, and surface elevation were monitored simultaneously with a pressure gauge, a laser anemometer, and a laser wave gauge. A high-speed camera was used to provide a qualitative description of the impact process. Chan and Melville (1987) reported that spray occurred immediately after the impact in all the cases of the experiment. This research also showed that trapped air and the shape of the breaking crest at the moment of impact with the wall is a significant factor in changing the pressure and velocity of the wave impact. A comprehensive review of wave slamming on walls can be found in Peregrine (2003).

An important factor in the study of wave-body interaction is the shape of the wave crest as it meets the wall, which has a significant influence on the quality of impacts (Bogaert *et al.,* 2010). The relative angle between the body and the fluid surface was reported as a factor in analyzing impact pressure and velocity by Kapsenberg (2011). Different wave-body interaction angles led to dissimilar and complex impact phenomena with different air entrainment mechanisms. Three different types of wave-wall impacts with different air entrainment mechanisms are shown in Fig. (1-1) from Bogaert *et al.* (2010).

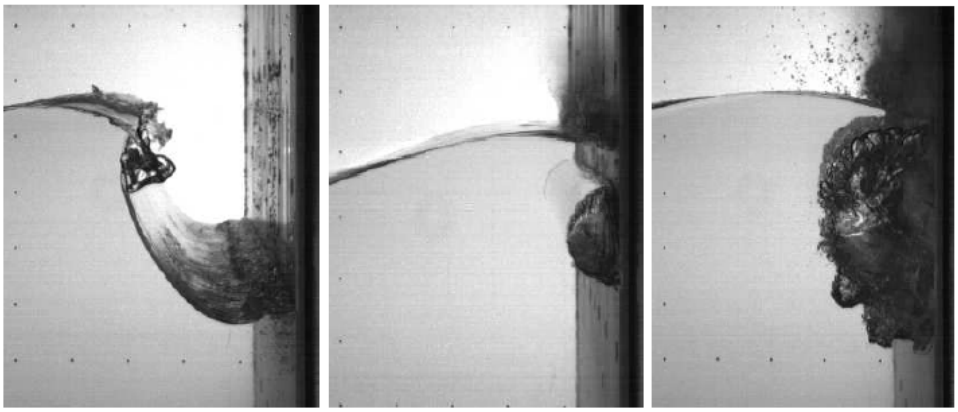

Fig. 1-1 Water Slamming on a wall. Left: broken wave impacting on the wall. Centre: wave impact with air entrainment at large scale. Right: Wave impact at full scale with air entrainment. The moment that a wave crest impacts the wall, the spray is produced (Bogaert *et al.,* 2010).

The difference between a plunging wave and a deep water wave in wave-body impact is another area of study, which has not received as much attention. The majority of researchers have focused on analyzing and calculating the pressure, whereas the wave impact on a ship, the spray formation, and the fluid flow behavior after the impact have not been a concern (Fig. 1-2).

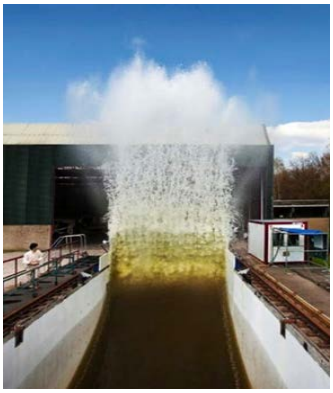

Fig. 1-2 The behavior of spray formation and spray cloud at different heights was not a concern. The impact pressure was studied. (Sloshel Project, Brosset *et al.,* 2009).

The water impact problem has received considerable attention. Wagner's theory (Wagner 1932) was introduced as the basic, applied theory for the water impact problem. The Wagner theory is based on a flat-disc approximation and assumes potential flow theory for an incompressible liquid. The boundary conditions and Bernoulli equations are linearized to develop a solution for a wedge impacting on a flat water surface. However, this model assumes a local small dead-rise angle, and that no air pocket is entrapped, which is not applicable for large-scale water-vessel impact. However, it is practical for small-scale and laboratory-scale water impacts because it provides simple analytical solutions. A schematic view of the Wagner theory, which shows the interaction of the flow between the free surface and body surface is shown in Fig. (1-3). In this figure, the interaction between fluid and body produces a jet flow, which in practice, ends up as a spray. No details or research directly related to the inner domains, which are the jet formation and spray cloud formation, have been found.

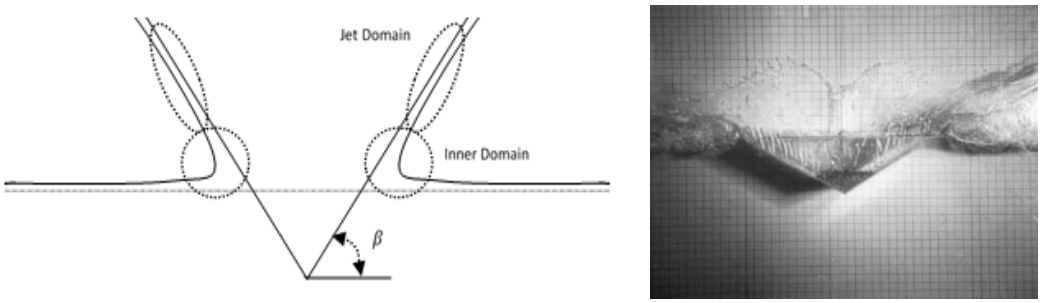

Fig. 1-3 Wagner Problem, no details, and research directly relative to the inner and jet domain can be found in the literature (left). Experimental view of wedge impact with the free surface by Qian *et al.* (2006) (Right).

Later studies worked on improving the Wagner theory by reducing the complexity of the model. These led to solving the analytical solution as an axisymmetric, two-dimensional model (Korobkin and Scolan, 2003), as well as the solution for the three-dimensional problem (Scolan and Korobkin, 2001). However, the point of interest for this theory and other studies related to slamming was to analyze the impact pressure on an object, and not to track fluid flow and capture spray formation. A detailed review of Wagner's theory can be found in Korobkin (2004) and Howison *et al.* (1991).

Another method associated with the Wagner theory is the Boundary-Element Method (BEM). This method was used by Greenhow and Lin (1985), Zhao and Faltinsen (1993) and Zhao *et al.* (1996) to solve the boundary-value problem. The distribution of velocity on the free surface, the shape of the free surface and the splash-up height of the domain are known at any time step. The pressure distribution and slamming force results from this method are in agreement with the experimental data and other numerical methods (Mei *et al.,* 1999; Zhao *et al.,* 1996). However, the effect of compressibility and other specific effects must be considered to understand the slamming phenomenon (Ogilvie, 1963).

Because of the complexity of the slamming problem, researchers tend to examine this problem from an experimental point of view. Bogaert *et al.* (2010) and Brosset *et al.* (2009) experimentally investigated the slamming problem in full scale and large scale by using two types of waves with different parameters. The reported reason that two types of waves were chosen was the difficulty of producing repetitive waves at full scale. Different types of wave impact occurred in the full-scale experiment, such as a flip-

through and wave pocket impact. The cause of these differences was reported to be the effect of wind. Wind clearly has an influence on the shape of the wave crest before and at the moment of impact, which changes the shape of the wave crest and makes repeatability uncertain. The effect of wind was not a concern for the large scale (1:6) experiment. The aims of the described experiment were to find a deterministic comparison between the full scale and large scale for defining the wave crest shape at impact, the air pocket behavior, and the pressure associated with the wave crest impact and air pocket. Other similar experimental attempts for modeling the wave pressure on the wall were reported by Chan (1994), Ding *et al.* (2008), and Colagrossi *et al.* (2010).

Greco (2001) investigated the behavior of a dam breaking, which was considered in the relevant literature as the same as the behavior of a vertical wall of water around the bow generated from wave-ship impact (Faltinsen, 2005). A 2-D case of a dam breaking, which was defined as the water impact with the wall, was extensively studied numerically and experimentally by many researchers (Greco, 2001; Marsooli and Wu, 2014; Ran *et al.,* 2015). In most of these studies, the pressure of impact on a wall, water overturning, free surface level, and velocity distribution along the free surface were analyzed and discussed.

Fullerton *et al.* (2010) numerically and experimentally investigated the wave impact pressure on a cube. The cube was located in three positions, completely under the free surface, at half-height above the free surface, and completely above the free surface. The angles of the cube relative to the incoming wave are $0^{\circ}, +45^{\circ}, and -45^{\circ}$. Two types of waves, breaking and non-breaking, with different wave heights and wave lengths were

used to study the physics of wave impact, and the trends of wave slap loads. The experiment was performed in a high speed tow basin. Pressure gauges were used on the side and top of the cube to measure the impact pressure of the wave.

The effect of wave bottom-slamming on ships and structures is an element of spray formation from the wave-vessel interaction. The bottom-slamming phenomenon is dependent on different variables and physical features and understanding these features are essential for studying the resultant spray formation. Greco *et al.* (2004; 2012) experimentally modeled water moving to the ship's deck (green water) and the wave bottom-slamming of a ship. Further, the model was investigated numerically in Greco and Lugni (2013). The experiment was performed in a towing tank equipped with a flap wave maker. A 1:20 scaled self-propelled patrol ship was used to separately investigate the effects of the ship motion on the water on deck using quantity measurement and optimal visualization.

The bottom pressure, local forces, wave elevation, rigid ship motion, and water on deck were recorded by different instruments. These and the flare pressure were discussed extensively for both types of modeling. The bottom slamming problem was modeled numerically using the Wagner theory to predict the maximum impact pressure at the time of impact. Overall, the experimental measurements and numerical solutions are in agreement with each other. However, the aim of this study was not directly related to spray formation.

Greco *et al.* (2004; 2012) reported that wave-body interactions producing water jets along the hull and the spray cloud led to the higher vertical motion. These two non-linear features of wave-ship interaction are not taken into account in their formulation. Underestimation of the experimental measurements was probably due to this neglect. The amount of water that exceeds the freeboard and turns into spray does not totally return to the deck, and overtopping events depends on the movement of incoming waves and the ship, which can be substantially different in a model compared with a full-scale ship.

Greco and Lugni (2012) investigated the water on deck problem using a 3-D weakly non-linear seakeeping method coupled with the water-on-deck method based on shallow-water theory. Different parts of the problem were divided into simplified models. A 2-D in-deck problem was split into a series of 1-D problems, which can be solved by the Godunov method for the main flux variables. The bottom-slamming problem was modeled with the Wagner theory, and the free surface was captured by the Level Set (LS) technique, which will be discussed in the next section. The transient Green function was used to linearize the radiation and scattering waves around the incident waves and solve the problem in the time domain.

Voogt and Buchner (2004) experimentally investigated wave impact pressure and the probability of wave impact on a FPSO. In this test, the simplified bow wave at the test scale of 1:60 in deep water was considered. The incident wave data, vessel motions, and bow pressure were calculated using data from a large array of pressure transducers and

force panels. A video recording system which was capable of determining the correlation between the wave shapes and the impact pressure-time traces was also used. The experiment shows that the linear theory for waves under-predicts wave steepness, but the second order wave theory provides a reasonable water surface model. It was observed in this experiment that up to a certain vertical free surface velocity no impact occurred between the wave and bow, but after this level, the probability of impact increases linearly up to a probability of 100% (Guedes Soares *et al.,* 2004).

Hu *et al.* (2006) and Hu and Kashiwagi (2009) numerically simulated the strongly non-linear behavior of a ship-wave interaction with the Constrained Interpolation Profile (CIP) method, which is based on a Cartesian grid method, to capture the interface of a two-dimensional wave impact with a floating body. An experiment was performed in a two-dimensional wave channel. A box type floating body was used instead of a ship scale model. A wave maker and a wave absorbing device were used at the two ends of the tank. Heave, roll, and sway of the floating body, wave elevation and a forced oscillation test in heave were performed. The results from the numerical method were compared to the experimental results for the case of fixed sway. The results show adequate agreement for different case studies, both for green water events and after its occurrence.

Hu and Sueyoshi (2010) used the same method and numerically investigated the behavior of extreme wave-body interaction to measure both ship motions and wave impact loads. This research modeled the wave impact problem in three dimensions and virtual particles were used to define the body. An experiment was performed in a towing

tank with the Wigley, ship model. The pressure of green water on the deck, as well as the heave motion of the ship, were calculated. For the numerical part of the solution, three grid sizes were used to predict the pressure and height of the free surface. All the models under-predicted the peak values of pressure, especially the low-resolution grid model. The free surface for the low grid resolution was not clearly modeled, but for two other high-resolution models, the results of the free surface level are in agreement with the experimental data. A container ship (S175) was modeled, and the snapshots that were presented in this research paper clearly showed water-on-deck and wave slamming features. Study of the spray cloud and jet formation after impact were not an objective of the mentioned study.

Asides from the simulation related to the wave impact pressure measurements, very limited researchers worked on the kinematics behavior of wave impact. Ryu *et al*. (2005) experimentally analyzed the kinematics of plunging breaking waves impinging and overtopping a structure and introduced a new method based on the principles of Particle Image Velocimetry (PIV) techniques. The BIV technique was used to measure the velocity fields in the aerated region around the structure. A study measuring the flow kinematics inside an aerated area with PIV techniques can be found in Govender *et al*. (2002). Other attempts to measure flow kinematics outside of aerated areas with the PIV method are reported by Chang and Liu (1999; 2000) and Melville *et al*. (2002). Chang and Liu (1998) measured the velocity of the overturning jet of breaking waves using PIV. The flow characteristics of aerated regions are rarely reported by researchers. Govender *et al*.

(2002) used a technique similar to PIV based on cross-correlating algorithms and image processing techniques. The BIV uses diffused backlighting for illumination, such as a Light-Emitting Diode (LED), instead of a laser. This new method generates shadow images from bubbly flow and droplets and uses these as tracers. Flow or bubble velocity was determined by correlating the texture of the images. Some applications of the BIV method for green water and sloshing can be found in Ryu *et al*. (2007a; 2017b), Chang *et al*. (2011), and Song *et al*. (2013).

Referring to the current experimental study presented in chapter 2, the primary focus of this study is to report the measurements of the droplet size and velocity for the process of spray cloud formation. This study can benefit other researchers for presenting analytical models for the size and velocity distribution of spray cloud during the wave impact with a lab-scale object. The current study applies the BIV technique to measure spray characteristics and flow kinematics due to wave impact using two models: a flat-shaped plate and a bow-shaped plate model. The process of wave impact to spray production was examined qualitatively. Flow velocity near the impact domain is obtained with the BIV technique. For validation, the results of the BIV method from the side view are compared with the results of DPIV method from the front view as well as results of the BIV and PIV measurements reported by Ryu *et al*. (2005) and velocity measurements of Chang *et al*. (2003), which used Fibre Optic Reflectometry (FOR) for measuring the velocity field. Wave characteristics and impact pressure are measured with several

pressure sensors and wave probes and compared with experimental results by Fullerton *et al*. (2010).

1.3 Numerical Simulation

In recent years, efforts to understand the marine icing phenomena using numerical methods have shown progress (Dommermuth *et al.*, 2006). While the CFD methods become mature enough to be considered practical tools for these multi-scale applications, less precise, but more practical, approaches have been applied in the meantime.

In recent years, considerable effort has been applied to the numerical modeling of water slamming in predicting the local damage from wave impact on structures and the prediction of water-on-deck phenomena (Chan and Melville, 1988; Kleefsman *et al.,* 2005). There has been less focus on the numerical simulation of spray formation arising from wave impact. The Numerical Flow Analysis (NFA) code by Dommermuth *et al.* (2006) used Cartesian-grid formulation with the VOF method to model breaking waves around the ship. Fullerton *et al.* (2009) used the NFA code to measure the wave-impact force when it impacts with a cube, which is located slightly above the free-surface level. The data on the Fullerton article showed the spray formation above the cube. Furthermore, some researchers focused on the study of bubble entrainment for the case of deep water wave breaking and during the jet/splash impacts (Derakhti and Kirby, 2014). However, in this study effect of bubble entrainment and aerated wave impact were not considered.

The multi-scale nature of this problem, which ranges from the macro-scale in meters for the wave and vessels, to the micro-scale, in millimeters and micrometers, for the spray droplets, makes numerical simulation extremely complicated (Bodaghkhani *et al.,* 2016). Numerical studies of wave-vessel interaction and spray production are complex problems in CFD (Brucker *et al*., 2010; Dommermuth *et al.,* 2006). The non-linear interaction between an extreme wave and a floating body needs to include the behavior of free surface turbulence, wave impact, wave breakup, air entrainment and bubble generation, spray sheet formation, and droplet trajectory (Hendrickson *et al.,* 2003). The stages of this complicated phenomena are shown schematically in Fig. (1-4).

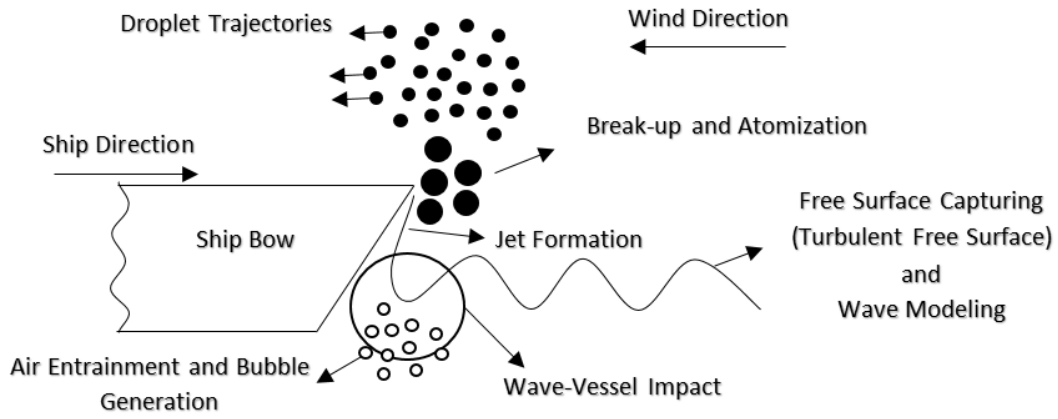

Fig. 1-4 Modeling procedure for solving the wave-vessel impact problem.

Different numerical methods have been developed to address discontinuities. Lagrangian and Eulerian approaches have been used in successful numerical approaches to approximate free boundaries in fluid flow. Both methods have advantages and disadvantages and selection of technique is based on the nature of the problem. Several

reviews of free surface flow are available by Mei (1978), for linear free surface flow using integral methods; Floryan and Rasmussen (1989), for numerical methods for viscous flows with moving interfaces; and Tsai and Yue (1996) for computational methods of non-linear free surface flows. A comprehensive literature review for two Eulerian methods, Volume of Fluid (VOF) and Level Set Method (LSM) that are used in the numerical simulation are reviewed.

1.3.1 Volume of Fluid (VOF)

Hirt and Nicholas (1981) first introduced the VOF method which was simple and efficient compared to other models for the calculation of free boundaries. This Eulerian technique was used to simulate the deformation of a free surface numerically. VOF defines a fluid fraction function $F(x, y, t)$, which has a value between unity and zero which represents the volume fraction of the cell occupied by fluid. Cells with F value between zero and one represent a free surface and they must have at least one neighbouring cell for which the F value equals zero. The VOF method requires less storage capacity for each cell. The derivative of F can be used to calculate the boundary normal. By knowing the normal direction and value of F, a line representing the free surface can be shown. The VOF technique is a simple and economical way to track the interface and free boundaries.

The first VOF code for calculating the free surface was introduced by Nicholas and Hirt (1975) which they titled SOLA-VOF. Chorin (1980) and Lafaurie et al. (1994) made

subsequent improvements. More accurate and advanced techniques were introduced and used, such as the Piecewise Linear Interface Construction (PLIC) method (Ashgriz and Poo, 1991; Rider and Kothe, 1998). In this method, the free surface is approximated by segments fitted to the boundary of every two neighboring cells. The velocity field fluxes are computed at cell faces, and the fluid is moved from a donor cell to an acceptor cell (Young, 1987).

One of the advantages of the PLIC method is that it does not attempt to reconstruct the interface as a continuous chain of joined segments. Rather, it reconstructs the interface as a discontinuous chain with asymptotically small discontinuities. Whenever the curvature is small (i.e., the radius of curvature is large with respect to the grid size) this method will be accurate (Scardovelli and Zaleski, 1999). Use of the original VOF method leads to the appearance of small air-pockets called 'flotsam' which is due to the piecewise constraint (Rider and Kothe, 1998). Refer to the original VOF method; fluid can be lost or gained due to rounding in the F function (Harvie and Fletcher, 2000).

The VOF method was applied to the simulation of the turbulent free surface and wave impact problem by Kleefsman *et al.* (2005) and Ganjum *et al.* (2012). Kleefsman *et al.* (2005) used the VOF method together with a local height function to overcome the problem of flotsam. The combination of these two methods was first introduced by Gerrits and veldman (2000) for simulating sloshing on board of a spacecraft. Ganjum *et al.* (2012) used the VOF model coupled with the turbulence model for modeling the tank

numerically to increase the accuracy. Wang and Ren (1999), Ren and Wang (2004) and Xuelin *et al.* (2009) used the VOF method to simulate waves slamming into an object.

The VOF method does not resolve the interface at high Reynolds number with a large density difference between the two flow phases. Velocity jumps occur right at the free surface interface in the VOF method. Thus artificial tearing occurs. In order to mitigate these occurrences, smoothing and filtering is required to reduce the velocity jump (Fu *et al.,* 2010; Brucker *et al.*, 2010). Fu *et al.* (2010) used a density weighted velocity smoother which is effective for simulating the free surface with the VOF method in the applications to modeling bow waves and stern waves. Dommermuth et al. (2006) used the VOF method with piece-wise linear polynomials to simulate ship waves with good results reported.

1.3.2 Level Set Method (LSM)

Recently, the Level Set method has become popular for problems of tracking fluid boundaries and was first introduced by Sussman *et al.* (1994) and Osher and Sethian (1988). In this method, the interface can be modeled sharply. Osher and Sethian (1988) introduced a new algorithm called the PSC scheme for representing a moving surface with free boundaries. The PSC scheme numerically solves the Hamilton-Jacobi equations with a viscous term. This scheme uses the approximation technique from hyperbolic conservation laws.

In general, the level set function is a method of capturing the interface represented by the zero contour of a signed distance function (Olsson and Kreiss 2005). The movement of the interface is governed by a differential equation, and the advection is calculated based on the Weighted and Non-Weighted Essentially Non-Oscillatory methods (WENO, ENO). The level set method represents the two-phase flow approximately using the flow of a single fluid, the physical properties (density and viscosity) vary across the interface. In this method, the fluid density and viscosity are defined as smooth functions of the distance from the interface. The function is continuous at the interface (Iafrati *et al.,* 2001).

Vogt and Larsson (1999) applied this method to the two-dimensional wave problem and achieved good agreement with experimental data. Sussman *et al.* (1994) re-initialized the distance function to keep the thickness of the transition zone constant. They solved the bubble generation function, denoted by the level set function as ϕ, with ϕ taken to be positive outside the bubble, negative inside the bubble and zero at the bubble interface. Application of the single and two-phase Level Set methods to study flow around a container ship can be found in the Cura Hochbaum and Shumann (1999) and Carrica *et al.* (2005).

The advantage of the Level Set method is that using the advection equation and computing the free surface curvature is more accurate than computing these equations with a non-smooth function. Another advantage of the level set method is that a smooth

function distance gives the interface a thickness fixed in time, and density and surface tension both depend on the level set function.

The drawback of the Level Set method is that the method is not conservative (Tornberg and Enhquist, 2000). In problems of incompressible two-phase flow, loss or gain of mass can occur. Several attempts have been made to improve the poor mass conservation of the Level Set method by combining the method with other methods such as VOF (Sussman and Puckett, 2000), the marker particles method (Enright *et al*., 2002) and by exchanging the level set function with a new advection scheme (Olsson and Kreiss, 2005). Olsson *et al.* 2007 introduced a new level set model which is easy to implement for three-dimensional problems. For this model, mass conservation is significantly better than the original level set model.

Our primary interest in this method is for applications of wave interaction with vessels and offshore structures. These applications require robust interface capturing that is accurate and scalable on a high-performance computing platform. The Level Set method is robust over large deformation, and applicable on a large scale with the high Reynolds number flow. Kees *et al.* (2011) introduced a new conservative level set method for modeling wave breaking. The method maintains a sharp and stable air-water interface and shows that the method is accurate for large-scale and complex free surface problems.

Note that, the interface can be defined as a single-phase level set method for which only the water phase of the problem would be solved. This kind of approach has several advantages and disadvantages. A comparison of this approach with the wave – vessel

interaction problem needs shows that the continuity condition will not be satisfied in the air phase. Thus the method is not suitable for problems such as when the air is trapped, or bubbles are formed inside the liquid, or when the air phase gets pressurized (Di Mascio *et al.*, 2004).

1.3.3 Turbulent Models

Most parts of any simulation of wave-vessel interaction such as free surface simulation, wave and wave breakdown, air entrainment and bubble generation, and spray formation require turbulence models. The first use of turbulence modeling for wave-vessel interaction problems is the simulation of a turbulent free surface. Many studies related to the turbulent free surface have been published, such as Melville (1996), Sarpkaya (1986) and Tsai and Yue (1996). Most non-linear and time-dependent free surface models are based on numerical solutions.

Borue *et al.* (1995), used Direct Numerical simulation (DNS) to solve the time-dependent Navier-Stokes equation and continuity equation for open channel flow problems capturing turbulence at the free surface. Komori *et al.* (1993) analyzed the fully non-linear free surface coupled with turbulent flow, but only a small deformation of free surface was considered. Tsai (1998) simulated the interaction between free surface and turbulence with the DNS method.

Brocchini and Peregrine (2001a) reported several features of turbulence at the free surface and described the deformation and breakup of the free surface, based on different

types of turbulence. Turbulence modeling with new boundary conditions, which is introduced for the strong turbulence event, is reported in Brocchini and Peregrine (2001b).

Several approaches for capturing large deformations, turbulence production, and dissipation at the free surface are available. The two-equation $k - \varepsilon$ eddy viscosity model, Large Eddy Simulation (LES), and Reynolds Stress Model (RSM) can all be used. Advantages and disadvantages of some of these model are reported by Ferreira *et al.* (2004). The results of implementing the two-equation $k - \varepsilon$ eddy viscosity model for high-Reynolds number, for two cases of turbulent boundary layers on a flat plate and jet impingement flow, were examined and reported by Ferreira *et al.* (2004) and were showed satisfactory in comparison with the experimental data.

Yue *et al.* (2003) used the LES method with the Level Set (LS) method to numerically simulate turbulent free surface flow, and calculated the effect of surface tension. The LES method attempts to resolve motions accounting for the bulk of the turbulent kinetic energy and can be applied to relatively high Reynold number in even complex flows, which cost significantly less than the DNS method. The DNS method should only be applied for low Reynolds numbers with simple geometries; the method attempts to resolve the energy dissipation scale (Kolmogorov) of turbulent motions, which makes DNS an extremely expensive method.

Besides the free surface simulation, waves and wave breakdown under the influence of turbulence are another challenge in simulating the wave-vessel impact problem. Lin

and Liu (1998a, b) and Bradford (2000) modeled a wave train and wave breaking by solving RANS equations and the $k-\varepsilon$ equations. The non-linear Reynold stress model (RSM) was used in this simulation and agreement was achieved between the numerical simulation and the experimental data. Bradford (2000) compared the performance of the $k-\omega$ model, $k-\varepsilon$ model and the Renormalized Group model (RNG) with experimental data from Ting and Kirby (1995; 1996) and Lin and Liu (1998a; 1998b). All of the models generally show satisfactory agreement; however, the wave breaking incident occurred earlier than usual in the experiment, which might not be a significant factor in modeling the wave-vessel impact. Zhao *et al.* (2004) used the VOF method to track the interface and applied a log-law profile for the mean velocity. They compared their results with the RANS model and they show an improved outcome compared with the experimental data.

The three-dimensional LES method and the DNS method were used to simulate breaking waves by Christensen and Deigaard (2001) and Wijayaratna and Okayasu (2000), respectively. The results show a satisfactory agreement with experimental data, but the usage of these two methods in three-dimensional modeling is computationally time-consuming.

Another factor involved with turbulence is air entrainment. High void fraction and strong turbulence breakup occur in the air entrainment and bubble generation process. Moraga *et al.* (2008) employed RANS and Reynolds stress closure models which are used in the case of low spatial resolution and the results were compared with the experiments of Waniewski *et al*. (2001) for measuring the location of a bubble source. Carrica *et al.*

(1999) show that all processes involving bubble generation, such as bubble collision, bubble coalescence, and bubble breakup should be considered and modeled with a turbulence model.

1.4 Maximum Entropy Principle (MEP)

Modeling the distribution of droplet size and velocity is essential in the study of spray cloud formation, and the size distribution and velocity are crucial parameters for the fundamental analysis of droplet trajectories upside of the bow of a vessel (Dehghani *et al*. 2016a; 2016b). Typical analytical models for predicting the size and velocity of droplets are extracted from experimental data and measurements for small-scale events, such as spray formation from a nozzle. Examples of these distributions are the Rosin-Rammler distribution (Rosin-Rammler, 1933), and the Nukiyama-Tanasawa distribution (Nukiyama-Tanasawa, 1939). The interested reader can refer to a review paper by Babinsky and Sojka (2002) for broad spray distribution models.

More recent studies use statistical approaches to predict more general droplet sizes and velocity distributions. The MEP method has become popular for the prediction of droplet sizes and velocity distributions because it produces reasonably accurate results. Sellens and Brzustowski (1985, 1986) and Li and Tankin (1987, 1988) were the first to introduce this method. Since the theory of this method has been well described by these researchers, the background materials are not covered in this thesis. The method assumes that while the system entropy is maximized and conservation equations (mass,

momentum, and energy) are satisfied, the equation for size distribution will be equally satisfied.

The MEP method has been upgraded for different conditions, and the effects of several phenomena were added over the past two decades. Kim *et al*. (2003) used the MEP and instability analysis of liquid sheets to consider the effect of the instability of liquid jets in their model. Huh *et al*. (1988) consider the effect of turbulent conditions for diesel sprays in conjunction with the MEP model.

The MEP was originally introduced for predicting the droplet size and velocity distribution of diesel spray from a nozzle. However, in the current study, the MEP applied to spray production due to wave interaction with marine objects. Similarly, after the wave impact, the water forms a liquid sheet, which is the same as the non-homogenous, inverted hollow cone that exits from a nozzle with one side of the cone attached to the marine structure. Afterward, it breaks up into ligaments that form droplets.

1.5 Analytical Approach

The process of water delivery and spray production from wave impact is a multifaceted engineering problem and consists of various complex phenomena. The process can be divided into five regimes, 1) wave impact, 2) air entrainment, 3) high-speed water sheet formation, 4) water sheet and ligaments breakup, and 5) spray cloud formation (Bodaghkhani *et al.,* 2016; Dehghani-sanij *et al.,* 2017a; 2017b). Ability to develop a model to consider all the five mentioned regimes in one mathematical

formulation for predicting the final average droplet diameter of spray cloud due to wave impact is essential. In this section, the background literature related to all the components that are used to develop a comprehensive analytical model for this prediction was reviewed.

Wave characteristics at the moment of impact including wave horizontal and vertical velocities are discussed in several references (Bhattacharyya 1978, Airy 1845). In the present case, basic harmonic deep water wave formulation and second-order Stokes theory wave formulation are used (Stokes 1880, Rayleigh 1917, Fenton 1990). Various scaling laws for wave impact and air entrainment have been proposed in investigating wave behaviors. Froude scaling is applied to the waves prior to impact, and the Bagnold-Mitsuyasu scaling law is used for impacts with a high level of aeration and air entrainment (Bagnold, 1939; Bredmose *et al.,* 2015).

Besides the wave impact and aeration criteria, the water sheet formation, breakup, and droplet formation are significant mechanisms in the spray production and water delivery process (Bodaghkhani *et al.,* 2016; Dehghani *et al.,* 2016a; 2016b). After impact, compressed air trapped by the impact pressure accelerates the water and forms a high-velocity sheet of liquid (Ryerson, 1995). This high-velocity sheet of water breaks up and follows scaling laws dictated by Reynolds and Bond numbers. Then, droplets are formed from the breakup of water sheet ligaments, and the Weber number becomes a significant non-dimensional number (Bilanin, 1991). General physical discussion regarding the water sheet and droplet breakup will be discussed in detail in Chapter 4.

The Froude scaling law no longer applies in the presence of trapped and entrained air for wave impact with an object, nor for wave impact involved in the wave crest overturning (Bredmose *et al.,* 2009; 2015). In these cases, the Froude scaling law is influenced by the compressibility effects of a change of fluid pressure relative to atmospheric pressure and aeration due to wave breaking. Several researchers analyzed the effects of compressibility on the maximum wave pressure. Blackmore and Hewson (1984) demonstrated that the pressure ratio for the scale ratio of $1:20$ does not follow the Froude, scaling model. They suggested a formula for peak pressure as $p_{max} - p_0 = \lambda \rho_w T c_b^2$, in which T is the wave period, c_b is the wave phase speed, and λ is a parameter with units of s^{-1}, which varies for different scales.

Lugni *et al.* (2010) suggested that the compressibility of an air pocket increases with the Euler number $(Eu = 2(p_0 - p_{ullage})/(\rho_w u_0^2))$, and decreases based on the Cavitation number $(Ka = 2(p_{ullage} - p_v)/(\rho_w u_0^2))$. This study was based on wave impact with an air cavity in a 2-D sloshing test. The value of the air pressure inside the tank in the still water condition, the so-called ullage pressure, strongly influences the initiation and the evolution of bubbles during the impact. Many authors considered a 1-D piston analogy of Bagnold (1939) for the air entrapment process in wave impact. This model suggests that the relationship of $p_{max} - p_0 = 2.7 \rho_w u_0^2 K/D$ is applicable to the air pocket entrainment for water impact. In this equation, K and D are the initial amplitude of the impacting water wave and the diameter of the trapped air pocket respectively. Takahashi *et al*. (1985) suggested a dimensionless number extracted from Bagnold's

results, which they called Bagnold number. They proposed that in the case of wave slamming on a wall, the maximum pressure is a function of the dimensionless number $Bg = \rho_w u_0^2 K/(p_0 D)$. Cuomo *et al*. (2010a; 2010b) provided a method for estimating $K, D,$ and u_0 from the wave parameters. The variable K is proportional with $\sqrt{H_0}$, in which H_0 is the significant wave height; variables D and u_0 are directly proportional to H_0.

Besides the air trapped at the moment of impact, aeration has an effect on the decrease of maximum pressure. Several experiments and field data observations were performed to analyze the effect of aeration on the reduction of maximum pressure. Bullock *et al*. (2001) showed that this reduction at laboratory test scale is approximately 10% for salt water. Bredmose *et al*. (2015) used a scaling analysis method for aerated wave impact and showed that for the Froude scaled model, the normalized maximum pressure ($(P_{max} - P_0)/P_0$) is a function of the initial aeration ($\beta_0(x)$) and the ratio of dynamic pressure to the atmospheric pressure ($\rho_w u_0^2/P_0$). Bredmose *et al*. (2015) generalized the Bagnold-Mitsuyasu scaling law for any situation in which all the kinetic energy within a certain fluid region goes into the compression of an air pocket. This paper indicates that the velocity scale ratio for aerated impact flow is proportional to $\sqrt{P}$, and Bredmose *et al*. (2015) generated a general figure for relating the lab-scale to full-scale models based on the Bagnold-Mitsuyasu scaling law, Froude law, and asymptotes related to these curves.

Following the stage involving the wave, wave impact pressure, air entrainment, and maximum impact pressure, the next stage of the process which involves parameters related to the instability and disintegration of the liquid sheet and the formation of droplets, is considered. Scaling parameters related to the breakup of the liquid sheet and droplet formation are considered as the next step in the model. Most authors in this area reference the work of Rayleigh (1879), who recognized two linearly independent mode shapes for the liquid sheet: the sinuous mode and the varicose mode. The early work of Fraser *et al*. (1962) presented a model for the breakup of a flat, inviscid sheet with the sinuous mode of wave growth. Dombrowski and Johns (1963) introduced a model for viscous liquid sheets. Altieri *et al.* (2014) reviewed the previous research related to liquid sheets and developed a model to represent mechanisms of sheet disintegration and droplet formation for spray nozzles.

This chapter is written based on: Armin Bodaghkhani, Joshua R. Dowdell, Bruce Colbourne, Yuri S. Muzychka, Greg F. Naterer, Measurement of spray-cloud characteristics with bubble image velocimetry for braking wave impact, In Cold Regions Science and Technology, Volume 145, 2018, Pages 52-64, ISSN 0165-232X.

Chapter 2 Experimental Simulation

The primary focus of this chapter is to report the measurements of the droplet size and velocity for the process of spray cloud formation. The work covered in this chapter applies the BIV technique to measure spray characteristics and flow kinematics due to wave impact using two models: a flat-shaped plate and a bow-shaped plate model. The process of wave impact to spray production was examined qualitatively. Flow velocity near the impact domain is obtained with the Bubble Image Velocimetry (BIV) technique. For validation, the results of the BIV method from the side view are compared with the results of DPIV method from the front view as well as results of the BIV and PIV measurements reported by Ryu *et al*. (2005) and velocity measurements of Chang *et al*. (2003), which used Fibre Optic Reflectometry (FOR) for measuring the velocity field. Wave characteristics and impact pressure are measured with several pressure sensors and wave probes and compared with experimental results by Fullerton *et al*. (2010).

2.1 Experimental Setup

The experiment was conducted in a $57.4\,\mathrm{m}$ wave tank located in the Ocean Engineering Research Center at Memorial University of Newfoundland's Faculty of Applied Science and Engineering. This tank is $57.4\,\mathrm{m}$ long, $4.5\,\mathrm{m}$ wide, and a maximum depth of $H_t = 3.04\,\mathrm{m}$. It has a single piston board-style wave-maker, which is driven by a single $3{,}000\,\mathrm{PSI}, 125\,\mathrm{hp}$ hydraulic drive. The other end contains a wave damping beach that serves as a wave energy absorber and reflection reducer. The water depth is kept

at $\mathrm{H} = 1.9\ \mathrm{m}$. A tow carriage supports the simulated hull models and is located approximately at the tank's midway point. Despite the significant effect of wind on breakup process, air surrounding the model kept calm at all time.

Due to the high wave energies required to create a spray, strength and rigidity were primary concerns in model development. The other priority was to create a laboratory-scale model that had the ability to let the water experience breakup in the same way as full-scale vessels. A height of $\mathrm{h} = 1\ \mathrm{m}$ for the models was considered adequate to balance these two requirements. The first model was a flat-shaped plate with a height of $\mathrm{h_f} = 1\ \mathrm{m}$, a width of $\mathrm{b_f} = 0.7\ \mathrm{m}$, and $0.2\ \mathrm{m}$ wide side plates. The shape of the second model approximated that of a ship's bow. It had a narrower front face and side plates with variable flare angles, which can be mounted on the carriage with different stem angles with respect to the vertical axis. The dimensions of this model were $\mathrm{h_b} = 1\ \mathrm{m}$ in height, $\mathrm{b_b} = 0.15\ \mathrm{m}$ in width and $0.3\ \mathrm{m}$ wide side plates. Additionally, $0.2\ \mathrm{m}$ of each model was submerged in the water, and the intersection between the free surface level and middle of the models is set as origin $\mathrm{O}(0, 0, 0)$.

The free surface variations due to the wave height passing several positions were measured with capacitive wave probes. Three probes were used to measure the far-field wave height, the wave height at the point of impact, and the wave reflection after impact. The far-field probe (WP1) was located at a $1\ \mathrm{m}$ distance from the model to avoid impact-wave reflection in the negative x-direction, and the point of impact probe (WP2) was located exactly in front of the model to measure the wave height at the moment of impact

and the wave reflection. The reflection probe (WP3) was located 0.6 m from the model but in the same plane (Fig. 2-1b). It should be noted that the wave probes are not located in front of the camera, and are located such that they do not conflict with the image capturing.

Wave breaking processes in the laboratory for comparisons with a real scale are challenging to predict numerically. Several authors demonstrated similarity between a breaking wave in the laboratory and the actual scale. Philips (1985) presented a model for the distribution of the breaker front length, which leads to the momentum flux from the wave field into the upper ocean and the total gravity wave energy dissipated by breaking waves. Several other past studies such as Melville (1994) and Drazen *et al.* (2008) improved the equations by Philips (1985) and compared the breaking wave in the laboratory with a real scale ocean breaking wave. Further, recent work of Sutherland and Melville (2013) introduced a dimensional analysis for predicting the distribution of the breaker front length. In the current study, a non-dimensional study by Sutherland and Melville (2013) was used to determine the wave characteristics that are compatible with the wave data presented by Ryerson (1995).

A qualitative measurement of spray characteristics was acquired with a high-speed camera. A Phantom $V611$ high-speed camera was placed in two different positions in relation to the test model: a side view through the tank windows for lateral and vertical spray, and a front view for spray distribution along the width of the models. The distances between the camera and center of both objects for the side view and front view are kept

at $2.30\ m$ and $1.7\ m$, respectively. For BIV technique several LEDs were used on one side, and these lights were diffused by an acrylic plastic sheet. Several other LED and DC light fixtures were used to increase the brightness and quality of the captured videos. The BIV method was used to analyze the aerated area and the backlighting technique leads to sharp images. The camera frame rate was fixed at $1000\ \mathrm{fps}$ with a fixed resolution of 1024×768 pixels. Due to restrictions on the Field of View (FOV), the camera was aimed either at the lower position of the sheet formation or the higher position looking at the spray heights. Adequate lighting was used for the camera to obtain sharp and clear images.

Nova Sensor model $\mathrm{NPI} - 19$ medium pressure sensors were used. These sensors were located on the model at $27.5\ \mathrm{cm}\ (\mathrm{A})$, $30\ \mathrm{cm}\ (\mathrm{B})$, $32.5\ \mathrm{cm}(\mathrm{C})$, $35\ \mathrm{cm}\ (\mathrm{D})$, and $37.5\ \mathrm{cm}\ (\mathrm{E})$ from the bottom of the model to capture the distribution of wave impact pressure. Each sensor contains a piezoresistive sensor chip inside a hermetically sealed diaphragm housing. External threading allowed the sensors to be flush-mounted to the model test rig. The justification for using these particular sensors is found in Fullerton *et al*. (2010). The schematics of the experiment, which demonstrate different FOV (side and front), are shown in Figs. (2-1a) and (2-1b), respectively. As is shown in Fig. (2-1a), two different FOV were considered in this experiment: FOV1 for studying the spray and measuring droplet characteristics, and FOV2 for analyzing the behavior of a wave at the time of impact, as well as water sheet production arising from the impact, in which both FOV have dimensions of $600 \times 450\ \mathrm{mm}$.

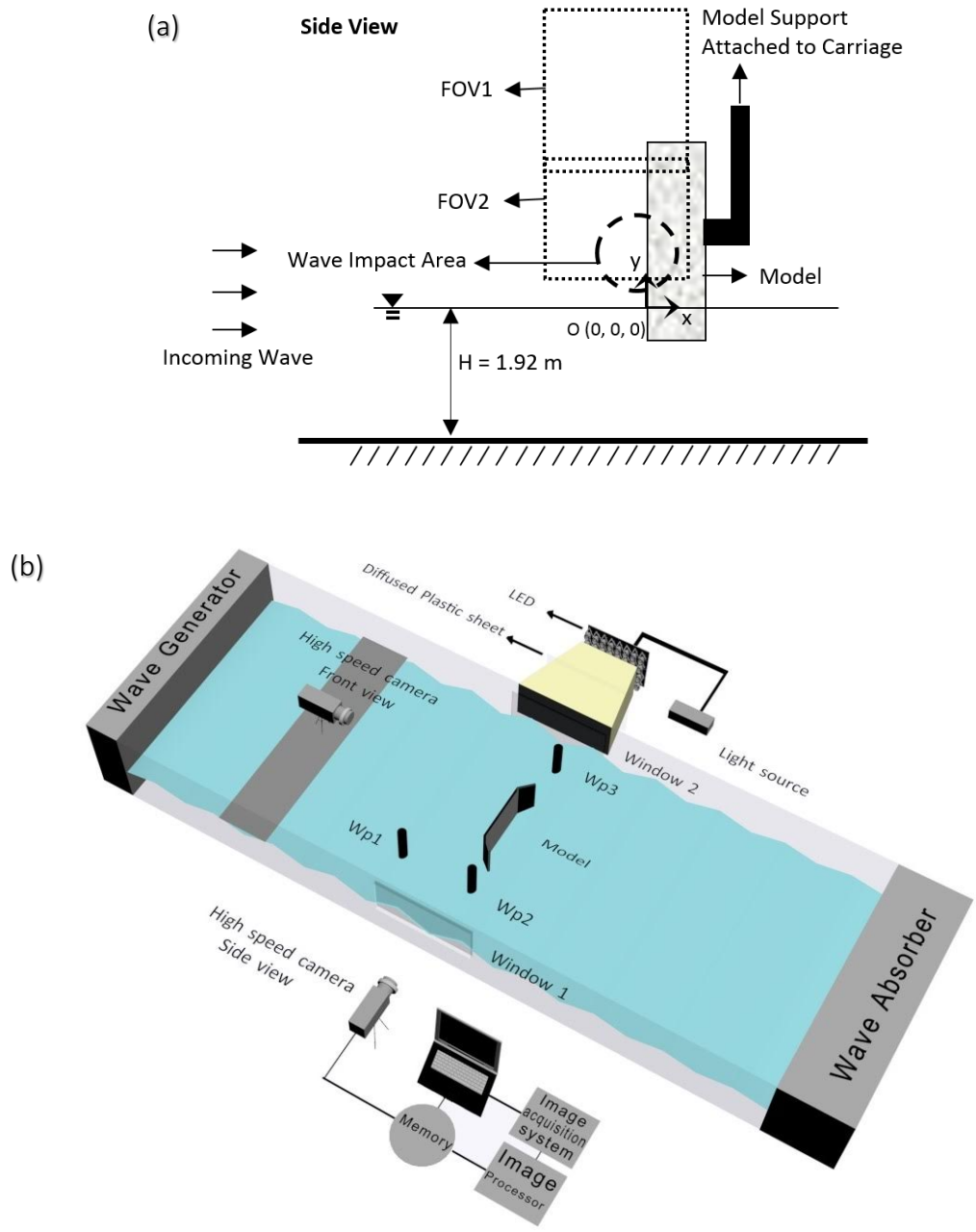

Fig. 2-1 Model structure and FOV of the experiment for both (a) side view, (b) 3-D schematic view and the BIV apparatus.

The DPIV technique was used to calculate velocity and droplet size and to track droplet detached from aerated regions. This method of computationally analyzing digital video

images removes both the photographic and optomechanical processing steps inherent in PIV and Laser Speckle Velocimetry (LSV). The method, first introduced by Willert and Gharib (1991), has been upgraded by various researchers.

DPIV and BIV techniques are restricted and controlled by a narrow Depth of Field (DOF). Ray (2002) suggested adjusting the camera aperture and the distance from the camera lens to the center of measurement in front of the object. DOF is defined as the distance near the object captured by the camera, which is well focused and sharp. Due to the narrow DOF, errors related to displacement in the image, which is further correlated to velocity, were reduced. Detailed correlation and a discussion regarding finding the DOF can be found in Ryu *et al*. (2005). However, Ryu *et al*. (2005) reported velocity measurements in both sharp and blurred images as independent from DOF methodology.

Several sample images of DPIV and BIV studies are shown in Fig. (2-6). These show the several stages of image filtering, morphological steps, and noise reduction as well as droplet detection. Due to the algorithms for image filtering, thresholding, and background subtraction in this study, only some samples are shown in Fig. (2-6). In this study, boundaries that are out of the focal plane of the camera and appeared blurry in the image were removed from the ensemble averaging. Droplet detection from these images was used for further post-processing such as size and velocity detection.

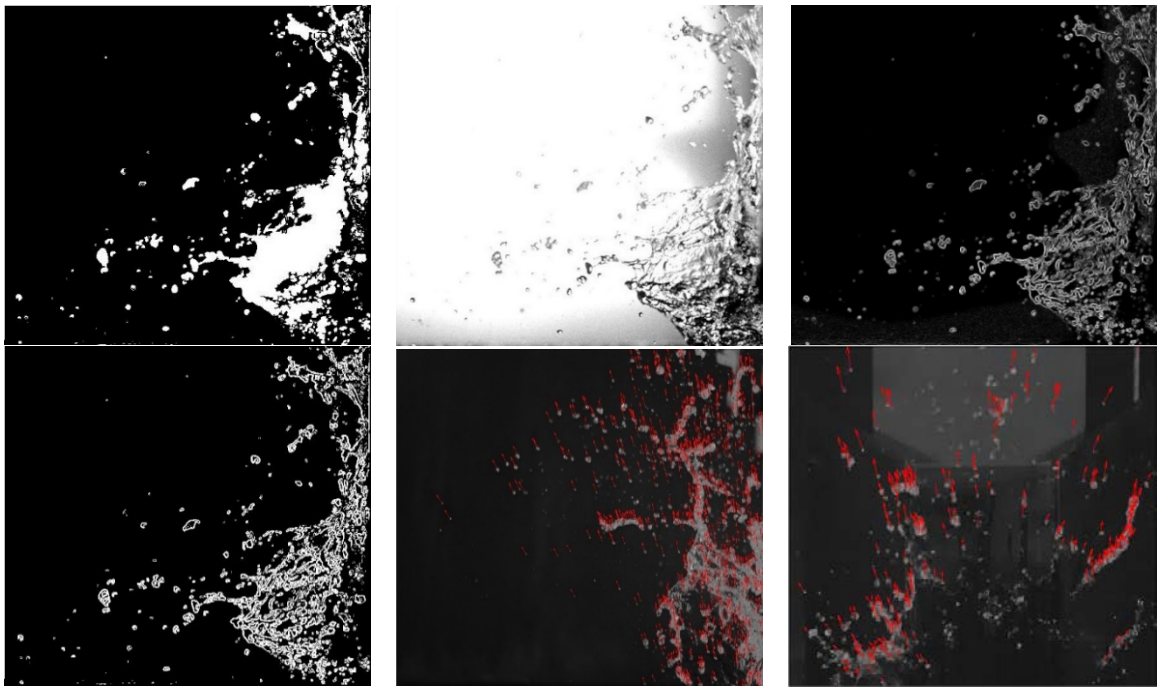

Fig. 2-2 Sample raw images of side and front views of the water droplet and jet formation using several algorithms and image filtering for noise reduction, morphological steps, background subtraction, and droplet detection as well as velocimetry.

The waves in the tow tank were calibrated for ensuring that the wave board span and frequency set points were accurate and that wave amplitudes were generated accordingly. Wave probes and pressure sensors were calibrated separately and prior to use to ensure proper measurements. The camera calibration was conducted by taking images from a square checkerboard pattern panel of known and uniform width. These checkerboard images were placed in the focal plane of the camera and the midpoint of the FOV.

2.2 Experiment Uncertainties

The precision error for the pressure sensors and wave probes was calculated by recording values when the overall data acquisition system was running under normal conditions. For each wave characteristics, 20 measurements were taken from each pressure sensor as well as from each wave probe. A total of 400 measurements from five pressure sensors and 240 from three wave probes were taken for all the wave characteristics and trials. The bias errors were assumed to be a common estimate of 0.5% based on the spec sheets of both pressure sensors and wave probes. The precision error for pressure sensors and wave probes was calculated as 1% and $4.7\ \%$. The bias and precision errors based on Kline and McClintock (1953), $\mathrm{U_{x,i}} = (\mathrm{P_{x,i}^2} + \mathrm{B_{x,i}^2})^{1/2}$ represent uncertainties, which for pressure sensors and wave probes uncertainties are calculated as 1.1% and 4.8%. Because the water level was not quite at the start of each trial, the precision error for the wave probe reading of the water surface elevation is relatively large.

The uncertainty due to the wave period (T) readings can be attributed to the resolution of the x-axis that represents the distance between two peaks of a wave, which is the time step of the data acquisition ($\Delta \mathrm{t} = 1 \times 10^{-5}$). The wavelength $\lambda = \mathrm{g}T^2/2\pi$, as given by Bhattacharyya (1978), and its precision and bias errors can be calculated based on an equation by Kline and McClintock (1953). The same procedure is performed to measure the uncertainties of the wave phase velocity $V_c = \sqrt{g\lambda/2\pi}$. The uncertainties in

the calculation of wave period, wavelength, and wave phase velocity are estimated as 0.5%, 1%, and 2.2%, respectively.

The error created by the DOF limitation is calculated based on a formulation according to Ray (2002) for the nearest (R) and farthest limit (S) for camera aperture. The DOF is calculated as $\mathrm{D} = \mathrm{S} - \mathrm{R}$, and the error associated by the DOF can be estimated as $\varepsilon = \mathrm{D}/2\mathrm{l}$, where l is the distance between the camera and the center of the camera's focal plane. For the flat-plate model, by considering $\mathrm{D} = 0.2\ \mathrm{m}$ and $\mathrm{l} = 1.7\ \mathrm{m}$ for both side and front views, ε is calculated as 5.8%. For the bow-shaped plate model, by considering $\mathrm{D} = 0.2\ \mathrm{m}$ and $\mathrm{l} = 2.3\ \mathrm{m}$ for both side and front views, ε is calculated as 4.3%

The limits of resolution and the level of uncertainty of the DPIV technique is described in detail by Willert and Gharib (1991). The statistical uncertainty in the measurements was reported by taking into account the effects of noise in the acquisition system, as well as numerical noise generated by particle images being truncated on the edges of a pixel window with a size of 32×32. The lowest uncertainty for the DPIV method is about 0.01 pixels to a maximum of 0.15 pixels, which is dependent on the amount of droplet displacement. In this analysis, more than 100 droplets were examined in most of the trials, in which increasing the number of droplets leads to the uncertainties increase. For this case, the uncertainties are calculated as 0.1 pixels, which for the largest droplet is calculated as 0.05% and for highest droplet velocity with longest displacement distance is calculated as 0.1%.

2.3 Wave Conditions

Image processing was performed for the waves and wave-crest types that were able to produce a spray. Those wave conditions that could produce a spray were determined by trials, which systematically varied the wave generator input characteristics. The different behaviors of water break-up in the experiment forced the use of various wave characteristics. All runs were repeated 5 times for the sake of experiment repetitiveness. The wave-crest types, the wave impact pressure, and types of the break-up after wave impact were considered as criteria for choosing a particular wave for further calculations. Table 1 shows the wave characteristics that were used for both models and are limited to those that generate spray. For producing the spray from the wave impact, the breaking waves were chosen, which are stronger than the regular sinusoid waves. Experimental results show that the regular sinusoid waves do not have enough kinetic energy and enough velocity to produce spray after the impact. This problem causes significant errors in measuring the wave characteristics such as wavelength and wave phase velocities, however in this experiment wave characteristics were calculated based on the deep water wave formulation (Bhattacharyya, 1978). A combination of the frequency and span that were used are aligned with the wave heights, wavelengths, wave periods, and wave phase velocities and are presented in Table 2-1.

It should be noted that wave characteristics combinations that produce wave phase velocities lower than $1.45\ m/s$ are not forming spray after the impact and waves with higher wave phase velocities ($> 1.85\ m/s$) was very strong, which may cause damage to

our experiment facility. The following combinations were chosen based on the experiment limitations. In addition, three different wave impact types were observed in this experiment. First, swell type impact (sloshing) was observed. This occurs when the impact happened before the moment that a wave reaches the breaking point and the moment that wave impact after the wave breaking occurs (Fig. 2-3a). This type of impact usually has a low kinetic energy and does not produce spray. Second, the waves that completely break, when they meet the model (Fig. 2-3b), are called flip-through impact. This type of impact is the primary focus of this experiment.

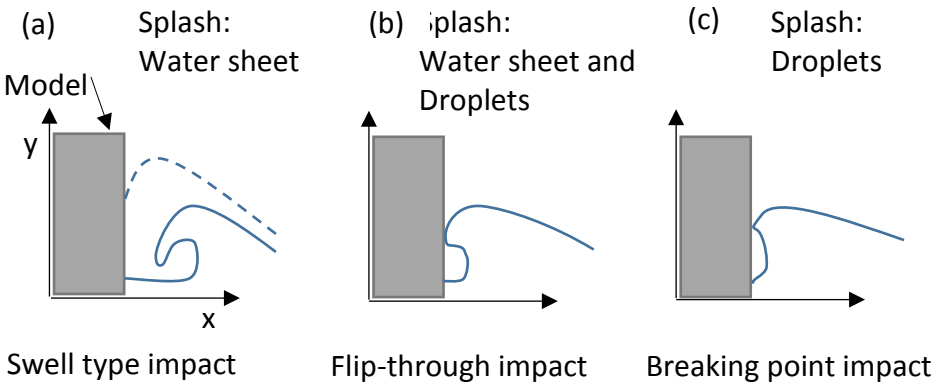

Fig. 2-3 Schematic demonstration of three types of impact.

Finally, the breaking point impact, which happens when the impact occurs exactly at the moment that a wave starts to break and the wave crest is starting to overturn (Fig. 2-3c). This kind of impact is violent and produces very high-speed droplets without any sheet. This type of wave impact is not considered in this study. Two primary waves that are chosen from the train of waves to impact the wall are focused such that they break

exactly when they meet (flip-through impact). Due to the restriction of the wave generator, there were errors associated with this procedure, which caused some waves to not entirely to break at the impact point. However, errors are reduced by increasing the number of trials and choosing the right test to meet the criteria.

Table 2-1 Experimental wave characteristics.

Span (%)	Frequency (Hz)	Wave Height WP1 (mm)	Wave Height WP2 (mm)	Wave Length (m)	Period (s)	Wave Phase Velocity (m/s)
50	0.85	276	289	2.08	1.16	1.80
40	0.95	233	232	1.72	1.05	1.64
35	1	208	213	1.59	1.00	1.57
50	0.95	233	253	1.42	1.04	1.48

Waves were generated by sending an external voltage signal made up of 10 waves with the same span and frequency. Single sample output data from both the side-parallel and far-field wave probes are shown in Fig. (2-4).

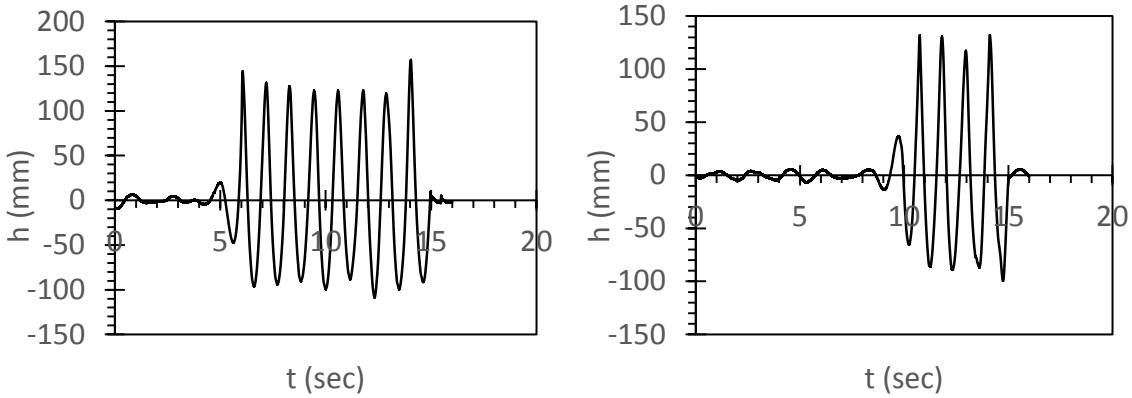

Fig. 2-4 Time history of water free surface elevation (h) for a sample wave with wave height of $253\ mm$ from (a) far-field wave probe (WP1), (b) side-parallel wave probe (WP3).

Pressure measurements were performed for all trials with 5 iterations for each wave characteristics. From the experimental trials, the breaking waves that were impacted when the wave is completely overturned and the breaking wave that impacts the wall at the moment of overturning were picked for further post-processing measurements. A small number of waves behaved differently in varying iterations, which were counted as experimental errors. To avoid the effect of reflected waves on spray-cloud quality, only the first two waves that impacted with the models are considered for measurements and further image processing. The average of wave height and wave velocity of the first two waves were considered for further calculations. It should be noted that because there is not any reflection at the beginning of the impact, the first two waves were almost identical.

This chapter is written based on:

1. Armin Bodaghkhani, Yuri S. Muzychka, Bruce Colbourne, 3-D numerical and experimental simulation of spray-cloud formation due to wave-body interaction, In Second Thermal and Fluids Engineering conference, 2017, ISSN: 2379-1748.
2. Armin Bodaghkhani, Yuri S. Muzychka, Bruce Colbourne, 3-D numerical and experimental simulation of wave run-up due to wave impact with a vertical surface, In Journal of Fluid Engineering, (Under Review).

Chapter 3 Numerical Simulation

For solving this wave-body interaction problem, transient incompressible two-phase flow Navier-Stokes equations and turbulent flow at the interface were considered. The numerical model is treated as a multiphase problem, which includes a liquid phase (water), a gas phase (air), and an object dealt with as a solid. The object is considered to be fixed with waves moving towards it. The frame of reference is considered fixed in regards to the position of the object. By assuming that there is no temperature variation in this problem, the continuity and transport momentum equations are:

$$\nabla.(\vec{v}) = 0 \tag{3-1}$$

$$\frac{\partial}{\partial t}(\vec{v}) + (\vec{v}.\nabla)\vec{v} = -\frac{\nabla \mathrm{p}}{\rho} + \nabla.(\vec{\tau}) + \vec{g} + \frac{\vec{F}}{\rho} \tag{3-2}$$

where ρ is density, $\vec{v}$ is three-dimensional velocity field as a function of three-dimensional space ($x_i = (x, y, z)$) and time (t). $\vec{g}$ is the gravitational body force and $\vec{F}$ is an external body force. The stress tensor $\vec{\tau}$ is given by:

$$\vec{\tau} = \nu(\nabla \vec{v} + \nabla \vec{v}^T - \frac{2}{3}\nabla.\vec{v}\, I) \tag{3-3}$$

where ν is the kinematic viscosity and I is the unit tensor. Eqs. (3-1) and (3-2) are the governing equations for solving flow in this problem, and are solved numerically based on the projection method, which is called the decoupled or segregated method (Chorin 1968), and operated as a two-stage fractional step.

3.1 Turbulence Model

The realizable $k-\varepsilon$ model is the turbulence model considered for this problem because of its robustness, expense, and high accuracy compared with other models. The realizable $k-\varepsilon$ model is different from the conventional $k-\varepsilon$ model: it contains a new eddy-viscosity formula and a new equation for solving the dissipation rate (ε). The following equations are introduced for this model as:

$$\frac{\partial k}{\partial t}+\frac{\partial}{\partial x_j}(ku_j)=\frac{1}{\rho}\frac{\partial}{\partial x_j}\left[\left(\mu+\frac{\mu_t}{\sigma_k}\right)\frac{\partial k}{\partial x_j}\right]+\frac{G_k}{\rho}-\varepsilon \tag{3-4}$$

$$\frac{\partial \varepsilon}{\partial t}+\frac{\partial}{\partial x_j}(\varepsilon u_j)=\frac{1}{\rho}\frac{\partial}{\partial x_j}\left[\left(\mu+\frac{\mu_t}{\sigma_\varepsilon}\right)\frac{\partial \varepsilon}{\partial x_j}\right]+\varepsilon\,.\,C_1S-C_2\frac{\varepsilon^2}{k+\sqrt{\nu\varepsilon}} \tag{3-5}$$

where $C_1=\max\left[0.43,\frac{\eta}{\eta+5}\right]$, $\eta=S\frac{k}{\varepsilon}$, $S=\sqrt{2S_{ij}S_{ij}}$, and $S_{ij}=\frac{1}{2}(\frac{\partial u_i}{\partial x_j}+\frac{\partial u_j}{\partial x_i})$.

In Eqs. (3-4) and (3-5), G_k represents the generation of turbulence kinetic energy and is equal to $\mu_t S^2$ and $\mu_t=\rho C_\mu {k^2}/{\varepsilon}$, which is called turbulent viscosity, where C_μ is not constant compared with the standard $k-\varepsilon$ model. This is calculated as $C_\mu=$

$(A_0 + A_s \frac{k\sqrt{S_{ij}S_{ij}}}{\varepsilon})^{-1}$, where $A_0 = 4.04$, $A_s = \sqrt{6}\cos\phi$, and $\phi = 1/3\cos^{-1}(\sqrt{6}\cos^{-1} S_{ij}S_{jk}S_{ki}/(\sqrt{S_{ij}S_{ij}})^3$. In Eqs. (3-4) and (3-5), $C_2 = 1.9$, $\sigma_k = 1.0$, and $\sigma_\varepsilon = 1.2$. ρ and μ are density and viscosity respectively.

3.2 Volume of Fluid and Level Set Method (LSM)

VOF is used for modeling two immiscible fluids, which tracks the volume fraction of both fluids by solving a single set of momentum equations. If the p^{th} fluid's volume fraction in the cell is donated as a_p then:

$$\begin{cases} a_p = 0 & (when\ cell\ is\ empty) \\ a_p = 1 & (when\ the\ cell\ is\ full) \\ 0 < a_p < 1 & (when\ both\ fluids\ are\ present\ in\ the\ cell) \end{cases} \quad (3\text{-}6)$$

The solution of the continuity equation was used to track the interfaces between the phases, which is represented by the following formula for the p^{th} phase:

$$\frac{\partial a_p}{\partial t} + \nabla.\left(a_p \vec{v}_p\right) = 0 \quad (3\text{-}7)$$

and the primary phase (air) volume fraction equation is computed based on:

$$\sum_{p=1}^{n} a_p = 1 \quad (3\text{-}8)$$

In this work, a Geometric Reconstruction Scheme was used for representing the interface between fluids, which is a piecewise-linear approach based on the work of Youngs (1982). In this method, the interface between two fluids is assumed to have a linear slope within each cell, and this linear shape is used for calculating the advection of fluid through the cell faces. The first step in this reconstruction scheme is calculating the position of the linear interface relative to the center of each partially-filled cell, based on information about the volume fraction and its derivatives in the cell. The second step is calculating the advecting amount of fluid through each face using the computed linear interface representation and information about the normal and tangential velocity distribution on the face. The third step is calculating the volume fraction in each cell using the balance of fluxes calculated during the previous step. In this numerical simulation, the implicit scheme was used to discretize the volume fraction equation, which will be discussed in section 3.3. The LS method (Osher and Sethian 1988; Sussman and Puckett 2000) was coupled with the VOF model to use the advantage of a level set function, which is defined as a signed distance from the interface, is smooth and continuous, and which will increase the accuracy of the interface calculation. A coupled method was used to prevent the discontinuous disadvantage of a VOF model. The level set function φ is taken as a signed distance from the interface and defined mathematically in a two-phase flow system as:

$$\varphi(x,t) = \begin{cases} +|d| & if\ x \in primary\ phase \\ 0 & if\ x \in \Gamma \\ -|d| & if\ x \in secondary\ phase \end{cases} \quad (3\text{-}9)$$

where $\Gamma = \{x \mid \varphi(x,t) = 0\}$.

Viscosity and density in each cell in the transport equations are determined by Eqs. (3-10) and (3-11), in which subscript 1 and 2 represent each phase as:

$$\rho = \alpha_2\rho_2 + (1-\alpha_2)\rho_1 \quad (3\text{-}10)$$

$$\mu = \alpha_2\mu_2 + (1-\alpha_2)\mu_1 \quad (3\text{-}11)$$

3.3 Numerical Schemes

The least squares cell-based method was used to construct the values of a scalar at the cell faces and for computing secondary diffusion terms. This method is computationally less expensive than other models because of the linearity assumption (ANSYS Fluent theory guide). A pressure-based solver was used to solve the governing equations sequentially. In the segregated pressure-based solver, the governing equations for the solution variables are solved one after another. Discretization of each scalar quantity ψ was performed by considering the unsteady conservation equations for the transport of that quantity. The discretization equation of the equation of transport in

integral form, which is applied to each cell in the computational domain, are shown in Eqs. (3-12) and (3-13), respectively.

$$\int_V \frac{\partial \rho\psi}{\partial t} dV + \oint \rho\psi\vec{v}.d\vec{A} = \oint \Gamma_\psi \nabla\psi.d\vec{A} \tag{3-12}$$

$$\frac{\partial \rho\psi}{\partial t} V + \sum_h^{M_{faces}} \rho_h \psi_h \vec{v}_h.\vec{A}_h = \sum_h^{M_{faces}} \Gamma_\psi \nabla\psi_h.\vec{A}_h \tag{3-13}$$

where ρ is the density, $\vec{v}$ is the velocity vector, $\vec{A}$ is surface area vector, and Γ_ψ is the diffusion coefficient for ψ. M_{faces} is the number of faces of the cell, ψ_h is the value of scalar ψ on face h, and subscript h represents the specific quantity at the h^{th} cell. Eq. (3-13) is nonlinear and contains the unknown scalar of variable ψ at the cell center and in surrounding neighbor cells. The proper linear form of Eq. (3-13) is:

$$\alpha_f \psi = \sum_{nb} \alpha_{nb} \psi_{nb} \tag{3-14}$$

where α_f and α_{nb} represent the linearized coefficient of ψ and ψ_{nb}, in which subscript nb represents the neighboring cell.

The momentum and both turbulent equations are discretized based on the QUICK scheme (Leonard and Mokhtari, 1990; Leonard, 1979), which is more accurate because of the structured mesh that is used in this problem. The pressure equations for the VOF method are solved based on a PREssure STaggering Option (PRESTO) scheme, which uses

the discrete continuity balance for a "staggered'' control volume about the face to compute the "staggered'' (i.e., face) pressure. This procedure is similar in spirit to the staggered-grid schemes used with structured meshes. As mentioned previously, the volume fraction equation was discretized with an implicit scheme. The following finite difference scheme is used to calculate fluxes at each cell, for all cells.

$$\frac{a_q^{p+1}-a_q^p}{\Delta t}V+\sum_h(U_h^{p+1}a_{q,h}^{p+1})=0 \quad (3\text{-}15)$$

where $p+1$ is the symbol for the current time step and p is for the previous time step. $a_{q,h}$ is the face value of the q^{th} volume fraction and is computed from the QUICK scheme, V is the volume of the cell, and U_h is the volume flux through the cell h.

An implicit time integration scheme was used in this numerical simulation to evaluate the time level because of the stability condition of the problem. The implicit scheme is solved iteratively at each time-step level. The following equation shows the implicit scheme:

$$\phi^{n+1}=\phi^n+\Delta t\cdot F(\phi^{n+1}) \quad (3\text{-}16)$$

3.4 Boundary Conditions

At the inlet boundary, a higher-order wave theory was used to introduce the wave as a boundary condition. The transient fifth-order Stokes wave was used as a deep-water

wave, with a nonlinear profile. An averaged flow velocity magnitude and wave characteristics such as wave height and wavelength are introduced at the inlet. For more information regarding the fifth-order Stokes wave theory; the reader can refer to [43, 44]. Further, a transient profile for both free surface level and bottom level are introduced based on the origin. For more information, the reader can refer to Fenton (1985 and 1990).

$$\zeta(x,t) = A\cos a + A^2k(b_{22} + A^2k^2b_{24})\cos 2a + A^3k^2(b_{33} + A^2k^2)\cos 3a + A^4k^3b_{44}\cos 4a + A^5k^4b_{55}\cos 5a \quad (3\text{-}17)$$

The velocity potential associated with the wave is calculated as:

$$\phi(x,t) = A(a_{11} + A^2k^2a_{13} + A^4k^4a_{15})\cosh kh \sin a + A^2k(a_{22} + A^2k^2a_{24})\cosh 2kh \sin 2a + A^3k^2(a_{33} + A^2k^2a_{35})\cosh 3kh \sin 3a + A^4k^3(a_{44})\cosh 4kh \sin 4a + A^5k^4(a_{55})\cosh 5kh \sin 5a \quad (3\text{-}18)$$

wherein the above equations, $a_{mn}$and b_{mn} are functions of wave length and liquid heights which can be found in Fenton (1985). A is wave amplitude, k is wave number, which is equal to $2\pi/\lambda$, and $a = k_x x + k_y y - \omega t + \varepsilon$. In this equation, wave frequency ω is equal to $\sqrt{gk\tanh(kh)}$, in which h is the liquid depth.

At the outlet boundary, a damping sink term (S) was added to the momentum equation to avoid wave reflection from the outlet boundary. This damping function, called the numerical beach in the Fluent software, is introduced as:

$$S = -\left[C_1 \rho V + \frac{1}{2} C_2 \rho |V| V\right] \left(1 - \frac{z - z_{fs}}{z_b - z_{fs}}\right) \left(\frac{x - x_s}{x_e - x_s}\right)^2 \quad (3\text{-}19)$$

where $\hat{z}$ is the vertical direction, $\hat{x}$ is the flow direction, and C_1 and C_2 are the linear and quadratic damping resistance coefficients which are set as $10\, s^{-1}$ and $50\, m^{-1}$ respectively. The terms x, x_s, and x_e are the distance in the flow direction, the start, and end points of the damping zone in the $\hat{x}$ direction. The terms z, z_{fs}, and z_b are the distance from the free-surface level, the free-surface level, and bottom level along the $\hat{z}$ direction. V is the velocity along the $\hat{z}$ direction.

The back and front sides of the computational domain are set as symmetrical, which indicates no-slip conditions at these boundaries. The top boundary was set as symmetrical and far enough from the air-water interface to avoid any reflections from this wall. The bottom boundary was set as a wall boundary with the no-slip condition.

3.5 Grid Refinement Study

The computational conditions were set as in the experimental simulation. Several variable sized grids were used to study grid refinement. Three different grid spacing were implemented to study the effect of mesh sizing on the free surface profile and the impact

pressure**.** Grid spacing were varied from 3.5 mm to 5mm near the body to capture the turbulent interface at the moment of impact. The geometry and mesh specifications details are shown in Fig. (3-1).

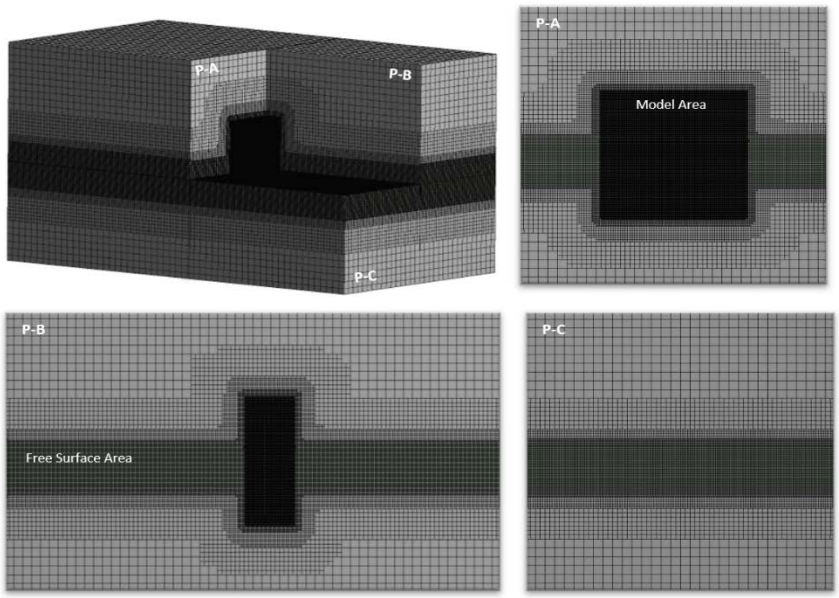

Fig. 3-1 Numerical geometry and structured Cartesian mesh fiction, P-A is a plane section that contains mesh around the model area, P-B is a plane section that includes mesh specifications of both model and free surface area, P-C is a plane section that shows mesh specification showing mesh about the free surface area.

The far-field grid spacing which captures the water-air interface (wave), was set to twice, and in some cases, triple the size of the near-body mesh sizes. Fig. (3-2) shows a comparison of the time series of the pressure at point (B) located on the flat plate model for three different mesh sizes. The impact pressure was computed on the surface, and good general agreement has been found among the smaller grid spacing (3.5 and 4 mm) grids and the experimental results.

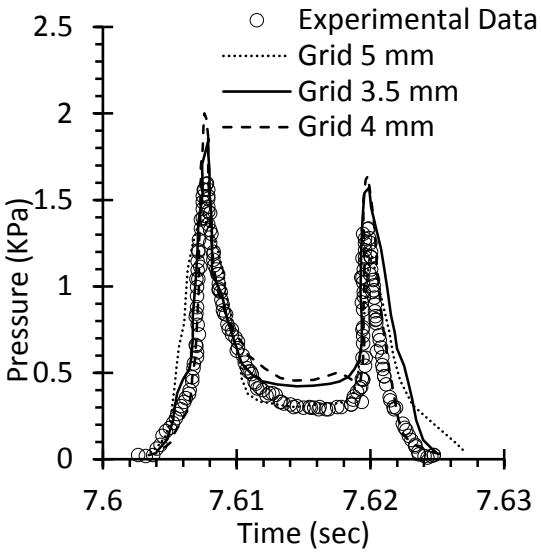

Fig. 3-2 Time variation of pressure from pressure sensor B, located on the model, in comparison with numerical results with three grid sizes.

Further, as is shown in Fig. (3-2), the peak pressure from numerical modeling with the smaller grid size (3.5 and 4 mm) agree well with the experimental simulation, whereas for the coarser grid (5 mm), a delay of the first peak was observed and the peak value is lower than the measured experimental value. Fig. (3-3) shows free surface elevation from the wave probe that is located in front of the model. A coarser grid underpredicts the free surface elevation in comparison with other grid sizes. These two graphs indicate that finer mesh size leads to better results. In the interest of capturing the breakup process, a very small grid size was used near the wall for further processing, but the 4 mm grid would be sufficient for capturing the wave run-up velocity field.

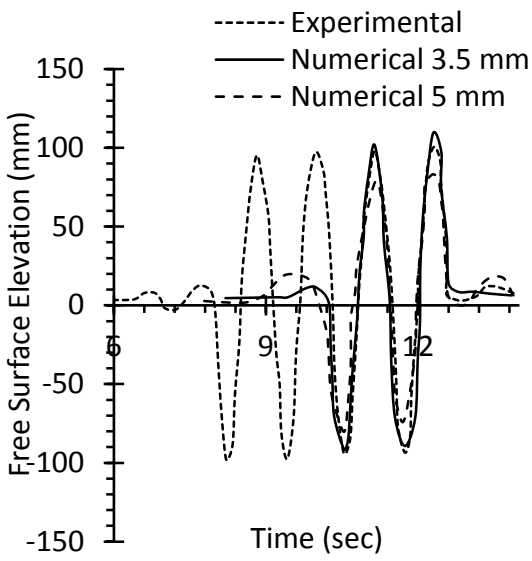

Fig. 3-3 An experimental free surface elevations in comparison with the numerical results for large and small size grid spacing.

This chapter is written based on:

1. Armin Bodaghkhani, Bruce Colbourne, Yuri S. Muzychka, Prediction of Droplet Size and Velocity Distribution for Spray Formation due to Wave-Body Interactions, In Journal of Ocean Engineering, (Under Review).
2. Armin Bodaghkhani, Bruce Colbourne, Yuri S. Muzychka, Droplet Size and Velocity Distribution of Wave Spray due to Wave-Body Interaction, In journal of Flow, Turbulence and Combustion, (Under Review).

Chapter 4 Maximum Entropy Principle (MEP)

This principle was developed by Jaynes (1957) based on the Shannon's (1948) concept of information entropy, which is a measure of the uncertainty in a probability distribution. The MEP is a statistical tool, which is able to predict the least biased probability density function that satisfied a set of constraints expressing the available information related to the distribution in the system. The MEP was originally introduced for predicting the droplet size and velocity distribution of spray from a nozzle applied to diesel spray. However, in this study, the authors applied the one- and two-dimensional MEP to spray production due to wave interaction with marine objects. Similarly, after wave impact, the water forms a liquid sheet, which is the same as a non-homogenous inverted hollow cone that exits from a nozzle with one side of the cone is attached to the marine structure. Afterward, it breaks up into ligaments that form droplets. This new model prediction was compared with the results of droplet and velocity measurements from wave impacts on a lab-scale flat-shaped plate and a bow-shaped model.

4.1 1-D MEP Mathematical Formulations

The process of spray formation from wave impact proceeds by producing a thin sheet of liquid which develops instabilities, breaks up into ligaments, and finally, forms droplets. Size distribution and velocity distribution of droplets are governed by the thermodynamic

laws when equilibrium states are transferred from one state to another. During this transformation, the equations for mass, momentum, and energy conservation are used as constraints, while entropy maximization occurs. Constraints are developed by assuming that the breakup and spray formation is a practically conservative process. The conservation equations downstream of a wave impact area can be presented as probability density function f, which is the probability of finding droplets based on both droplet diameter D or droplet volume V_d, and droplet velocity v_d. In this method, it is assumed that the droplets formed just downstream of the breakup area have the same total, mass, momentum, kinetic energy, and surface energy as the primary water sheet.

The solution of all constraints uses both of these variables, so $d\varphi = d\bar{v}d\overline{D}$. According to the probability concept, the total summation of probabilities is equal to unity $\sum_i \sum_j f_{ij} = 1$. By combining all the conservation constraints with the normalization constraints, information regarding droplet size and velocity distributions based on the conservation laws can be provided (Sellens and Brzustowski, 1985). A normalized set of equations (Li and Tankin, 1987; Li *et al.*, 1991) can be solved iteratively based on the Newton-Raphson procedure to predict a size and velocity distribution of spray cloud.

$$\int_{\bar{D}_{min}}^{\bar{D}_{max}} \int_{\bar{v}_{min}}^{\bar{v}_{max}} f\overline{D}^3 d\bar{v}d\overline{D} = 1 + \bar{S}_m \tag{4-1}$$

$$\int_{\bar{D}_{min}}^{\bar{D}_{max}} \int_{\bar{v}_{min}}^{\bar{v}_{max}} f\overline{D}^3 \bar{v}d\bar{v}d\overline{D} = 1 + \bar{S}_{mu} \tag{4-2}$$

$$\int_{\bar{D}_{min}}^{\bar{D}_{max}} \int_{\bar{v}_{min}}^{\bar{v}_{max}} f(\bar{D}^3 \bar{v}^2/_H + B\bar{D}^2/_H) d\bar{v} d\bar{D} = 1 + \bar{S}_e \quad (4\text{-}3)$$

$$\int_{\bar{D}_{min}}^{\bar{D}_{max}} \int_{\bar{v}_{min}}^{\bar{v}_{max}} f d\bar{v} d\bar{D} = 1 \quad (4\text{-}4)$$

$$f = 3\bar{D}^2 \exp\left[-\lambda_0 - \lambda_1 \bar{D}^3 - \lambda_2 \bar{D}^3 \bar{v} - \lambda_3 \left(\bar{D}^3 \bar{v}^2/_H + B\bar{D}^2/_H\right)\right] \quad (4\text{-}5)$$

Equations (4-1) to (4-3) are mass conservation, momentum equation, and energy equations, respectively. Eq. (4-4) is a normalization constraint and Eq. (4-5) is the probability density function (PDF). In these equations, the solution domain changes from $\bar{D}_{min}$ to $\bar{D}_{max}$ for droplet size variations and $\bar{v}_{min}$ to $\bar{v}_{max}$ for droplet velocity variations, which in this simulation are set as 0 to $1500\ \mu m$ for droplet sizes and 0 to $8\ m/s$ for droplet velocities, respectively. According to the aforementioned references, in this set of equations the dimensionless terms were used as $\bar{D}_i = D_i/D_{30}$, $\bar{v}_j = v_j/U_0$, where U_0 is the average initial velocity of the water sheet at the moment of impact with the wall and D_{30} is the mass mean diameter of droplets and is calculated based on the experimental results using the following equation:

$$D_{30} = \sum m_i d_i /_M = \sum n_i d_i^4 /_{\sum n_i d_i^3} \quad (4\text{-}6)$$

In Eq. (4-5), f is the PDF for representing the continuous size and velocity distribution in an integral form. In Eq. (4-1), the non-dimensional mass source term ($\bar{S}_m$) was neglected because the effect of evaporation and condensation were not considered. The drag force was considered to be acting on the liquid sheet and spray droplets. The drag force on the liquid is calculated as a momentum transformation and is considered as a momentum source. By considering the drag force to be acting on one side of the liquid sheet with the length of L_b (the other side is attached to the model), the drag force (F_1) is written as (White, 2006):

$$F_1 = {}^1\!/_2\, \rho_a {U_0}^2 A_f C_D \tag{4-7}$$

$$\begin{cases} C_D = 1.328/\sqrt{Re_L} & 10^3 < Re_L \\ C_D = (1.328/\sqrt{Re_L}) + 2.3/Re_L & 1 < Re_L < 10^3 \end{cases} \tag{4-8}$$

where C_D is the drag coefficient for flow over a flat plate with a contact area of A_f.

The computational domain was divided into two separate domains: (1) the domain containing the liquid sheet and (2) the domain containing droplets, once droplets form from the ligament breakup. Eq. (4-7) introduced the drag force acting on the water sheet at the first computational domain and the following equation, Eq. (4-9) presented the drag force acting on the droplets at the second computational domain:

$$F_2 = {}^1\!/_2\, C_D \rho_a {V_d}^2 A_d \tag{4-9}$$

$$C_D = \begin{cases} 24/Re & Re \le 0.2 \\ 18.5/Re^{0.6} & 0.2 \le Re \le 500 \\ 0.44 & 500 \le Re \le 10^5 \end{cases} \tag{4-10}$$

where C_D is the droplet drag coefficient, V_d is the droplet velocity - which because of the highly transient nature of the problem, is varied with time - and A_d is assumed to be the area of a spherical droplet with a constant size.

In Eq. (4-2), the non-dimensional momentum source was calculated for the water sheet domain and the droplet domain using the following equations, which represent the amount of momentum transferred from the surrounding air medium to the liquid sheet and to the droplets per unit of time, respectively.

$$\bar{S}_{mu} = \frac{F}{\dot{J}_0} = \frac{F_1}{\rho_l U_0^2 A_{cross}} = \frac{\rho_a}{\rho_l} \times C_D \times \frac{\frac{1}{2}(b+c)L_b}{b \times t} \tag{4-11}$$

$$\bar{S}_{mu} = \frac{F}{\dot{J}_0} = \frac{F_2}{\rho_l U_0^2 A_{cross}} = \frac{1}{2} \times \frac{\rho_a}{\rho_l} \times C_D \times \left(\frac{d_d}{d_{30}}\right) \tag{4-12}$$

where F is the drag force, $\dot{J}_0$ is the initial momentum flow rate, L_b is the breakup length, and t is the breakup thickness. Variables b and c are the initial edge of the impact and the distributed edge of the water sheet, respectively.

In Eq. (4-3), the $\bar{S}_e$ represents all the sources of energy. However, in this simulation, energy conversion was not considered. In Eq. (4-5), $B = 12/We$, $We = \rho U_0^2 D_{30}/\sigma$, and H is the shape factor, which, for the uniform velocity profile, is equal to 1. To solve the set of equations of (4-1 - 4-5), the Lagrange multipliers should be calculated first, which can be obtained by solving the whole set of equations simultaneously. The Newton-Raphson numerical method was used from the initial value guesses for λ_0, λ_1, λ_2, and λ_3, to calculate new values for the Lagrange multipliers. Because of the complexity of this set of equations, another constraint for the Lagrange multipliers is needed to stabilize the system after each iteration, and to ensure that normalization is maintained. This constraint is introduced by Sellens and Brzustowski (1985) as:

$$\lambda_0 = \ln\left[\int_{\bar{D}_{min}}^{\bar{D}_{max}} \int_{\bar{v}_{min}}^{\bar{v}_{max}} \exp[-\lambda_1 \bar{D}^3 - \lambda_2 \bar{D}^3 \bar{v} - \lambda_3 (\bar{D}^3 \bar{v}^2 + B\bar{D}^2)]\, d\bar{v} d\bar{D}\right] \quad (4\text{-}13)$$

According to theory, the velocity distribution for any droplet size is Gaussian, and the droplet velocity in a spray cannot be negative. This leads to a velocity distribution resembling a truncated Gaussian distribution. Number-based droplet size distribution can be extracted from Eq. (4-5) by integration over the velocity range as:

$$\frac{dN}{d\bar{D}} = \frac{3}{2}\left(\frac{\pi \bar{D}}{\lambda_3}\right)^{1/2} \{\mathrm{erf}(A) - \mathrm{erf}(B)\} \exp\left(-\lambda_0 - \lambda_3 B\bar{D}^2 - \left(\lambda_1 - \frac{\lambda_2}{4\lambda_3}\right)\bar{D}^3\right) \quad (4\text{-}14)$$

where N is the normalized droplet numbers and:

$$A = (\bar{v}_{max} + \frac{\lambda_2}{4\lambda_3})(\lambda_3 \bar{D}^3)^{1/2} \quad (4\text{-}15)$$

$$B = (\bar{v}_{min} + \frac{\lambda_2}{4\lambda_3})(\lambda_3 \bar{D}^3)^{1/2} \quad (4\text{-}16)$$

4.2 2-D MEP Mathematical Formulation

Although some models for small-scale atomization suggest a deterministic method to predict the liquid sheet breakup and droplet formation, the final stage of spray formation from the wave impact on a larger scale such as wave impact with the scaled model in tow tank or wave impact with the large-scale model in a real situation is random and chaotic. In this regards, the basics conservation equations such as mass, momentum, and energy equations during the change of state from the wave impact to water sheet and then droplets must be satisfied. The schematic drawing of different stages of this occurrence is shown in Fig. (4-1). For a specific given wave characteristic conditions, there are an infinite set of possible droplet sizes and velocities that can satisfy the conservation equations and also the last spray formation require a statistical description of droplets ensembles.

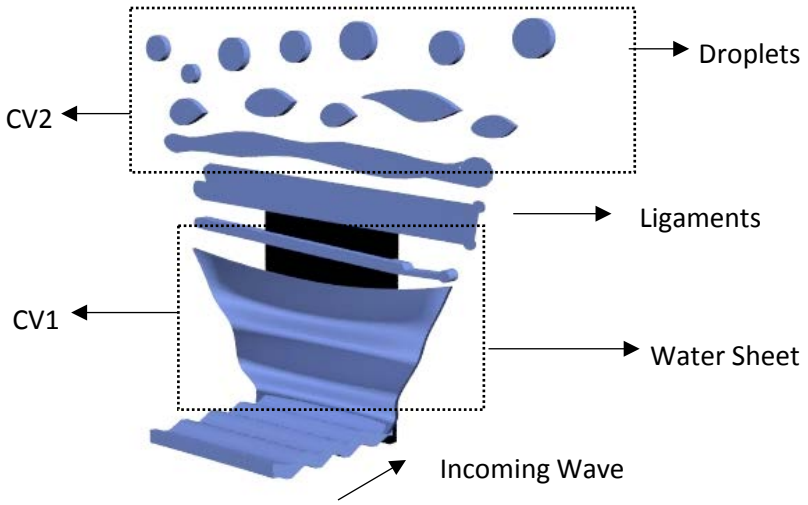

Fig. 4-1 Schematic drawing of water sheet formation and breakup due to wave impact. Two Control Volumes (CV) for calculating the drag force are illustrated in the figure.

In this study, a probability density function (PDF) by maximizing Shannon's entropy (Shannon 1948) according to the MEP was obtained. The PDF for the droplet size and velocity is introduced by Li and Tankin, 1991 as:

$$f = \exp[-\lambda_0 - \lambda_1 \bar{D}^2 - \lambda_2 \bar{D}^3 - \lambda_3 \bar{D}^3 u_* - \lambda_4 \bar{D}^3 v_* - \lambda_5 \bar{D}^3 (u_*^2 + v_*^2)] \quad (4\text{-}17)$$

where λ_i's $(i = 0, 1, 2, 3, 4, 5)$ are the Lagrangian multipliers, which are determined based on the five conservation laws and normalization constraint and are in continuous integral form as:

Mass: $$\int_{\bar{D}_{min}}^{\bar{D}_{max}} \int_{\bar{u}_{min}}^{\bar{u}_{max}} \int_{\bar{v}_{min}}^{\bar{v}_{max}} f \bar{D}^3 \, du_* dv_* d\bar{D} = 1 + \bar{S}_m \quad (4\text{-}18)$$

X-Momentum: $\int_{\bar{D}_{min}}^{\bar{D}_{max}} \int_{\bar{u}_{min}}^{\bar{u}_{max}} \int_{\bar{v}_{min}}^{\bar{v}_{max}} f\bar{D}^3 \bar{u}\, du_* dv_* d\bar{D} = \overline{u_*} + \bar{S}_{mu}$ (4-19)

Y-Momentum: $\int_{\bar{D}_{min}}^{\bar{D}_{max}} \int_{\bar{u}_{min}}^{\bar{u}_{max}} \int_{\bar{v}_{min}}^{\bar{v}_{max}} f\bar{D}^3 \bar{v}\, du_* dv_* d\bar{D} = \overline{v_*} + \bar{S}_{mv}$ (4-20)

Kinetic Energy: $\int_{\bar{D}_{min}}^{\bar{D}_{max}} \int_{\bar{u}_{min}}^{\bar{u}_{max}} \int_{\bar{v}_{min}}^{\bar{v}_{max}} f\bar{D}^3 ({u_*}^2 + {v_*}^2) du_* dv_* d\bar{D} = \overline{u_*^2 + v_*^2} + \bar{S}_{ke}$ (4-21)

Surface Energy: $\int_{\bar{D}_{min}}^{\bar{D}_{max}} \int_{\bar{u}_{min}}^{\bar{u}_{max}} \int_{\bar{v}_{min}}^{\bar{v}_{max}} f\bar{D}^2\, du_* dv_* d\bar{D} = \frac{1}{3\tau_*} + \bar{S}_s$ (4-22)

Normalization: $\int_{\bar{D}_{min}}^{\bar{D}_{max}} \int_{\bar{u}_{min}}^{\bar{u}_{max}} \int_{\bar{v}_{min}}^{\bar{v}_{max}} f\, du_* dv_* d\bar{D} = 1$ (4-23)

As is emphasized the solution space consist of three variables as $d\psi = d\bar{u}d\bar{v}d\bar{D}$, where $\bar{D} = d/D_{30}, \bar{u} = u/U,\ \bar{v} = v/U$. In these equations, the Lagrangian multipliers must be determined numerically for each individual case. In addition to the above conservation equations, by adding another constraint of the surface area to volume ratio of the droplets, the effect of the distribution of small droplets will be considered in PDF values. The following equation suggests the mean surface to volume ratio constraint for a given spray.

$\int_{\bar{D}_{min}}^{\bar{D}_{max}} \int_{\bar{u}_{min}}^{\bar{u}_{max}} \int_{\bar{v}_{min}}^{\bar{v}_{max}} f\bar{D}^{-1}\, du_* dv_* d\bar{D} = K_p$ (4-24)

By considering this new constraint the probability distribution function converted to the following equation:

$$f = \exp[-\lambda_0 - \lambda_1 \overline{D}^2 - \lambda_2 \overline{D}^3 - \lambda_3 \overline{D}^3 u_* - \lambda_4 \overline{D}^3 v_* - \lambda_5 \overline{D}^3 (u_*^2 + v_*^2) - \lambda_6 \overline{D}^{-1}] \quad (4\text{-}25)$$

4.2.1 Source Terms in Breakup

Previously mentioned conservation equations are contained a source term to indicate a deviation of this constraint from an entirely conservative breakup. These conditions are typically minimal, but their effects are significant in the final result of breakup process.

The mass source term $\bar{S}_m$ reflect any changes to the amount of mass during the breakup process such as evaporation and condensation. As the duration of breakup are usually around $3 - 5\ (s)$, which is very short, typically the effect of evaporation is neglected and the mass source term assumed to be zero. The momentum source terms indicate the acceleration of the liquid during the breakup process. The drag force on the liquid is calculated as a momentum transformation and is considered momentum source term. The following equations (4-26 – 4-30) represent the calculation of these source terms for the both sides of the liquid sheet. The kinetic energy source term $\bar{S}_{ke}$ represent the amount of kinetic energy transferred between the liquid sheet and the surrounding air, which is considered zero in this calculation.

$$F_1 = {}^1/_2\, \rho_a {U_0}^2 A_f C_{D,y} \quad (4\text{-}26)$$

$$F_2 = {}^1\!/_2\, \rho_a V_0{}^2 A_f C_{D,x} \tag{4-27}$$

$$C_{Dx,y} = \begin{cases} 1.328/\sqrt{Re_L} & 10^3 < Re_L \\ (1.328/\sqrt{Re_L}) + 2.3/Re_L & 1 < Re_L < 10^3 \end{cases} \tag{4-28}$$

$$\bar{S}_{mu} = \frac{F}{j_0} = \frac{F_1}{\rho_l U_0^2 A_{cross}} = \frac{\rho_a}{\rho_l} \times C_{D,y} \times \left[\frac{1}{2} \cdot \frac{(b+c)L_b}{(b \times t)}\right] \tag{4-29}$$

$$\bar{S}_{mv} = \frac{F}{j_0} = \frac{F_2}{\rho_l V_0^2 A_{cross}} = \frac{\rho_a}{\rho_l} \times C_{D,x} \times \left[\frac{1}{2} \cdot \frac{(b+c)L_b}{(b \times t)}\right] \tag{4-30}$$

where L_b in Eqs. (4-29) and (4-30) represent the liquid sheet breakup length and can be calculated based on the nonlinear stability analysis. According to Jazayeri and Li, 1997 the breakup length is obtained by taking into account the solution of the initial disturbance amplitude up to third order. This correlation (Eq. 4-31) represent the breakup length based on the Weber number (We), density (ρ), and initial disturbance amplitude (η):

$$\frac{L_b}{h} = \sum_{i=1}^{5} \sum_{j=1}^{4} \sum_{k=1}^{4} \frac{c_{ij}}{We^{i=1}} \left[\ln\left(\frac{h}{\eta}\right)\right]^{j-1} \left(\frac{B_k}{\rho^{k-1}}\right) \tag{4-31}$$

where $2h$ is sheet thickness, and the coefficients c_{ij} and B_k are determined by the least-square fitting technique.

The surface source term accounts for changes in surface energy during a breakup when the liquid sheet breakup, its surface area is reduced by two processes of contraction of sheet segments into ligaments and then the breakup of ligaments to droplets. A model for this energy reduction is provided by Dombrowski and Johns (1963). Further, Sellens (1989) consider the surface source term as the values of D_{30}/D_{32}, where D_{30} is the Mass mean diameter and D_{32} is the Sauter mean diameter. In this study, the value of D_{30} can be calculated by Eq. (4-32) and the value of D_{32} is deliberated based on the results of experimental study.

$$D_{30} = \sum \frac{m_i d_i}{M} = \frac{\sum n_i d_i^4}{\sum n_i d_i^3} \tag{4-32}$$

$$D_{32} = \frac{\sum n_i d_i^3}{\sum n_i d_i^2} \tag{4-33}$$

4.2.2 Mass Mean Diameter

The mass mean diameter is calculated based on the nonlinear stability analysis (Jazayeri and Li 1997). This study shows that the liquid sheet breaks off at half-wavelength intervals to form ligaments and ligaments further break down into individual droplets according to Rayleigh theory (Rayleigh 1879). According to the equation of conservation of mass, the nonlinear stability analysis, and the Rayleigh theory the expression for mass mean diameter can be calculated from the following equation:

$$D_{30} = 2.12\ (\lambda_1 h)^{1/2} \tag{4-34}$$

where λ_1 can be calculated from $d\Omega_r/dm = 0$, where Ω_r represent the real part of the dispersion relation governing the characteristics of the unstable sinuous waves on an incompressible viscous liquid sheet as is based on the linear stability theory (Squire 1953, Li and Tankin 1991) and is given by:

$$\left[(\Omega + im) + \frac{2m^2}{R}\right]^2 \tanh(m) - \frac{4m^3}{R^2}\, S \tanh(S) + \rho\Omega^2 + \frac{m^3}{We_1} = 0 \tag{4-35}$$

where R is the radius of curvature of interface, $m = ka$ is the dimensionless wavenumber, $2a$ is sheet thickness, $k = 2\pi/\lambda$ is the wavenumber, and λ is the wavelength of disturbance ω. In Eq. (4-35), $S = sa$ and $s = k^2 + \omega + \frac{ikU_0}{\upsilon_t}$, where υ_t is kinematic viscosity.

This chapter is written based on:

1. Armin Bodaghkhani, Yuri S. Muzychka, Bruce Colbourne, A scaling model for droplet characteristics in a spray cloud arising from wave interactions with marine objects, ASME, International Conference on Offshore Mechanics and Arctic Engineering, Volume 7A: Ocean Engineering ():V07AT06A050.
2. Armin Bodaghkhani, Yuri S. Muzychka, Bruce Colbourne, An analytical model of final average droplet size prediction of wave spray cloud, International Journal of Heat and Fluid Flow, (Under Review).

Chapter 5 Analytical Approach

In this chapter, four stages of wave spray production are considered, including; 1) the formulation of wave impact velocities based on the input wave characteristics, 2) the formulation of air entrapment at the moment of impact based on the Bagnold-Mitsuyasu scaling law, which calculates the maximum impact pressure, 3) a mathematical relationship between the maximum wave impact pressure and the maximum wave run-up velocities, and finally, 4) the breakup phenomena, all are combined to predict a relationship between input wave characteristics and the wave spray final average droplet diameters. All the stages that are considered in this procedure are schematically shown in Fig. (5-1).

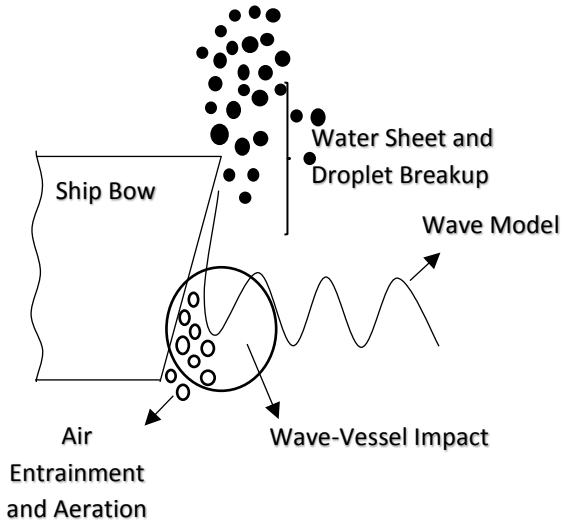

Fig. 5-1 Schematic of wave spray formation and four stages from the wave impact on final spray formation.

5.1 Wave Velocity at Impact

Wave characteristics at the moment of impact play a significant role in the final average droplet diameter in the spray cloud. In this study, two wave models were considered to calculate the vertical and horizontal water wave velocity at the moment of impact. The effect of both models for calculating the wave velocity on the final average droplet diameter is investigated.

First, the velocity of the wave at the moment of impact is calculated using the equation for harmonic waves in deep water, with the horizontal and vertical water velocity moving along the x-axis and with time t as:

$$u = k\xi_a V_w \cos k(x - V_w t) \tag{5-1}$$

$$w = k\xi_a V_w \sin k(x - V_w t) \tag{5-2}$$

where k is the wavenumber calculated as $k = 2\pi/L_w = 4\pi^2/(gT_w^2)$, ξ_a is the wave amplitude, and V_w is the wave velocity calculated as $V_w = \sqrt{gL_w/(2\pi)}$ for deep water. In these equations, L_w is the wavelength calculated as $L_w = gT_w^2/(2\pi)$ and T_w is the wave period calculated as $T_w = \sqrt{2\pi L_w/g}$ (Bhattacharyya, 1978). It should be noted that, for the sake of simplicity, the wave diffraction and radiation effects are not considered in this study. However these two phenomena do influence the velocity of the wave at the impact moment.

Secondly, a second order Stokes wave theory was considered to calculate the velocity field component for finite depth water wave. From the velocity potential equations, and based on the Fourier expansion, the horizontal and vertical water velocity moving along the x-axis is calculated by the following equations (Stokes 1880, Fenton 1990):

$$u = \sum_{n=1}^{\infty} n\Psi_n \frac{\cosh n(y+d)}{\sinh nd} \cos nx \tag{5-3}$$

$$v = \sum_{n=1}^{\infty} n\Psi_n \frac{\sinh n(y+d)}{\sinh nd} \sin nx \tag{5-4}$$

where $\Psi(x, y, t)$ is a velocity potential that satisfies the Laplace's equation, then Ψ_n depends on wave amplitude (ξ_a) and water depth, and d is the constant water depth of the undisturbed medium. By expanding the series to the second order, the velocity field components can be calculated as follows:

$$u = \xi_a(\coth d + \xi_a \cos x)\cos x + \frac{3}{4}\xi_a(\coth^2 d - 1)\cdot(\coth^2 d + 1) \tag{5-5}$$

$$v = \xi_a(1 + \xi_a \coth d \cos x)\sin x + \frac{3}{2}\xi_a \coth d \sin 2x\,(\coth^2 d - 1) \tag{5-6}$$

where the wave celerity can be calculated as $c^2 = \frac{g}{k}\tanh(kd)$.

5.2 Maximum Impact Pressure

Wave impact pressure plays a significant role in the process of wave spray formation as it compresses the air that is trapped and leads to acceleration of the wave run-up after the impact. Several authors demonstrated that the Bagnold-Mitsuyasu law can be generalized to cover the wide range of wave impact applications such as 2-D, 3-D, and compression of air during the wave impact (Bredmose *et al.*, 2009; Abrahamsen and Faltinsen, 2013; Bredmose *et al.*, 2015). In the study related to a generalization of Bagnold's law for air compression during wave impact, an assumption was made to consider that all the kinetic energy during the wave impact goes into the compression of an air pocket at the moment of impact. This assumption is not very realistic and is simplified in the present case to consider that during the wave impact some fraction of the kinetic energy is used to accelerate the fluid away from the impact zone. By considering the equation for the kinetic energy of the wave with a liquid region of volume V^* that encloses the air pocket with a volume of V_0 and assuming that the procedure of air compression follows the adiabatic compression law, the work needed to compress the air to maximum pressure of p_{max} can be calculated by the Eq. (5-7) as:

$$\left(\frac{p_{max}}{p_0}\right)^{\frac{\gamma-1}{\gamma}} + (\gamma - 1)\left(\frac{p_{max}}{p_0}\right)^{\frac{-1}{\gamma}} - \gamma = -\frac{\rho_w(\gamma-1)}{2V_0P_0}\int_{V^*} u.u\mathrm{d}V \tag{5-7}$$

where p_0 is the atmospheric pressure, ρ_w is the density of unaerated water, V_0 is the volume of the air pocket at atmospheric pressure, $\gamma = 1.4$ is the heat capacity ratio of air,

and u is the velocity magnitude at the moment of impact. At the moment of impact, the shape of the air pocket volume and the water that enclose this air is arbitrary; however, for the sake of simplicity and by referring to experimental results of wave impact (Bogaert *et al.*, 2010), these shapes are assumed as a half of concentric cylinders with a length equal to the width of impact W. The characteristics linear dimensions of the air pocket and the effective enclosing water, without considering the air leakage are assumed as $D = H_{m0}\pi/12$ and $k_w = 0.2H_{m0}(1 - \pi/12)$, respectively. In these equations, H_{m0} is the significant wave height. By substituting the volumes of the air pocket and the enclosing water based on these diameters and their shapes as well as both wave velocities field in Eq. (5-7), the following equations can be used to calculate the maximum pressure of impact by knowing the input wave characteristics:

$$\left(\frac{p_{max}}{p_0}\right)^{\frac{\gamma-1}{\gamma}} + (\gamma - 1)\left(\frac{p_{max}}{p_0}\right)^{\frac{-1}{\gamma}} - \gamma = -\frac{\rho_w(\gamma-1)}{2P_0}\left(\frac{k_w^2}{D^2} - 1\right)(k\xi_a V_w)^2 \quad (5\text{-}8)$$

$$\left(\frac{p_{max}}{p_0}\right)^{\frac{\gamma-1}{\gamma}} + (\gamma - 1)\left(\frac{p_{max}}{p_0}\right)^{\frac{-1}{\gamma}} - \gamma = -\frac{5}{2}\cdot\frac{\rho_w(\gamma-1)}{P_0}\cdot c' \quad (5\text{-}9)$$

where the ratio of k_w^2/D^2 based on their equations can be calculated as 0.31. c' in Eq. (5-9) is the result of $\int_{V^*} u.u\mathrm{d}V$ and is calculated based on the assumptions that water depth d and wave amplitude ξ_a are constant over the range of the integral. Due to the complicated trigonometry equations, the results of the integral are shown only as c'.

5.3 Maximum Wave Run-up Velocity

The dynamic pressure from a wave impacting with objects has been shown to vary in different locations as well as different cycles. The maximum impact pressure mainly depends on the shape and velocity of the approaching wave. Finding a relation between the flow momentums arising from the wave impact with the corresponding kinematics of the wave is logical to connect these two processes. Referring to the work of Ariyarathne *et al*. (2012) and Song *et al*. (2013), a correlation between the maximum impact pressure and wave phase velocity can be suggested as Eq. (5-10):

$$p_{max} = c_i \rho_w U_{max}^2 \tag{5-10}$$

where c_i is the impact coefficient and U_{max} is the maximum wave run-up velocity, which for practical application can be obtained easily. The value of c_i can be varied based on wave impact geometry, location, and velocity; however an average value is used for this study. Furthermore, a sensitivity analysis regarding the effect of variation of impact coefficient on the comprehensive model will be discussed.

5.4 Breakup Model

The last stage in this study is the correlation that connects the maximum wave run-up velocity with the breakup models, which leads to the calculation of the final average droplet diameter. Under certain conditions, aerodynamic forces exceed the interfacial

tension forces and lead to the formation of unstable waves and this is one of the significant factors leading to the instability and disintegration of a liquid sheet.

Models for the thinning liquid sheet with the velocity included can be found in several studies. However, in this study, the Dombrowski and Johns (1963) model is used, which is based on inter-relating the forces that act on the liquid sheet, which is thinning with time and moving in one direction, in a surrounding gas or air medium. The four forces that are considered in this model are pressure force F_p, surface tension force F_σ, inertial force F_I, and viscous force F_μ. Then, a sinusoidal disturbance is imposed to the system and it is assumed that the sheet thickness varies according to $h\tau = k$, where h is the sheet thickness and τ is the break-up time. The corresponding ligament diameter D_L and final average droplet diameter D_D are calculated as:

$$D_L = 0.9614 \left[\frac{K^2\sigma^2}{\rho_a \rho_w U_{max}^4}\right]^{1/6} \left[1 + 2.6\mu \sqrt[3]{\left(\frac{K\rho_a^4 U_{max}^7}{72\rho_w^2\sigma^5}\right)}\right]^{1/5} \tag{5-11}$$

$$D_D = \left[\frac{3\pi}{\sqrt{2}}\right]^{1/3} D_L \left[1 + \frac{3\mu}{(\rho_w \sigma D_L)^{1/2}}\right]^{1/6} \tag{5-12}$$

where K is the spray parameter and can be calculated for the case of wave impact as $K = C\tau_n W$, τ_n is the sheet thickness at the moment of impact, W is the width of wave impact, and C is varying for this application between 1×10^{-6} and 25×10^{-5}. In Eq. (5-11), σ is the water surface tension, μ is the kinematic viscosity of water, and ρ_a is the air density.

Chapter 6 Results and Discussion

This chapter provides detailed results and discussion from the methods of simulations that are presented in the preceding chapters. The work detailed in the previous chapters is presented as individual studies that were performed to increase the knowledge of wave spray phenomena as a series of processes that starts with the wave impact and ends with the spray cloud. The end objective is to quantify the important aspects of spray cloud droplet characteristics arising from the wave impact with vessels and offshore structures.

6.1 Experimental Results

The process of spray-cloud production and flow kinematics arising from breaking wave impact on a fixed flat-shaped plate and a bow-shaped plate models were investigated using the BIV and DPIV methods to measure the wave run-up velocity. Two perpendicular plane views were used to capture the footages: a side and a front view. The wave run-up velocity measurements at the moment of impact are compared with the results of several published experimental results.

Aside from the BIV method, spray characteristics were examined based on the Digital Particle Image Velocimetry (DPIV) method. Measurements of droplet size, and velocity, as well as wave run-up velocity, were major concerns in this study. Results of velocimetry from both views were compared, and a satisfactory agreement was achieved among more than 90% of the data. The highly transient process of spray formation from the liquid sheet breakup was discussed, and the drag coefficients and drag forces were calculated

in two different stages of spray formation. Several pressure sensors were used to measure the impact pressure and three capacitive wave probes to measure the free surface profile.

6.1.1 Flow Behaviors

Wave interaction with a structure generates a highly turbulent and aerated flow. When the wave that impacts a structure has enough turbulent kinetic energy, it can produce a highly turbulent and aerated region in front of the structure, which leads to the production of a significant amount of spray. Three types of flow after impact were observed in front of the structure in this experiment. Depending on the wave impact condition, these can be categorized as a production of either water sheet, droplets, or both together.

For the first group, waves break and overturn at the moment of impact and transfer all the wave kinetic energy to turbulent kinetic energy (flip-through impact). This happened in conditions where wave velocity was high, which leads to the production of the water sheet, and the water sheet has enough energy to break up and produce droplets. Depending also on the wave characteristics, this type of impact often creates a large height water sheet. Droplets in this kind of impact can reach three times the height of the model (about $3\ \mathrm{m}$). This indicates very high-velocity droplets are formed, and they sometimes reach velocities an order of magnitude greater than the wave impact velocity. Both processes of initial droplet breakup, and in a few observations, secondary droplet breakup, are observed. Fig. (6-1) shows the four time-steps of a wave impact (first wave

condition in Table 2.1) containing both water sheet and droplets and demonstrates the process of spray formation from the sheet breakup. In these figures the tip of the model is located at $Y = 800\ mm$, which is located exactly on the x-axis of these figures. Y is the height in front of the models with respect to origin.

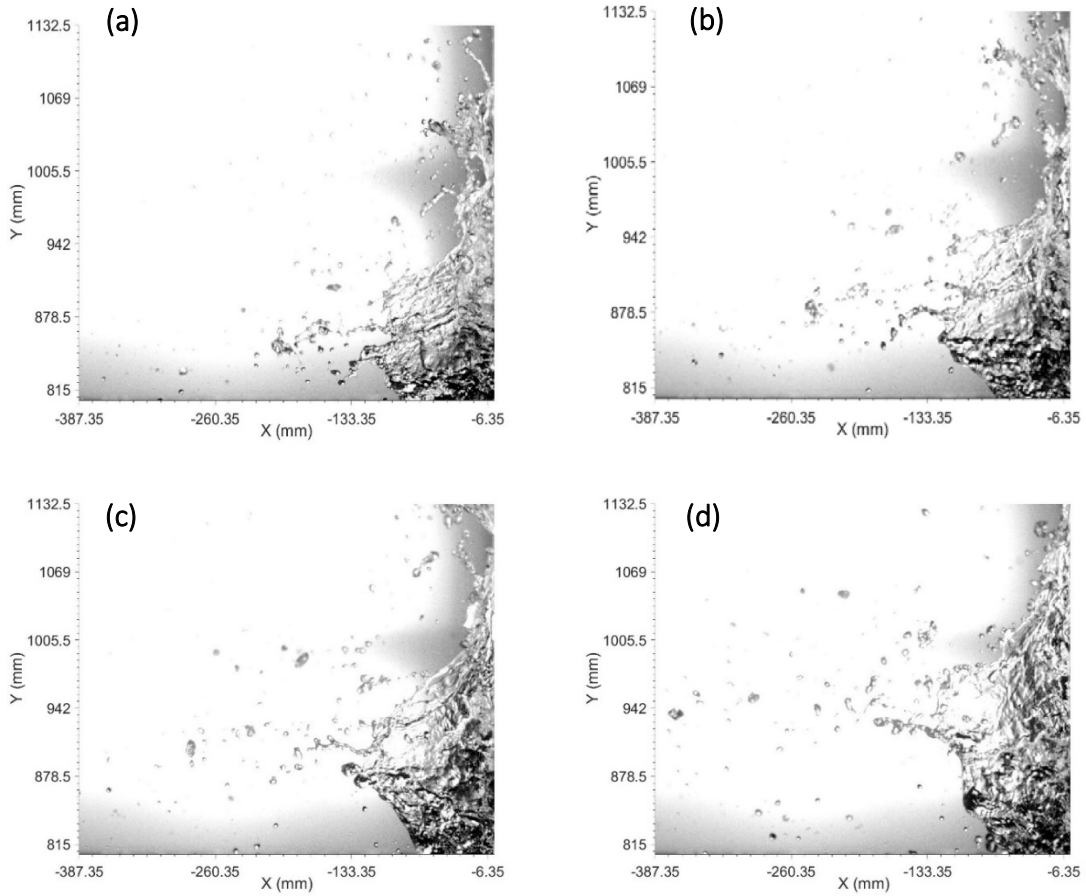

Fig. 6-1 Moment of wave impacts with the flat-plate model. Wave after impact turns into both water sheet and spray. $(a)\ t = 0.10\ s, (b)\ t = 0.15\ s, (c)\ t = 0.20\ s, (d)\ t = 0.25\ s$. Note: $t = 0$ is the moment of wave crest impact with an object.

In the second type of wave impact, which happened in most of the trials, the wave does not have enough kinetic energy (enough velocity) or does not reach the moment of

breaking before hitting the object. These swell waves (sloshing) lead to the production of a low kinetic energy water sheet. This sheet does not have enough velocity to break up and produce droplets and produces a shallow height water sheet in front of the model, which in most cases, does not reach as high as the tip of the model. Fig. (6-2) shows one experimental trial (first wave condition in Table 2.1) for 4 time-steps of this type of impact.

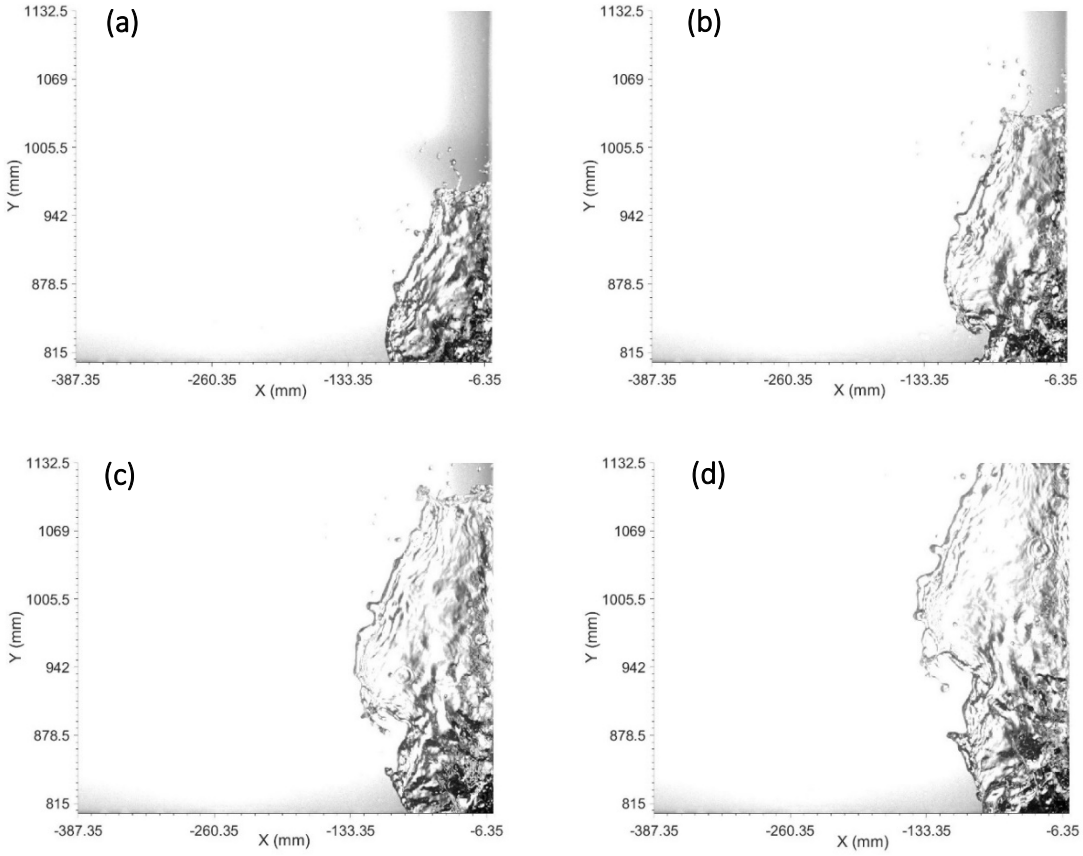

Fig. 6-2 Moment of wave impact with the flat-plate model. Water sheet does not break up due to low energy. $(a)\ t\ =\ 0.10\ s, (b)\ t\ =\ 0.15\ s, (c)\ t\ =\ 0.20\ s, (d)\ t\ =\ 0.25\ s$. Note: $t = 0$ is the moment of wave crest impact with an object.

In the third category of wave impact, droplet production, happened in a few of the trials; all the kinetic energy of the wave was transferred to the water and produced a large

volume of droplets at the moment of impact. This was observed when wave impact happened exactly at the time in which the wave crest started to overturn. This condition produced a high impact pressure on the structure, and because the volume of water that turned to spray is high, which led to large measurement errors associated with droplets overtopping, further measurements and image processing were not performed on this type of impact.

Although it is common to categorize the wave impact based on the wave slope at the moment of impact, several researchers categorized the impact waves as high and low aeration (Bullock *et al.,* 2007; Bredmose *et al.,* 2009). In the current study, waves that are categorized as swell type (sloshing) are considered as low aeration, which leads to high spike pressure with short duration. This type of impact is not violent, and no air entrapment occurs as the wave crest is not overturned and nor is ultimately overturned before the impact. The other two types (flip-through and breaking point impact) can be classified as high aeration waves, which contain significant amounts of trapped air in the process of impact. Both of these two waves produce a high spike pressure with a long duration on pressure sensors. Further, the breaking point impact is violent, and spray production is rapid, which is the feature that separates the breaking point impact from the flip-through in this study. However, both have a large amount of air trapped in them during the impact.

Spray production in conditions where the waves crest is before the time of overturning (mostly known as swell waves or sloshing) and in situations where the wave is at the time

of overturning is not studied. Two critical conditions in which wave impacts produce high-velocity water sheets and droplets are identified as: first, the wave impact when the wave crest is exactly at the moment of overturning, and second: the wave impact when the wave is completely overturned. As shown in the previous Figures (6-1) and (6-2), the time that the spray or sheet reaches its maximum height is different in each impact type. Waves that have higher kinetic energy and produce a spray from the beginning of impact provide the fastest event. An impact type where only a water sheet was produced is the slowest type, and the duration of the event cycle is longer than the other impact types.

The observed range of wave shapes at the moment of the impact showed repeatable and consistent outcomes. More than 90% of waves with the same characteristics produce the same type of splashes and almost the same range of droplet size and velocities after the impact. The consistency between these observations of water behaviors after the impact makes the study of spray-cloud formation easier.

6.1.2 Velocity Measurements

The BIV technique was used to quantify flow from the qualitative results captured by the high-speed camera. The velocity and size distribution of droplets from both the side and front FOV were compared to each other, and a good agreement between these two sets of data was achieved. In this method, the backgrounds of the images for different impact conditions were subtracted from the actual image. Next, the size of the droplets in the binary images was estimated using the LABVIEW image acquisition toolbox as well

as a Matlab image processing algorithm. The results from both tools were compared, and a satisfactory agreement was achieved with a maximum disagreement of 5%. Only droplets are taken into account, and the presence of any possible water sheet that does not break up to droplets was neglected in the calculation. In addition, velocimetry measurements were performed using the Insight 3G PIV software, and the velocity fields were calculated using an adaptive multi-pass algorithm. The initial interrogation window size of 32×32 pixels and a final window size of 16×16 pixels were used. A median filter was applied to eliminate the false vectors in the velocity field. Because of interest in an instantaneous velocity for each class size of droplets, the velocity fields were not reported here. Manual droplet velocimetry measurements, based on tracking individual droplets, were performed based on the in-house Matlab algorithm and are compared with the PIV measurements. This shows very good agreement with a relative error about 2%.

Figures (6-1) and (6-2) demonstrate the results of spray cloud velocity and size measurements for several waves from the side and front views in the flat-shaped plate and bow-shaped plate model, respectively. Each droplet velocity point that is presented in these figures is calculated based on the averaging of 10 droplets maximum velocity (20 frames – each 1.2 ms). Due to the transient behavior of droplets, two stages of droplet motion were considered as areas for measuring the velocities: the point of detaching from the sheet and the distance halfway from reaching the maximum height. Droplet size was placed into three categories: small, with a diameter of $300-700$ μm; medium, with a diameter of $700-1100$ μm; and large, with a diameter of $1100-1500$ μm. These groups

were categorized between the minimum and maximum droplet sizes that were observed and measured in the experiment.

Dimensional analysis was performed to introduce the governing and affecting variables in this experiment, which are:

$$\mathrm{V_d} = \mathrm{f}(\mathrm{d_d}, \mathrm{T}, \mathrm{d_m}, \mathrm{V_c}, \mathrm{g}, \mathrm{h_w}, \rho, \sigma) \tag{6-1}$$

where $\mathrm{V_d}$ is the droplet velocity and is dependent on both position and time, $\mathrm{d_d}$ is the droplet diameter, $\mathrm{d_m} = 600\ \mu\mathrm{m}$ is the roughly average droplet diameter, $\mathrm{V_c}$ is the wave phase velocity, g is gravitational acceleration, T is the wave period, $\mathrm{h_w}$ is the wave height at the moment of impact, ρ is the water densiy and σ is the water surface tension. Both water properties considered constant in this experiment. Performing the dimensionless analysis leads to the following dimensionless parameters:

$$\frac{\mathrm{V_d}}{\mathrm{V_c}} = \mathrm{G}\left(\frac{V_c T}{d_d}, \frac{d_d}{d_m}, \frac{g d_d}{V_c^2}, \frac{\mathrm{h_w}}{d_d}, \frac{\sigma}{V_c^2 d_d \rho}\right) \tag{6-2}$$

Since water droplet positions and maximum heights were not measured precisely in this experiment, the parameters related to their positions were neglected. Likewise, the time associated with droplet positions was disregarded in the dimensional analysis. Figures (6-1) and (6-2) illustrate similar profiles for two nondimensional parameters ($\mathrm{V_d}/\mathrm{V_c}$ and $\mathrm{d_d}/\mathrm{d_m}$) for different wave phase velocities. Based on the curve fitting

technique, different equations for the data trends are calculated. A linear relationship between dimensionless droplet size and velocity was observed. By adding the inverse effect of wave phase velocity to these relationships, the following empirical relationship is derived:

$$\frac{\mathrm{V_d}}{\mathrm{V_c}} = -\mathrm{a}\left(\frac{\mathrm{d_d}}{\mathrm{d_m}}\right) + \mathrm{b} \tag{6-3}$$

where the values of a and b are different for both models: a and b were calculated for the flat-shaped plate model as -0.4 and 2.4, and -0.5 and 2.3 for the bow-shaped model.

Results generally show that small droplets have a higher average velocity, and large droplets have a lower range of velocities. Medium size droplets, in all cases, have velocity ranges between two other groups and only this group reaches maximum height in the FOV1 area. Due to resistance forces of drag and gravity on the droplets, the small and large droplets cannot enter the higher spray-cloud area (FOV1). As Figures (6-3) and (6-4) show, in most cases, waves with higher wave phase velocities produce a finer spray with larger droplet velocities when it impacts the wall. Waves with the phase velocity of $V_c = 1.6\ \mathrm{m/s}$, which in this experiment are the waves with larger wave heights and wavelengths, produce finer droplets and larger droplet velocities $(5.5 - 7\ \mathrm{m/s})$ with a maximum of $4.40\mathrm{V_c}\ (\mathrm{m/s})$.

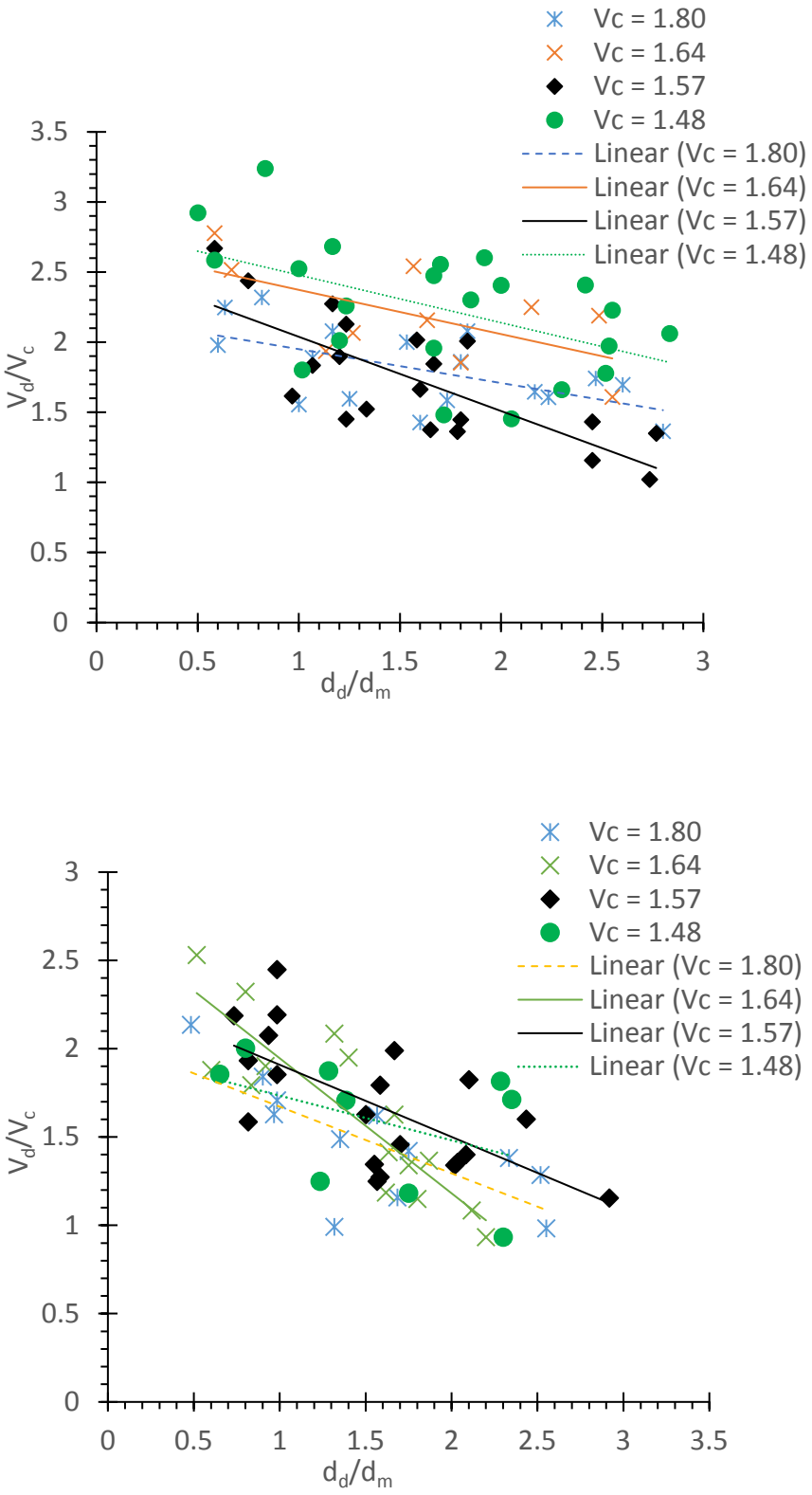

Fig. 6-3 Droplet average velocity for various droplet sizes in different wave phase velocities (V_c) for the flat-shaped plate model. Top: Front view, bottom: Side view.

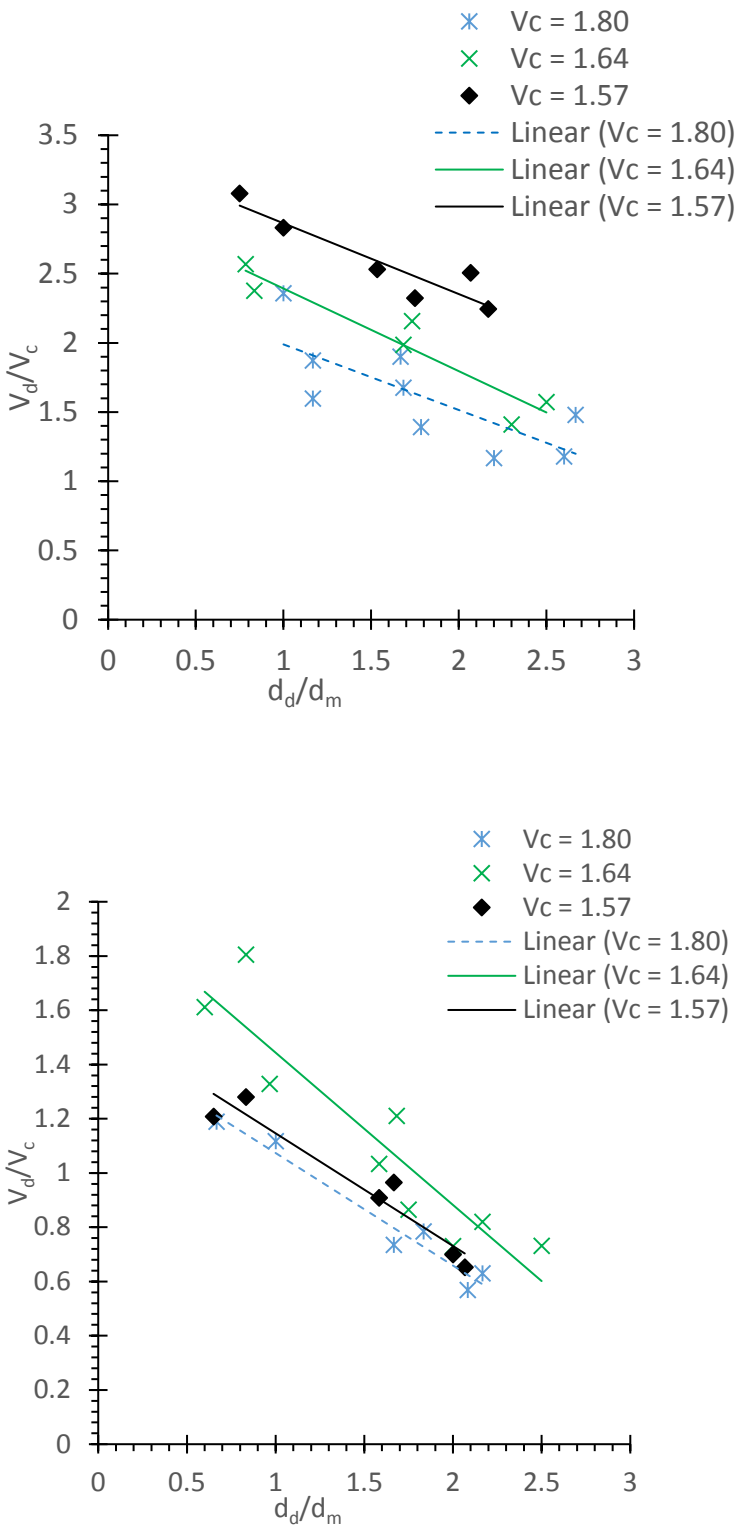

Fig. 6-4 Droplet average velocity for various droplet sizes in different wave phase velocities (V_c) for the bow-shaped model. Top: Front view, bottom: Side view.

The results of the image processing technique for the jet produced immediately after impact were compared with those reported by Chuang *et al*. (2015) and Ryu *et al*. (2007a). The dominant velocity of the run-up is reported by Chuang *et al*. as $2.8\,\mathrm{C}$, in which C represents a wave phase velocity equal to $2.05\ \mathrm{m/s}$. This value matches the current experimental data in which the maximum velocity of droplets was measured at about $5.5-7\ \mathrm{m/s}$, except for those impacts that involved wave crests at the time of overturning. These values are well matched with the data reported by Ryu *et al*. (2007a). In the cases of wave impact with a structure at the moment of overturning, the maximum velocity was measured at around $8\ \mathrm{m/s}$.

6.1.3 Droplet Behavior Examination

Prediction of the motion of spray droplets is a time-dependent problem and cannot be considered as a steady state flow. As the experiment results show, spherical droplets experience significant acceleration and deformation during transfer from the moment of impact until reaching their maximum height. Drag force has a significant influence on deformation, which affects the motion of droplets. In the case of a wave impact on a stationary plate, the increase in drag force due to droplet deformation leads to a reduction in droplet velocity, which in turn decreases the drag force. For larger droplets, the gravitational force is significant and reduces droplet speed. Spray production in this experiment is considered an isolated drop configuration, in which the spray is not dense, and droplets do not affect each other.

The Reynolds number range was calculated from the range of droplet sizes and velocities to be between $900 < \mathrm{Re_d} < 10^4$. The Reynolds number is defined as $\mathrm{Re_d} = \mathrm{V_d d_d}/\upsilon$, where $\mathrm{V_d}$ is droplet velocity, $\mathrm{d_d}$ is droplet diameter, and υ is the kinematic viscosity of water. By considering the area of interest where the spray cloud is formed (FOV2 in Fig. 2-1a), only droplets with a particular velocity and size can be present and reach this area. This is because of the kinetic energy of droplets, and only some droplets have enough kinetic energy to reach this level. Overall, high and low-velocity droplets do not follow the stream to the FOV2 region and fall down to the water.

The following relationship (Eq. 6-4) is used to calculate the drag coefficient for the range of Reynolds numbers that droplets experience and is introduced by Kelbaliyev and Ceylan (2007). This relationship fits the drag curve nicely for a broad range of Reynolds numbers smaller than $\mathrm{Re} = 5 \times 10^5$, which is referred to as the drag crisis. The smallest and largest Reynolds numbers were calculated between 900 and 10^4 for this experiment.

$$\mathrm{C_D} = \frac{24}{\mathrm{Re}_d}\left[1 + 18.5\mathrm{Re_d^{3.6}} + \left(\frac{\mathrm{Re_d}}{2}\right)^{11}\right]^{\frac{1}{30}} + \frac{4}{9}\frac{\mathrm{Re_d^{\frac{4}{5}}}}{330+Re_d^{\frac{4}{5}}} \tag{6-4}$$

The drag coefficient for several droplet velocities and sizes are shown in Fig. (6-5) for both the flat-shaped plate model and the bow-shaped model. The results are based on measured data from the front view. As both figures show, the variation of drag coefficients for smaller droplets is much higher than for the other size classes. Drag

coefficients for medium droplets are nearly constant; this demonstrates that drag force and gravitational force do not play a significant role in changing the velocities of the mid-sized droplets. Generally, the drag coefficient is equal to $4/9$, which changes very little for Reynolds numbers between 2×10^4 and 5×10^5. For larger droplets, the drag force slightly varies, but it is not significant compared to the gravitational force. The drag coefficient for both side and front views show similar trends and ranges. Differences between the front and side view results are minimal. This indicates that the accuracy and consistency of measurements are correlated with the repetitiveness of the experiments. A corresponding drag force based on the calculated drag coefficient are shown in Figs. (6-6) and (6-7) for the flat-plate model and based on the side-view measured data.

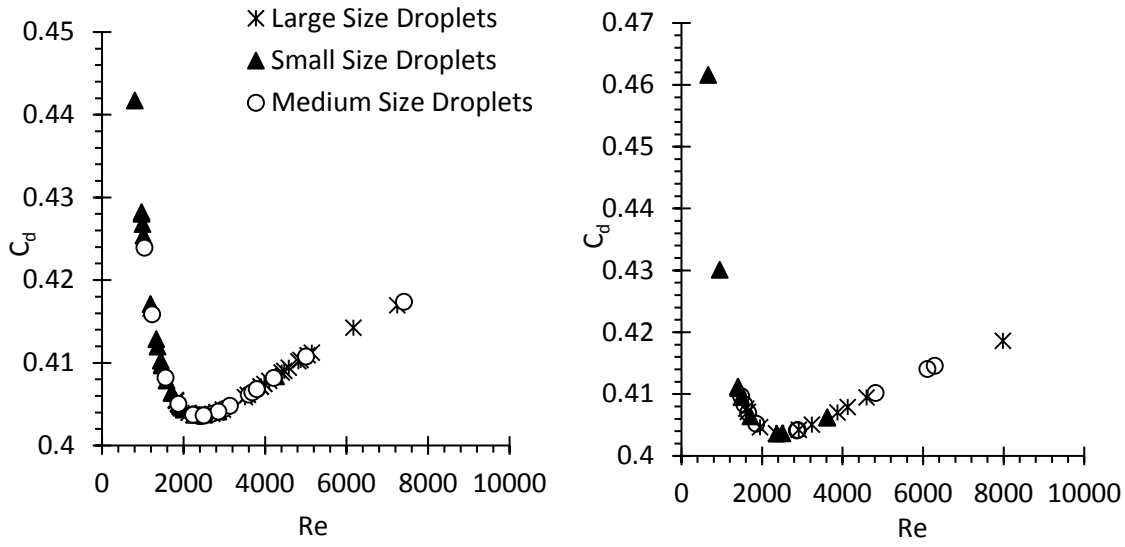

Fig. 6-5 Drag coefficient for three size ranges droplets calculated based on the side-view data for both models. Left: flat plate model, right: bow-shaped model.

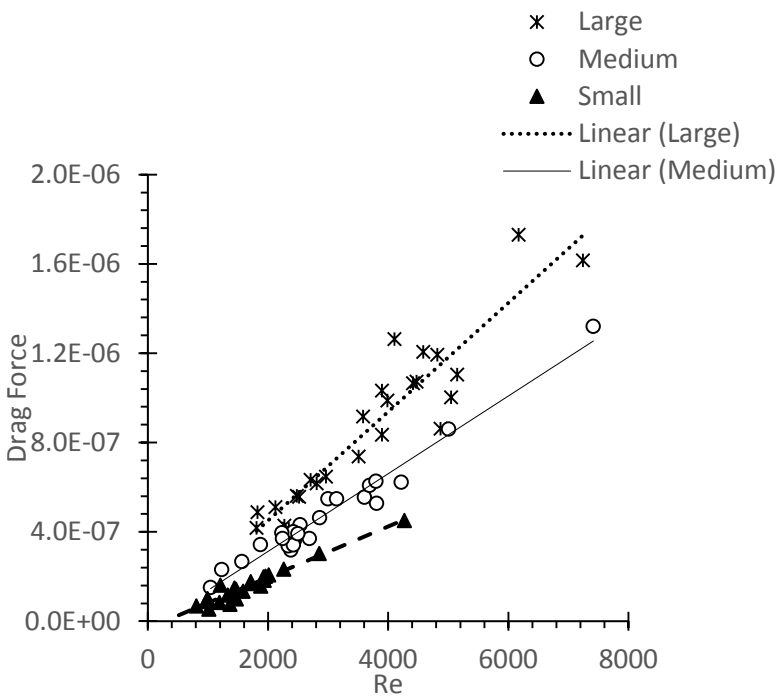

Fig. 6-6 The drag force on droplets as a function of Re number based on calculated drag coefficient.

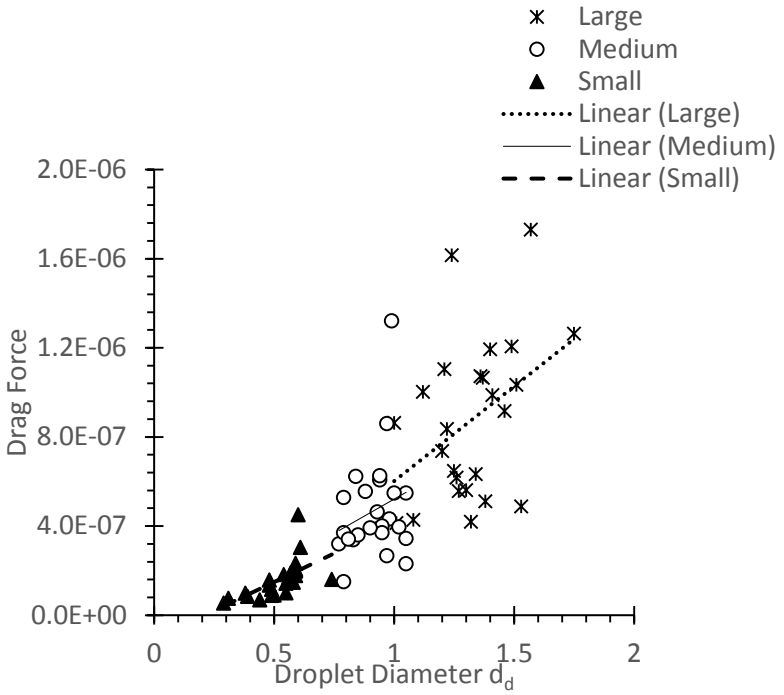

Fig. 6-7 Drag force on droplets as a function of droplet diameter based on estimated drag coefficient.

In addition, the deformation of liquid droplets has an effect on droplet velocity. In this experiment, the order of droplet velocities and sizes leads to different values for the Weber number, which is calculated as $\rho V_d^2 d_d/\sigma$, where ρ and σ are the density and surface tension of water, and V_d and d_d are the droplet velocity and diameter, respectively. The Weber number in different trials varied over a range of $30-500$, which demonstrates a broad range of this dimensionless number that is higher than previously documented critical Weber numbers, such as the bag mechanism $18 \leq We \leq 30$ and the transition mechanism $30 \leq We \leq 63$ (Cao *et al*., 2007; Lee and Reitz, 2000; Han and Tryggvason, 2001). This range of Weber numbers indicates that most of the droplets should experience a breakup. However, the results of the experiment indicate the opposite. This is thought to be because the droplets do not have enough travelling time to experience a breakup or alternately the instability growth rates in this case are low. Further, because of the resistance forces of drag and gravity, the instability in these droplets reduces and resists break up. Nevertheless, in some cases, droplet deformation and breakup were observed. In these cases, the Weber number is very large $(400 - 500)$ and, the droplets do have enough time to become unstable, which leads to a break-up. In contrast, small deformations do not lead to droplet breakup, and droplet surface tension tends to keep these droplets in a near-spherical shape.

In this experiment, small oscillations in the droplets were observed. These oscillations correlated with a deceleration of droplets, especially compared with non-oscillating droplets. This is due to the increase and decrease of drag force. It was observed that bigger

droplets ($1100 - 1500\ \mu m$) tend to oscillate more than small and medium droplets; droplet velocities and sizes play a significant role in this occurrence. Generally, droplets with a velocity lower than the average droplet velocities (flat-shaped plate model $2.8 - 3.5\ m/s$; bow-shaped model $2.5 - 3\ m/s$) are more likely to oscillate. This was quantified based on a statistical approach, and 300 individual droplets in various trials that are oscillating were picked to investigate their behaviors.

6.1.4 Pressure Measurements

The impact pressure of waves on the two models is calculated based on five sensors located on the flat-shaped plate model and three on the bow-shaped model. For each model, the maximum pressures have been computed based on the average of the two close sensors, because the maximum pressure is closely related to the location of pressure sensors on the objects. For low aeration impact, which happened when the wave impacted before the crest formed or after the wave completely breaks, the peak pressure tends to decrease as the height of the pressure sensors increases. However, pressure is generally uniform with respect to the width of the model. Further, for the high aeration impacts involving air entrapment, the impact pressure propagates away from the impact area with a fixed speed and longer duration. Similar behavior is reported by other researchers such as Bullock *et al.* (2007) and Bredmose *et al.* (2009).

The average maximum pressures from these sensors for both models, for several trials of different wave characteristics, are shown in Fig. (6-8). As this figure shows, impact loads

depend heavily on wave phase velocity. Waves with a higher velocity produce a higher maximum impact pressure. Formulations associated with the maximum pressure data were derived by curve fitting to find a relationship between dimensionless maximum pressure and wave velocity for both models. For a bow-shaped model, $P^* = 0.07\ V_m/V_c + 0.004$, and for a flat-shaped plate model the equation that fits the data is $P^* = 0.07\, V_m/V_c - 0.02$, where P^* is a dimensionless maximum pressure that was calculated as $p/\rho gH$. In this equation p is pressure, ρ is water density, g is gravity, and $H = 1.9\ m$ is the free surface height. V_m is the maximum wave run up velocity after the impact for each wave, which is varied from 1.60 to $2.2\ m/s$ for both models. The slope of the equation associated with both models is approximately equal. This indicates that a larger wave velocity produces a higher maximum pressure, and as a result, a higher droplet velocity. These equations are independent of the model geometries.

Maximum pressure measurements as a function of dimensionless wave heights for both models are shown in Fig. (6-9). Maximum pressure is related to wave height, and an increase in wave height leads to higher pressure in both models. The same procedure that was used earlier for fitting equations was followed by finding a relationship between dimensionless wave height and maximum pressure for both models.

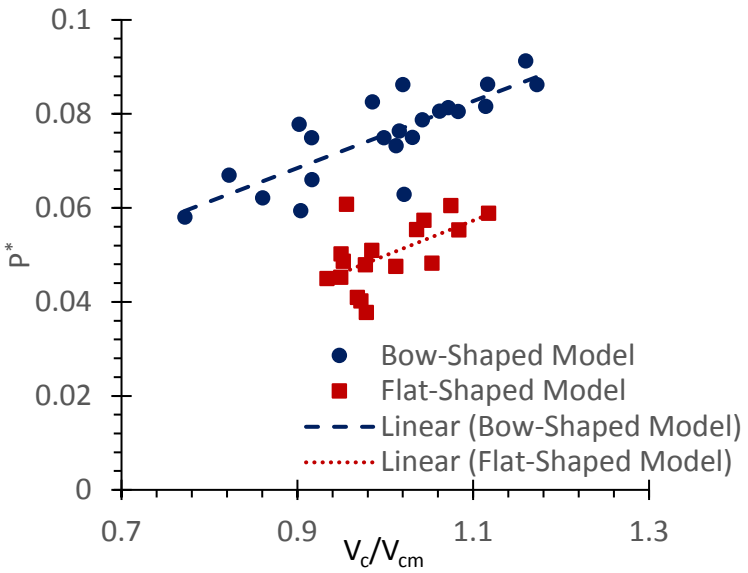

Fig. 6-8 Dimensionless maximum pressure $(P^* = p/\rho gH)$ as a function of dimensionless wave phase velocity (V_c/V_{cm}) for both models. The slope of both lines is equal to 0.07.

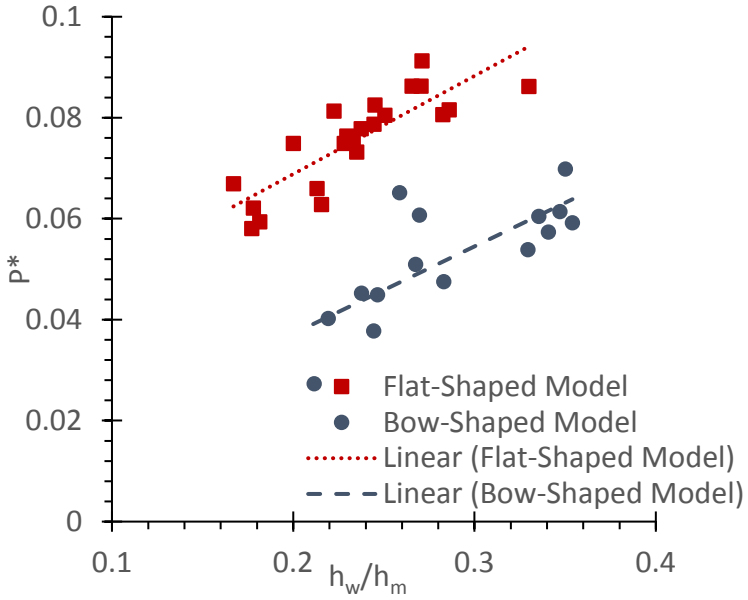

Fig. 6-9 Maximum impact pressure measurements as a function of wave height for both models. The slope of both lines is equal to 0.18.

The relationships between dimensionless maximum pressure and wave height for the flat-shaped plate and bow-shaped models are estimated by the following equations: $\mathrm{p}^* =$

$0.18\,h_w/h_m + 0.03$ and $p^* = 0.18\,h_w/h_m + 0.002$, respectively, where p^* is the dimensionless maximum pressure, h_w is a wave height, and h_m is the model height, which is constant and is equal to $1\ \mathrm{m}$ for both models. The slope of equations for both models are the same both indicating that an increase in wave height variations leads to an increase of impact maximum pressure. However, the magnitude of average dimensionless maximum pressure on the flat-shaped plate model $(P^* = 0.1)$ is higher than for the bow-shaped model $(P^* = 0.06)$.

Comparing the pressure sensor results to those reported by Fullerton *et al*. (2010) showed favorable agreement for similar wave-impact characteristics. The maximum, minimum, and average impact pressures for all the experimental trials using the three sensors on the bow-shaped model are presented in Fig. (6-10) and compare well with the results of other researchers' experiments. Fullerton *et al*. (2010) reported the maximum, minimum, and average impact pressure as 4.8, 1.5, and $3\ \mathrm{kPa}$, which is in agreement with the data presented in Fig. (6-10). However, the maximum pressure in our experiment differs by about $0.6\ \mathrm{kPa}$, which can be due to the positions of the pressure sensors and the wide range of wave characteristics used. The other reason is that, as described by other researchers (Greco *et al.*, 2007; Pergerine, 2003), it is common for impact pressures to vary, even over the same input conditions in an experiment; therefore, the comparison between different conditions can sometimes change.

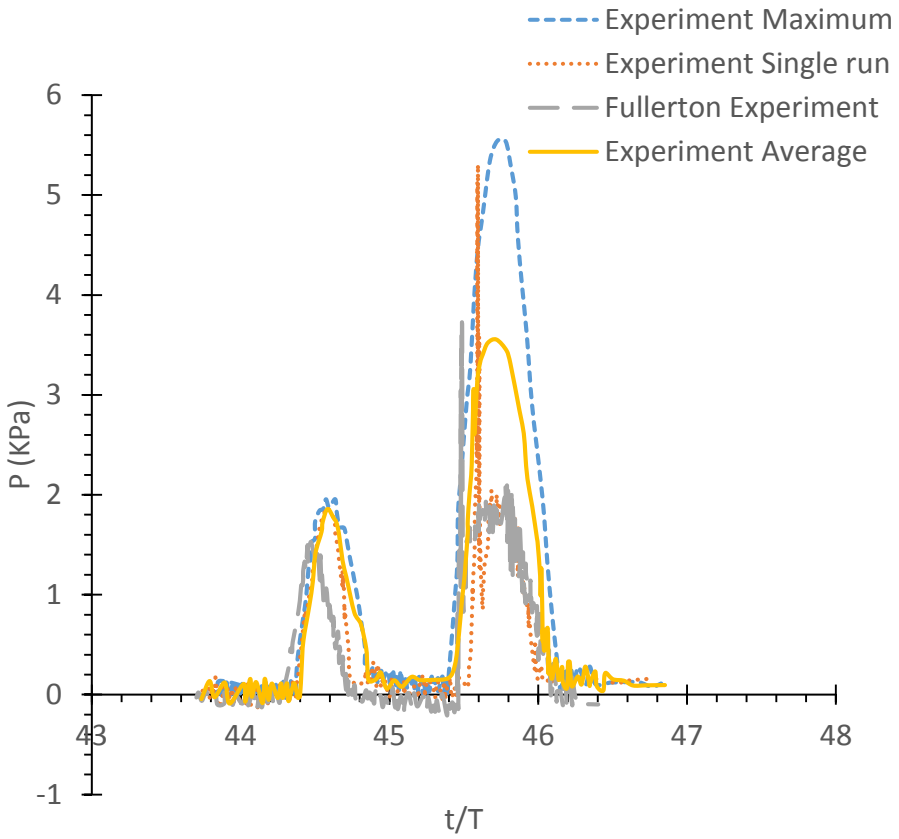

Fig. 6-10 Impact pressure for the maximum, minimum, and average pressure for the bow-shaped model and the experimental pressure measurements from Fullerton *et al.* (2010). The maximum and average pressures are based on the measurements for all trials.

6.2 Numerical Results

This section presents the results of numerical simulation of the interaction of a single nonlinear wave with a solid vertical surface in three-dimensions. A coupled Volume of Fluid (VOF) and Level Set Method (LSM) are used to simulate the wave-body interaction. A Cartesian-grid method is used to model immersed solid boundaries with uniform grid spacing for simplicity and to lower storage requirements. The behavior of the wave impact and the water sheet and high-speed jet arising from the impact are captured with these methods. The maximum wave run-up velocity, instant wave run-up velocity in front of the

vertical surface, the sheet break-up length, and the maximum impact pressure are computed for several wave characteristics. Results are compared with the previously discussed laboratory experiments. The numerical and experimental data on breakup length are further compared with an analytical linear stability model for a viscous liquid sheet, and good agreement is achieved.

The numerical case is shown in Fig. (6-11) matched with the geometry of the experiments. Inside a rectangular wave tank, a dam (flat plate) limits wave flow with an initial height of $0.9\ m$ from the bottom of the tank. The reference frame is set exactly at the initial location of the flat plate as $(0, 0, 0)$ and the free-surface level set as $0.2\ m$ above the x-axis, which means that $0.2\ m$ of the flat plate is located under the water. The input wave condition was introduced at the inlet and the numerical beach (damping) condition introduced at the outlet to absorb the incoming waves.

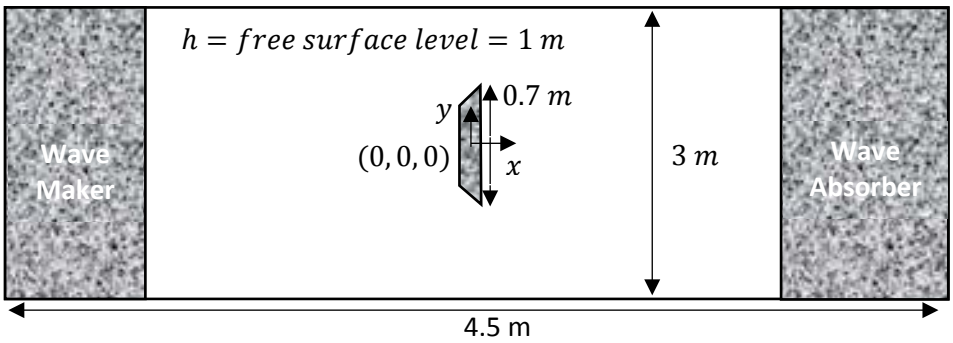

Fig. 6-11 A numerical wave tank with a lab-scaled flat-shaped model in the middle of the tank.

6.2.1 Free surface and Velocity

The simulated results of splashes shown in Fig. (6-12) are similar to previous simulations of the effects of water-dam impact, presented by Greco and Lugni (2012a; 2012b), which used a weakly nonlinear seakeeping solver to model the impact of a three-dimensional dam breaking flow with an obstacle. The current numerical modeling of wave impact with the lab-scale model is also compared in time with three-dimensional Smooth Particle Hydrodynamic (SPH) results reported by LeTouze *et al.* (2006), which simulated the impact of water on an object and subsequent breakup behavior, which included a qualitative comparison with wave impact splashes and shows good agreement. For better clarity, results of current modeling are shown in Fig. (6-12) from two different views, one containing the flat-plate (left) and one without the flat-plate from the rear view (right).

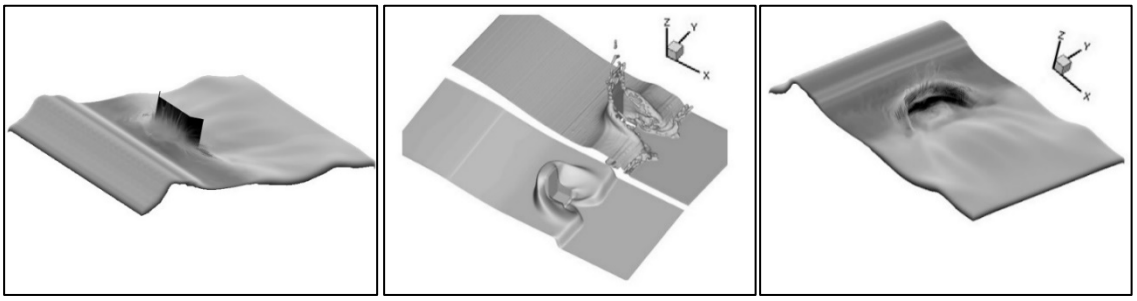

Fig. 6-12 Comparison of qualitative perspective views of water splashes when wave impact with an object in (left) the present numerical model from the front view, (middle-bottom) the Greco and Lugni (2012b) model, (middle-top) SPH results by LeTouze *et al.* (2006), and (right) the present numerical model from the rear view.

When the water impacts the flat object, it rises and starts to break-up due to acceleration. The water acceleration after the impact can be due to (1) impact pressure and/or (2) air entrainment, which force the water upwards. At the side of the object, two

arms of water are produced which do not have a high velocity compared to the water in front of the object. There are three differences between the present simulation and those reported by Greco and Lugni (2012b) and LeTouze *et al.* (2006) exist. First, in this simulation, the object is already submerged in the water, and the water level is set at $0.2\ m$ above the initial position of the object. Second, a two-phase flow was considered and both water and air entered the control volume domain with the same velocity. Because of this, the effect of air with an inlet velocity $1.5 - 1.85\ m/s$ clearly affects the spray and breakup conditions after the impact. Third, the effect of water slamming at the wave tank rear end is eliminated by using the numerical beach condition to absorb the wave reflection. Due to the computationally expensive nature of CFD for this multi-scale problem, the grid size is refined only in front of the object. Grid sizing plays a significant role in this problem for capturing breakup and spray. Thus, the behaviors of breakup and spray behind the object are not examined entirely properly due to this limitation.

Fig. (6-13) shows the velocity vectors at the moment of impact for four different time steps in sequence. The water after the impact produces a high-velocity jet in front of the plate, and a significant amount of air (second phase) is trapped between the water and the plate. It is not yet clear how this trapped air influences the pressure, but it is likely that the trapped air pressurizes the water and accelerates the fluid in front of the model, which causes the high-velocity jet leading to sheet breakup. As is clear in this figure, the intensities of the velocity vectors are high and this is because of more clarification in displaying the air entrapment and wave run-up vectors.

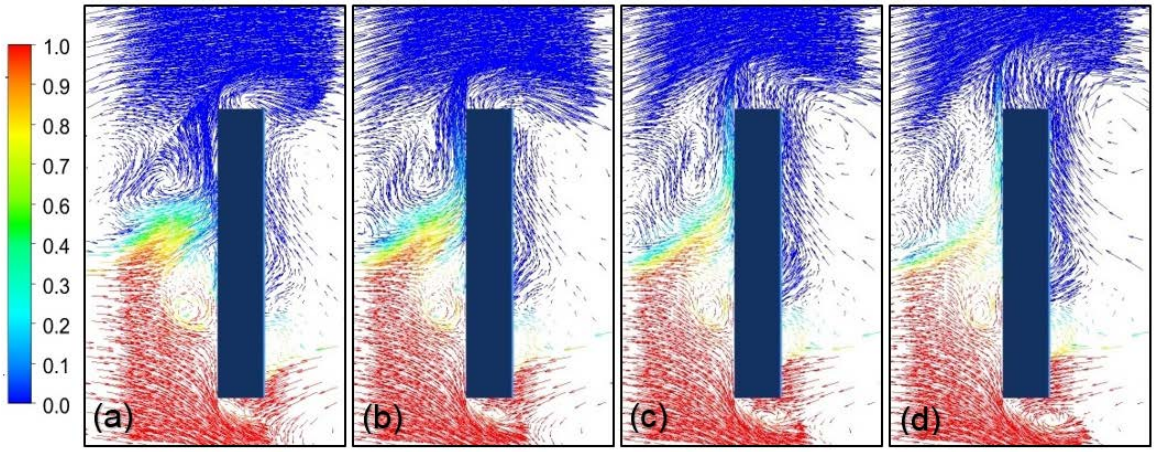

Fig. 6-13 Velcity vectors in front of the model at the moment of impact. Water and air are colored as red and blue, respectivly: Three time steps after the moment of impact (a) $t = 0.08\ s$, (b) $t = 0.14\ s$, and (c) $t = 0.2\ s$.

Figure (6-14) shows a time step of velocity vectors colored by velocity magnitude at the moment of water-sheet acceleration, which is $0.05\ s$ after the moment of impact. As the global behavior of the water, as it moves from waves to spray production, is very similar to that observed in the experiment, it can be concluded that the numerical methods and initial conditions provide a useful model and a good approximation in modeling this problem. As is clear in Fig. (6-14), after the impact, water rises along the vertical axis in front of the plate and is accelerated by the impact pressure and the air that is trapped by the impact. From the numerical modeling results, it can be seen that the wave impacts the plate with a velocity of $1.7 – 3.2\ m/s$ (Fig. 6-14a) and accelerates after the impact to a maximum velocity of $3.8 - 5.2\ m/s$ (Figs. 6-14b and 6-14c). The high-velocity jet reaches twice the velocity of the wave impact. Finally, the jet decelerates due to gravity and drag force in the spray-cloud area (FOV2) and finally reaches the velocity of the air that is blowing on top of the model, with a velocity of $1.7 - 2.8\ m/s$ (Fig. 6-14d).

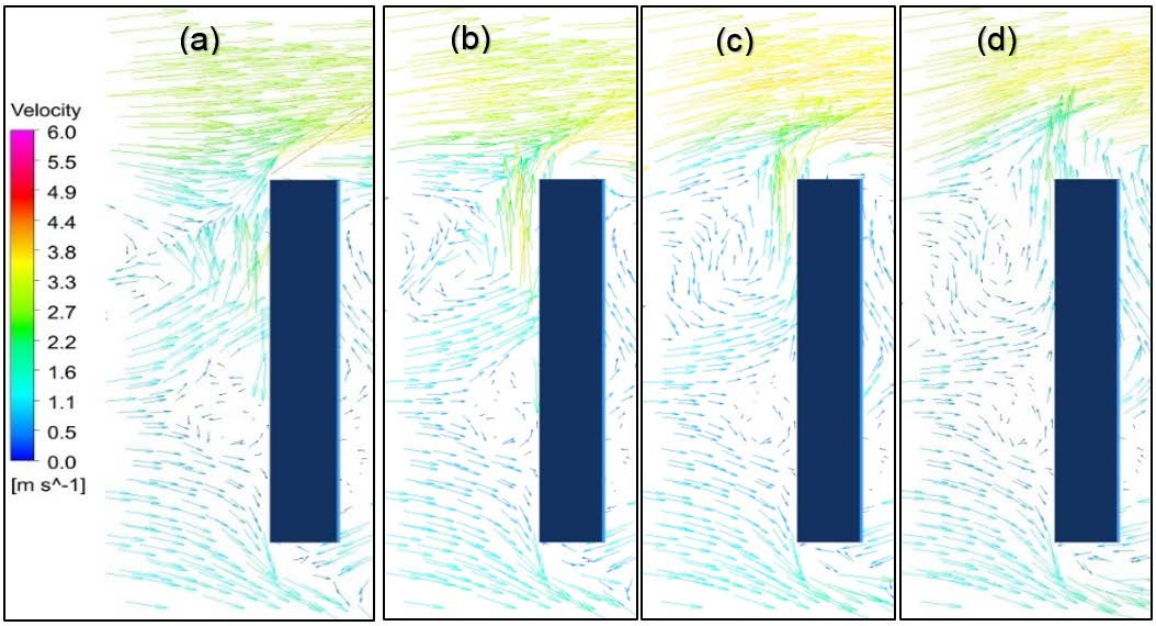

Fig. 6-14 Velocity vectors colored by velocity magnitude at the moment of water sheer acceleration in front of the model for four different time steps after the moment of impact, each 0.06 s ahead of the other.

By referring to the experimental results, a similar velocity distribution from the moment of wave impact until the water reaches the spray cloud area was achieved. In this experiment, the wave-phase velocity at the time of impact was calculated as $1.7 – 2.8$ m/s for different wave conditions. After the impact, water accelerates to a velocity of $3.8 – 5.2$ m/s, which varies for different droplet sizes. Figs. (6-15a) and (6-15b) show the velocity magnitudes of 25 samples in front of the models in both the experimental and numerical models, respectively. The differences between the velocity magnitude in the wave run-up region betweem the experimental and numerical results are because of the availability of air velocity at the top of the numerical flat-plate model. In the numerical simulation, all the droplets reach the velocity magnitude of the air at the region above the

tip of plate. However, for the experimental results, droplet velocities are reduced to zero velocity due to drag and gravity forces.

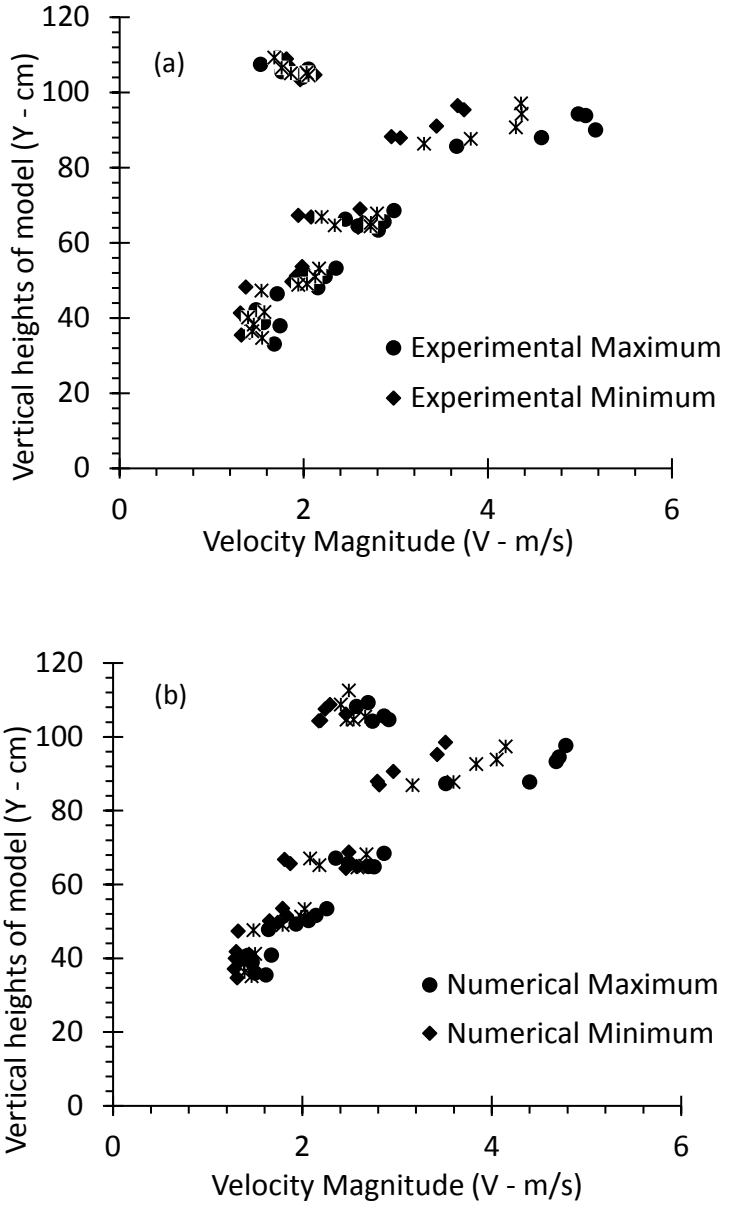

Fig. 6-15 Maximum, minimum, and average velocity magnitude of droplets in front of the flat-plate model along the vertical height of the model: (a) experiment simulation; (b) numerical simulation.

Fig. (6-16) shows the comparison between the numerical and experimental results. As is shown in this figure, the discrepancy between both results is about 5% for the velocities at the wave impact and water sheet formation locations. At the locations close to the tip of the plate with high jet velocity, the differences between numerical and experimental results are higher, and at the top of the plate, velocities from models are different because of different boundary conditions.

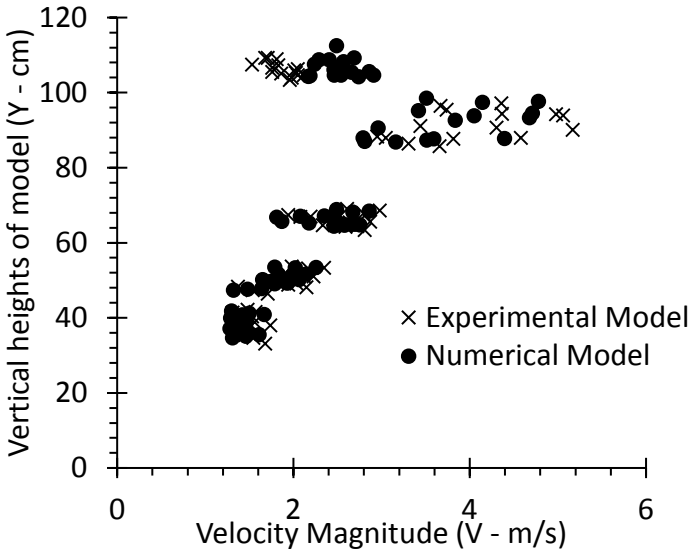

Fig. 6-16 Comparison between velocity magnitude of droplets in front of the flat plate model along the vertical height of the model in both experimental and numerical simulations.

The results show that small-size droplets have the highest average velocity, and large-size droplets have the lowest range of velocities compared with medium-size droplets. Only medium size range droplets can reach the maximum height. Due to drag force acting on the small size droplets and gravity force acting on the large-size droplets, these smaller and larger sized droplets cannot reach the spray-cloud area and maximum spray height.

For comparison between the numerical and the experimental results, the most common behavior is a production of the mixed flow of water sheet and droplets, illustrated in Fig. (6-1) for the experimental results and Fig. (6-17) for the numerical results. The experimental figures show the droplet distribution only from the tip of the model (Fig. 6-1). However, the numerical figures show the process of spray production from the moment of wave impact. Both numerical and experimental results show the distribution of a spray cloud after impact on the top of the tip of the model. As images (b) and (c) of each figure show, the distribution and amount of water that transfers to spray are identical. However, the distribution of droplets shown in Fig. (6-17) is different due to the mesh-size limitation for the numerical simulation ($3.5\ mm$ in grid spacing), in which small droplets cannot be captured. In addition, the air velocity in the numerical simulation on top of the numerical model is set at the same velocity as the wave-phase velocity at inlet, but in the experimental simulation this condition was not maintained.

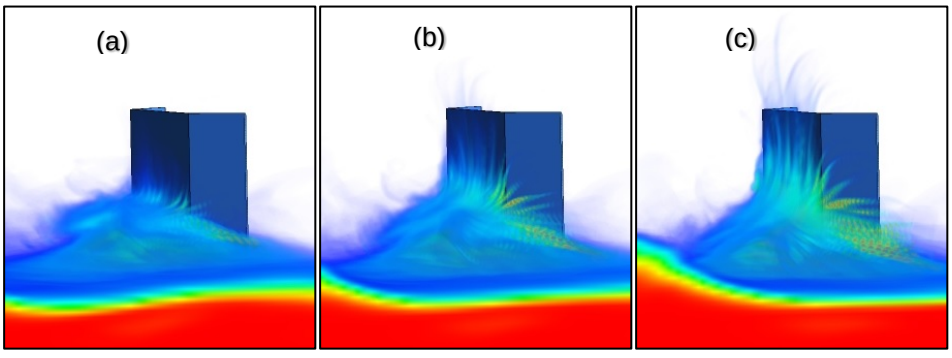

Fig. 6-17 Time sequences of numerical results for a common type of impact which consists of both water sheet and spray cloud. (a) $t = 0.08\ s$, (b) $t = 0.14\ s$, and (c) $t = 0.2\ s$.

6.2.2 Linear stability analysis

The breakup of the liquid sheet in the process of wave spray production undergoes a complex and unsteady process. The breakup length of the liquid sheet L_b is among the most significant parameters in the process of wave spray production. Fig. (6-18) shows a schematic description of the length of breakup. Linear stability analysis, presented by Dombrowski and Johns (1963), can evaluate the beginnings of instability of the liquid sheet and can provide sufficient information regarding the unstable, wave type behaviour of the liquid sheet as disturbances grow.

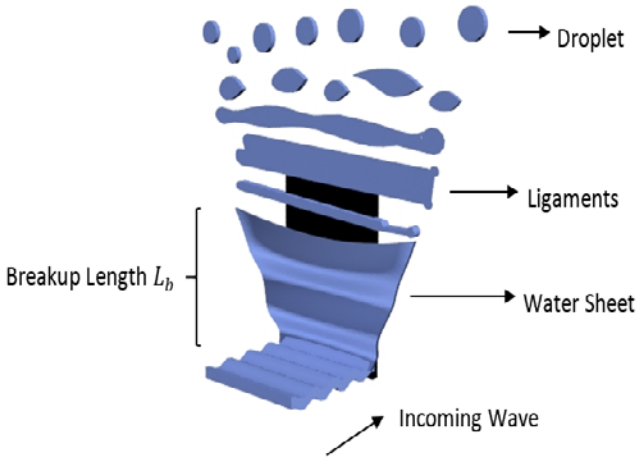

Fig. 6-18 Schematic determination of sheet breakup length.

Based on an analytical approach by Dombrowski and Johns (1963), the displacement of the inner and outer surface of a two-dimensional liquid sheet moving in a gas medium with the velocity of U_s can be calculated as:

$$\eta = R\eta_0 \exp(i(kx - \omega t) \tag{6-5}$$

where η is the fluctuation amplitude, $k = 2\pi/\lambda$ is the wave number and λ is the wavelength of the disturbance wave. ω is an imaginary number and the real part represents the disturbance frequency and the imaginary part represents the growth rate of disturbance.

The final dispersion relation for a planar liquid sheet is presented by Dombrowski and Johns (1963) as a second-order polynomial relation:

$$\left(\frac{\omega_i h}{U_s}\right)^2 + \frac{(kh)^2}{Re_s}\left(\frac{\omega_i h}{U_s}\right) + 2\frac{\rho_g}{\rho_l}(kh)^2\left(\frac{\rho_l}{\rho_g}\frac{1}{We_s} - \frac{1}{kh}\right) = 0 \tag{6-6}$$

where $Re_s = \rho_l U_s h/\mu$ is Reynolds number of the liquid sheet, $We_s = \rho_l {U_s}^2 h/\sigma$ is the liquid sheet Weber number, ρ_g and ρ_l are gas medium and water density, respectively, and h is the half of water sheet thickness (t_s). The liquid sheet velocity (wave run-up velocity) after the wave impact with the model was extracted based on the experimental measurements. Finally, the breakup length can be calculated based on the $L_b = U_s \tau_b$, where τ_b is the breakup time, which can be calculated as:

$$\tau_b = \frac{\ln\left(\frac{\eta_b}{\eta_0}\right)}{\omega_i} \tag{6-7}$$

All the parameters in these equations are known except $\ln(\eta_b/\eta_0)$, which needs to be decided based on experimental data in different cases. This is because η_0 changes with the inlet flow geometry and liquid flow conditions (Kim *et al.,* 2007). In this study, based on the result of the conducted experiments, the value of $\ln(\eta_b/\eta_0)$ was taken to be five. It should be noted that the value of $\ln(\eta_b/\eta_0)$ is uniquely related to each case study and should determine based on experimental or field observation data. Fig. (6-19) shows breakup length as a function of Weber number determined from the analytical approach, which is compared with the average results extracted from the numerical and experimental simulations. The breakup length decreases with increases in the liquid sheet Weber number. The analytical approach is in good agreement with the results extracted from both experimental and numerical results with less than 10% error. As is clear from this figure, the numerical and analytical results are in high precision agreement with each other. Further, the experimental results are based on averaging the breakup length for 10 trials. The error bars show the maximum and minimum breakup length in different trials. Overall, the agreement between all these approaches is considered satisfactory.

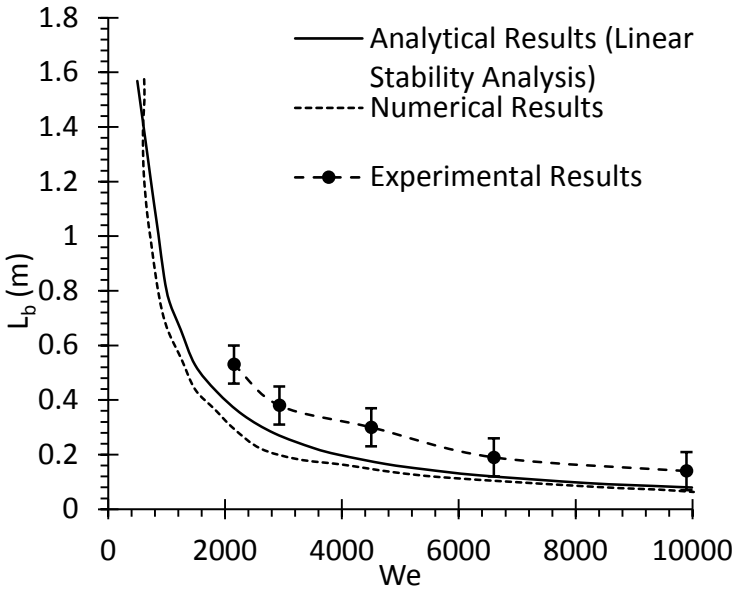

Fig. 6-19 Comparison between the numerical and analytical predictions with experimental results of liquid sheet breakup length based on a change in Weber number.

6.2.3 Pressure

During the experiment, several measurements were performed to compare the experimental results with the numerical results. Wave height (free-surface elevation) at three different positions, the impact pressure of waves on a flat-plate at five locations, and a qualitative analysis of wave impact acquired with the high-speed camera were used to compare the results of both simulations. Maximum, minimum, and average pressure measurements from the experiment are compared with the numerical results and those of Fullerton *et al.* (2010) and Greco and Lugni (2010b) in Figs. (6-20) and (6-21).

Fig. (6-20) shows the maximum, minimum, and average pressures from the experiment, which is in good agreement with the results of Greco and Lugni (2010b) presented in Fig. (6-21). The maximum pressure peaks from the Fullerton *et al.* (2010)

experiments are $0.2\ kPa$ and $0.8\ kPa$ higher than the others. As described by other researchers, it is very common that impact pressures vary over the same conditions in the experiment, so the comparison between different conditions can sometimes vary. However, the maximum and minimum range of values reported in most of the research in this area are the same. Maximum pressure measured by experiment and numerical simulation differs by about $0.5\ kPa$, which indicates that the numerical model under-predicts the pressure (Fig. 6-22). This discrepancy can be explianed based on pressure sensor reading errors due to wave reflections and due to sensor uncertainties. Another reseaon for this discrepancy is the train of wave-reflection pressure in both the numerical and the experimental simulations. When the wave impacts the flat-plate, a portion of wave energy is reflected and added to the next wave, which cause higher pressure. However, the results of average pressure measurements for both models and those reported in other references are matched with a discrepancy of less than 10%,.

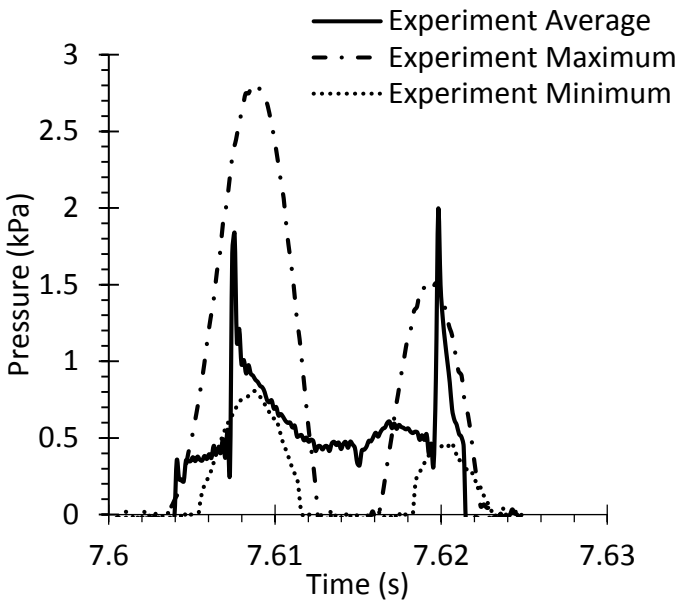

Fig. 6-20 Maximum, minimum, and average pressure measurements from the experimental modeling of wave impact with a flat plate on pressure sensors B and C.

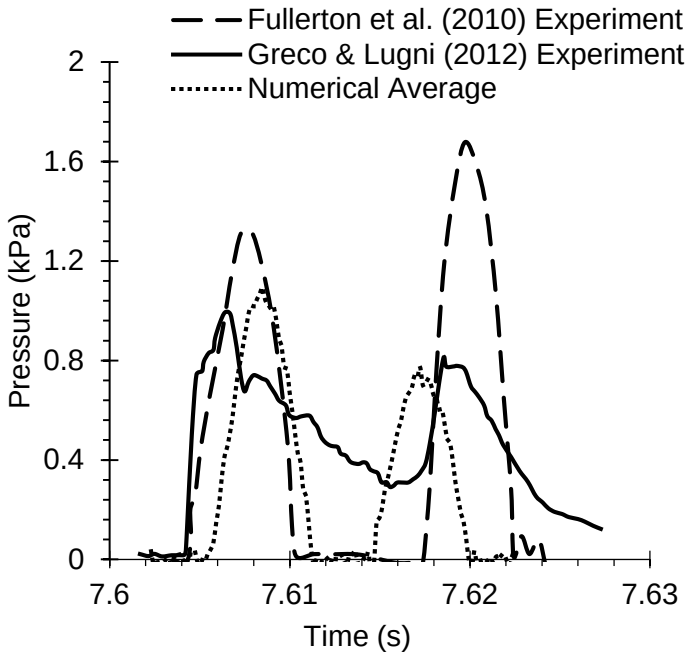

Fig. 6-21 A Comparison between the average of the numerical results, the Fullerton *et al.* (2010) experiment ,and the Greco and Lugni (2012b) experiment.

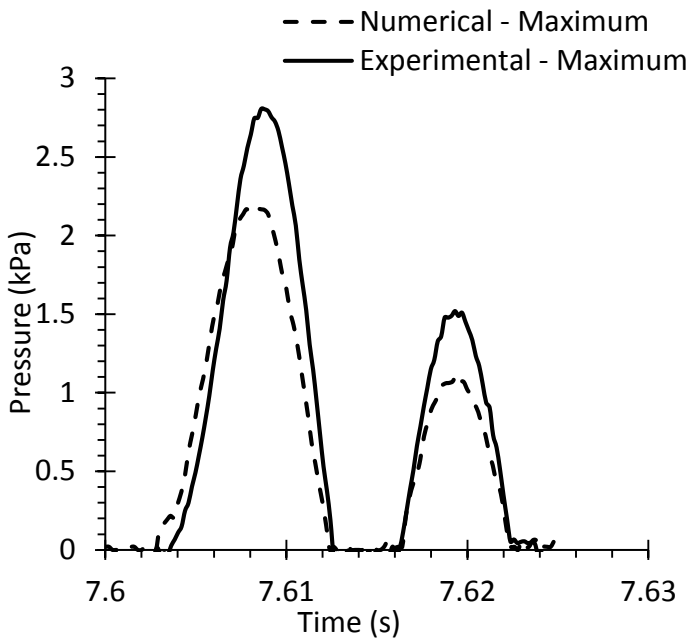

Fig. 6-22 A Comparison between the numerical and experimental maximum impact pressure on the flat plate. A small overprediction by the experimental method can be due to wave reflection and pressure sensor uncertainties.

6.3 MEP Results

This study addresses the development of a statistical tool for predicting the distribution of the size and velocity of droplets in spray caused by the interaction of waves with a marine object. A set of significant conservation constraints that govern the flow behavior, which is significantly important in the process of spray cloud formation resulting from the wave impact, were introduced and applied to both one- and two-dimensional cases. The size and velocity distribution arising from the maximization of the entropy is subject to these constraints. The prediction distribution is compared with the result of the experiment in a small scale spray due to the wave impact, and it is more accurate than the prediction results from the one-dimensional MEP. The prediction model further imposed to the full-scale conditions and is compared with the 1-D results of MEP by other

researchers. The effect of a drag force on both the liquid sheet that is formed from the wave impact as well as the downstream distribution of droplets was considered in this simulation.

6.3.1 One-dimensional MEP

The control volume extends from the time of impact to the breakup region for the first simulation stage, and to the spray region for the second simulation stage. In this simulation, the mass source term is assumed to be zero, which indicates that the breakup and spray are isothermal and enter the still air surrounding the control volume. As described before, two drag forces were considered: a drag force acting on the flat sheet in the breakup region, and a drag force acting on individual droplets in the spray region. The first drag force was estimated based on a flat triangular sheet of water exposed to the environment. However, the majority of the water sheet and the spray clouds either move vertically close to or attach to the model. Based on the geometry of the impact region, the impact area can be calculated as the area of a trapezium (Fig. 4-1). For the wave impact with the bow-shaped plate model, the breakup length is $L_b = 380\ mm$ on average. Since the width of the model is $b_b = 200\ mm$, the width of the sheet at the final distribution moment (the moment from breakup to spray) is $c_b = 300\ mm$; this indicates that the water sheet tends to spread about $50\ mm$ from both sides of the model. Since the width of the flat-shaped plate model is $b_f = 1000\ mm$, the breakup height is approximately $L_f = 485\ mm$, and the width of the sheet at the final stage of distribution

is $c_f = 1200\ mm$, which indicates that the water sheet spreads about $100\ mm$ from both sides of the model (mostly symmetrical).

Similar to a flow sheet from a nozzle, the boundary layer flow for the flat sheet due to the wave impact is laminar, and the Reynolds number is within the confines of the critical Reynolds number (5×10^5). By using Eq. (4-7), or the Blasius relationship, and the average velocity of the water sheet, the drag coefficient of one side of this flat sheet is calculated as $C_D = 0.0052$ for the bow-shaped model and as $C_D = 0.0046$ for flat-shaped model. By using these values in Eq. (4-10), $\bar{S}_{mu}$ is estimated as 3.075×10^{-5} for the bow-shaped, and $\bar{S}_{mu}$ is estimated as $= 3.057 \times 10^{-5}$ for the flat-shaped plate model. Moreover, the average drag coefficient for the second region, which only contains the spray, is calculated for both lab-scale models as $C_D = 0.91$. By using these values in Eq. (4-11), the momentum source term is calculated for both models as $\overline{S}_{mu} = 9.42 \times 10^{-4}$.

Furthermore, on larger scales, such as vessels and offshore structures, by considering that the mean wind velocity is equal to $21.6\ m/s$ based on the field observation of Ryerson (1995), and the wave phase average velocity at the moment of impact is equal to $25.2\ m/s$, the average water sheet velocity after the impact reaches $41.2 - 55.8\ m/s$. This calculation is based on the lab experiments reported by Ryu *et al*. (2005; 2007). The drag coefficient and momentum source term for the primary region were calculated as $C_D = 0.0004$ and $\bar{S}_{mu} = 1 \times 10^{-5}$, and for the secondary region, they were calculated as $C_D = 0.44$ and $\bar{S}_{mu} = 7.29 \times 10^{-4}$.

As mentioned before, two different control volumes were considered in this method. First, the control volume that extends from the moment of impact (which forms the bottom side of a parallel trapezoid) up to the moment of ligament and droplet formation (which forms the top side of the parallel trapezoid). Second, the control volume that extends from the moment of ligament and droplet formation up to the moment that these droplets reach the maximum height. The drag coefficient for the droplet region is much higher compared to the water sheet region, which indicates that the drag force is a significant factor in this stage of the process. The velocity profile at the impact moment is assumed to be uniform, and the sheets are distributed uniformly on the objects, which leads to $H = 1$.

For the spray experiment in the laboratory, it is assumed that there is no mass transfer and the ambient air is fully saturated. However, for the sake of simplicity, this was not considered in the large-scale data. Similarly, the energy source term, which is the amount of kinetic energy transferred to the liquid sheet and the droplets, was considered to be approximately zero, but in reality, this energy transfer should be taken into account.

The results of the predicted and measured size and velocity probability distributions for droplets in front of both lab-scaled models are shown in Figs. (6-23) and (6.24). These probability distributions are based on the average of all sample data for specific wave phase velocities $(2.2\ m/s)$. As is demonstrated in this figure the peak of nondimensional droplet diameter for the predicted model is 0.6 lower than the experimental results. This discrepancy can be because of errors and uncertainties related to the experiment

measurements. Moreover, the diameter and distribution of droplets were measured on a specific plane in front of the models and the presence of droplets in 3-dimensional were not considered in the experiment. However, the peak of nondimensional velocity for both predicted and experimental results are the same. Fig. (6.25) shows the predicted size and velocity probability distributions for droplets in front of a large-scale model. This results are based on the measured field observation values that are reported by Ryerson (1995) on a U.S. Coast Guard cutter. Comparison between the results of small scale and large scale models conclude that higher initial velocity of impact leads to shift of curve of distribution around a specific nondimensional droplet diameter and velocity, which indicates that in large scale most of droplets tends to have a narrow size range of diameters and velocities. Also for large scale, the droplet size are smaller than the small scale models, which shows that the breakup phenomena is significant in this wave impact process and should be considered for the study of spray formation from the wave impact.

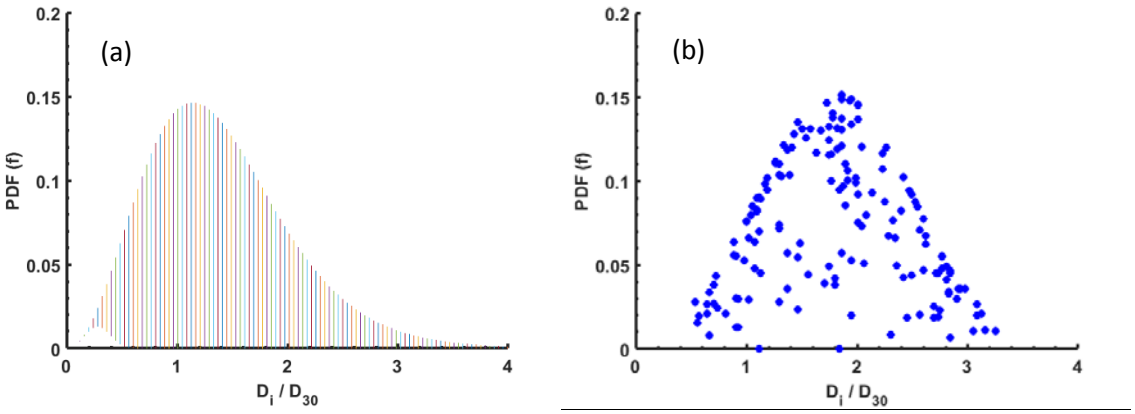

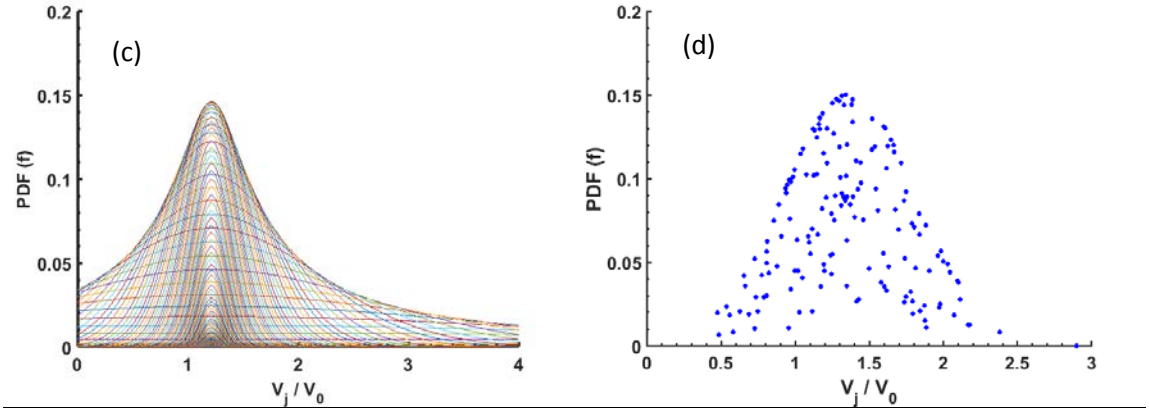

Fig. 6-23 The probability distribution of droplets as a function of droplet sizes and velocities. (a, c) Predicted model for the flat-shaped plate model, (b, d) The experimental probability distribution for the flat-shaped plate model.

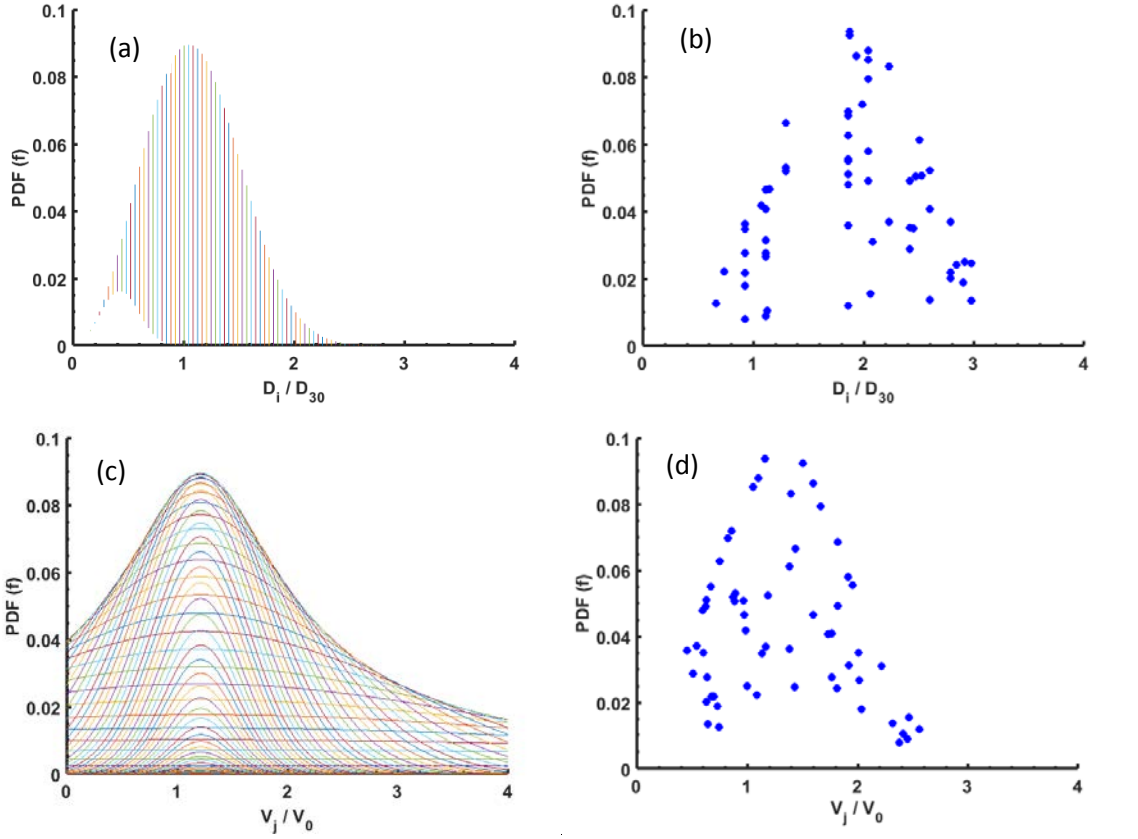

Fig. 6-24 The probability distribution of droplets as a function of droplet sizes and velocities. (a, c) Predicted model for the bow-shaped plate model, (b, d) The experimental probability distribution for the bow-shaped plate model.

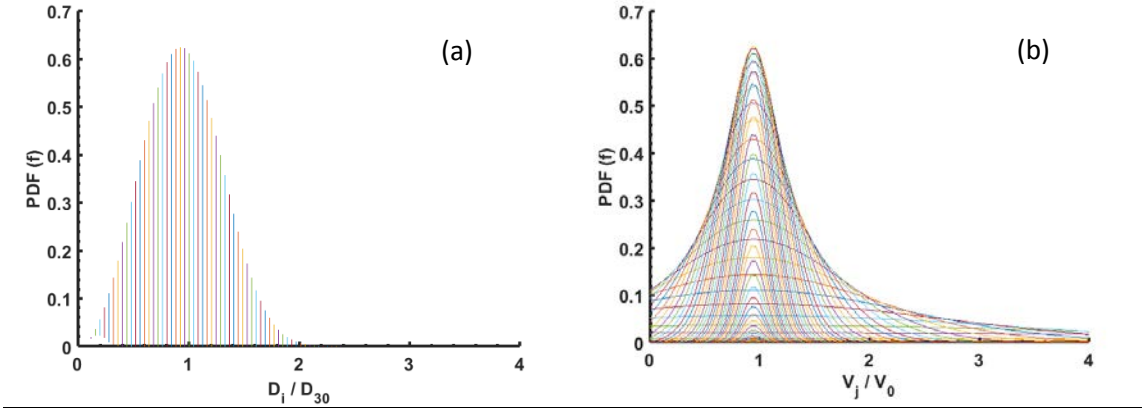

Fig. 6-25 The probability distribution of droplets as a function of droplet sizes (a) and velocities (b) for the large-scale case based on the initial values reported by Ryerson (1995).

By using the set of governing equations (Eqs. 4-1 – 4-5) and the parameter values described earlier, the probability counters of size and velocity of the water sheet for all three models were demonstrated in Fig. (6-26). This figure shows that the probability of the presence of droplets with a specific size and velocity is in agreement with the experimental results for both flat plate and bow-shaped models. The probability of the presence of medium size droplets with an average class velocity is higher than the probability of the presence of droplets with large sizes and small sizes.

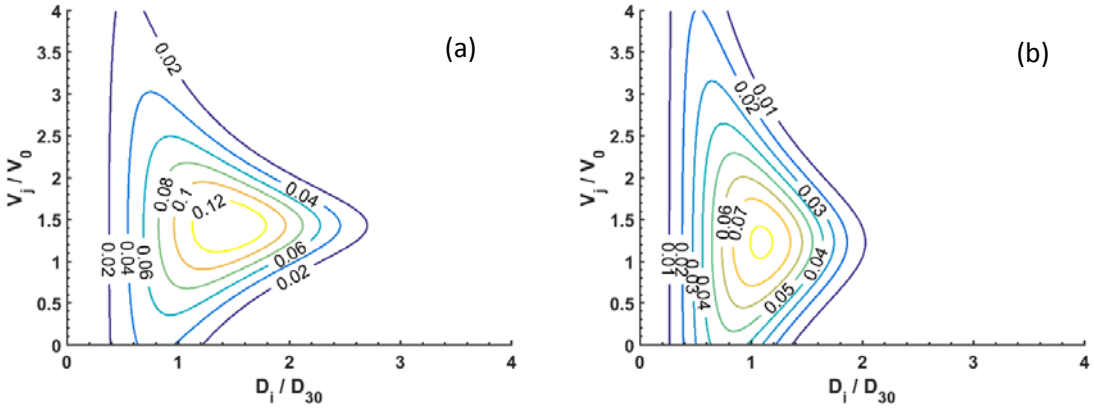

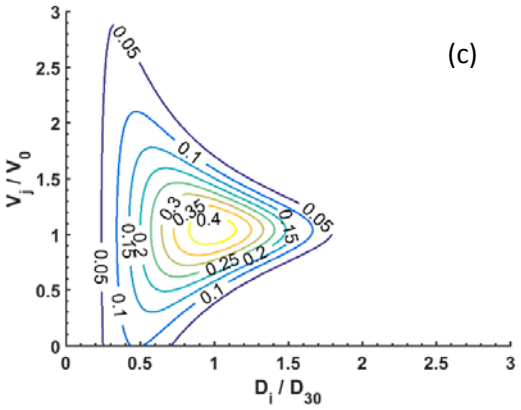

Fig. 6-26 The predicted probability contour of joint nondimensionalized size and velocity distributions. (a) Flat-shaped model (b) Bow-shaped model (c) Large-scale model.

Fig. (6-27) shows the droplet size distribution ($dN/d\bar{D}$) for all three models based on Eq. (4-14)**.** These graphs show the effect of various initial velocities on the droplet size distribution. As the initial velocity of impact increases, the distribution curve shifts towards the larger droplets and in consequence leads to larger distributions. The peaks of the distribution curves increase when the initial velocity increases. This is due to an increase in the value of the Weber number, which is a result of the creation of surface area. This can be explained based on the definition of the Weber number: the surface energy of the droplets decreases relative to the total energy of the spray droplets. This causes the formation of larger droplets. For the large-scale model, the distribution curve shifts towards the smaller range of droplet sizes (Fig. 6-27c) due to a decrease of mass mean diameters and greater values of initial sheet velocities. In this case, the quantity of droplet sizes in the medium range extensively increased compared to small-scale models.

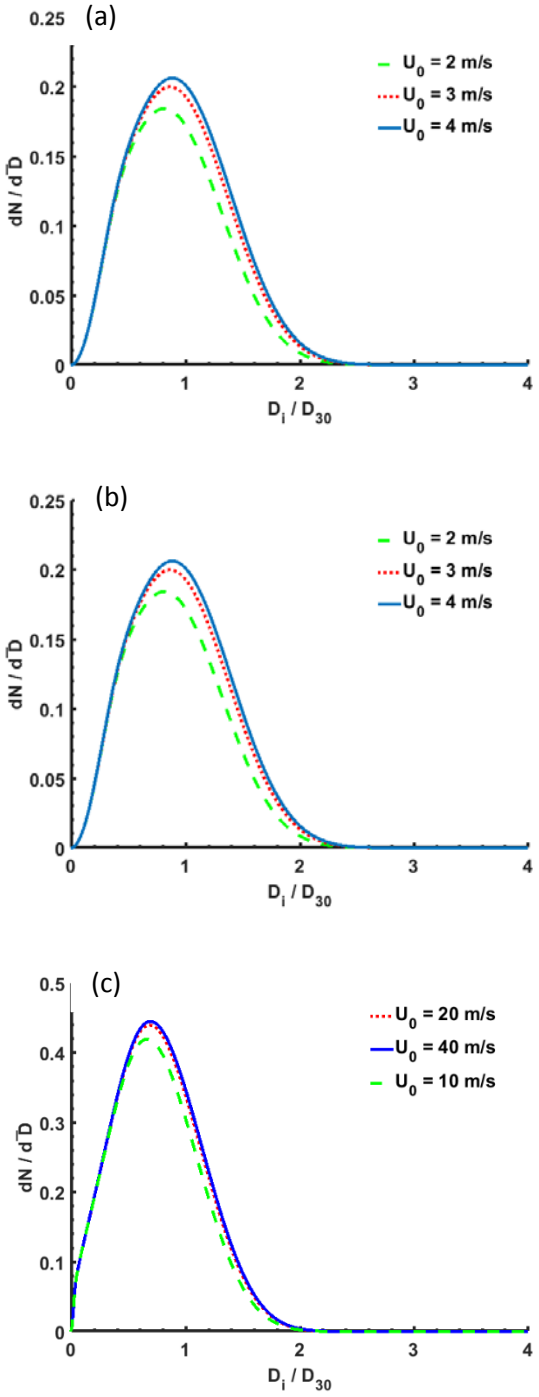

Fig. 6-27 Effect of initial sheet velocity on droplet size distribution. (a) Flat plate model (b) Bow-shaped model (c) Large-scale model.

The Fig. (6-27) shows the results of the prediction model for the case, which the effect of the drag force was only considered on the water sheet, and the results are only utilized in the primary part of this simulation. In the next step, the drag force on droplets is added to the momentum source term, and the control volume is extended from the moment of wave impact to the maximum height of the spray cloud, which covers water sheet formation, water sheet breakup, and droplets. Other important phenomena in the secondary breakup zone, such as turbulence, collision, coalescence, and gravity effects are ignored because they would add complications to the governing equations. The new momentum source is calculated based on the calculation of the drag force on each category of droplet sizes and velocities. The summation of these individual drag forces for each droplet leads to the computation of a new momentum source term. However, this requires the assumption that droplet transition from the primary stage of breakup to the secondary stage of spray formation is a steady process. In future research, this assumption will no longer be required if a turbulence model is considered. The size distribution result for droplets with the added drag force for both regions on the large-scale model is shown in Fig. (6-28). As this figure shows, the distribution of medium size droplets is narrower in comparison with the previous distribution that did not consider the secondary region drag forces. Moreover, the size distribution of medium class droplets is greater than the previous prediction model. The effect of the initial velocity of the water sheet is illustrated and indicates that higher initial velocity produces larger droplet size distribution. However, this velocity effect is not very significant.

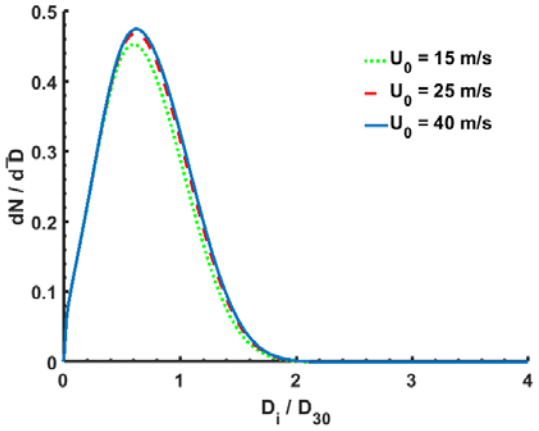

Fig. 6-28 Effect of initial sheet velocity on droplet size distribution in the model consists of the effect of drag force on both primary and secondary regions of flat-shaped plate model.

6.3.2 Two-dimensional MEP

The results of droplet size and velocity distribution from the experiment using the BIV and PIV methods compared with the results of the theoretical model all showed similar characteristics. A control volume considered that extends from the moment of impact, at the bottom of a model, up to the area that ligaments and droplets are formed. In this simulation, the isothermal assumption for the breakup and spray is lead to the mass source term is equal to zero. The results of the predicted and measured droplet size distributions in front of a flat-shaped lab-scaled plate model are shown in Fig. (6-29) for three different wave phase velocities, respectively. The experimental probability distributions for each wave phase velocities are based on the average of all sample data for a particular wave.

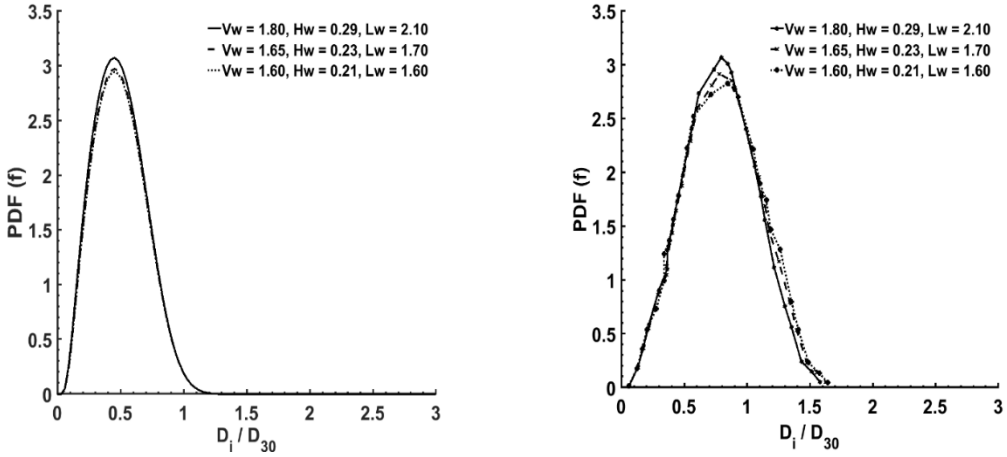

Fig. 6-29 Droplet size distributions for three different wave characteristics: a) Theoretical prediction model, b) Experimental model

A comparison between theoretical data and measured experimental data shows satisfactory agreement as the peak of probability distributions shifted with a discrepancy of less than 20%. Also, the experimental results show larger droplet size distribution in comparison with prediction data. This difference can be explained by several assumptions that are made for source terms and most importantly can be related to the assumption, which all the wave stage transferred to next stage of water sheet formation without considering any mass loss at the impact. Another reason for the discrepancy between the results of experimental and theoretical models can be discussed as a source of errors regarding the experimental measurements of BIV and PIV methods and based on the assumptions that were used to simplify the governing equations. Moreover, the diameter and distribution of droplets were measured on a particular one-dimensional plane in front of the model, and the presence of droplets in three dimensional was not considered.

Further, the results of theoretical and experimental droplet velocity distribution for an experimental model for three different wave phase velocities are shown in Fig. (6-30). As is evident from these figures, the predicted model underpredicts the velocity distribution. This discrepancy can be discussed based on all the previously mentioned differences and assumptions between experimental and theoretical models. Furthermore, the aerodynamic drag force can have a significant influence on droplet velocity over a tremendously short distance, which makes it very difficult in DPIV method to steadily measure the droplet velocities. Based on this transient behavior of droplets, three different short distances of droplet time life were picked, and the droplet velocities were measured based on the averaging over all these distances. In addition, droplets from the moment of breakup tend to oscillate, and they are mostly non-spherical, these two factors affect their velocities and lead to increase in drag.

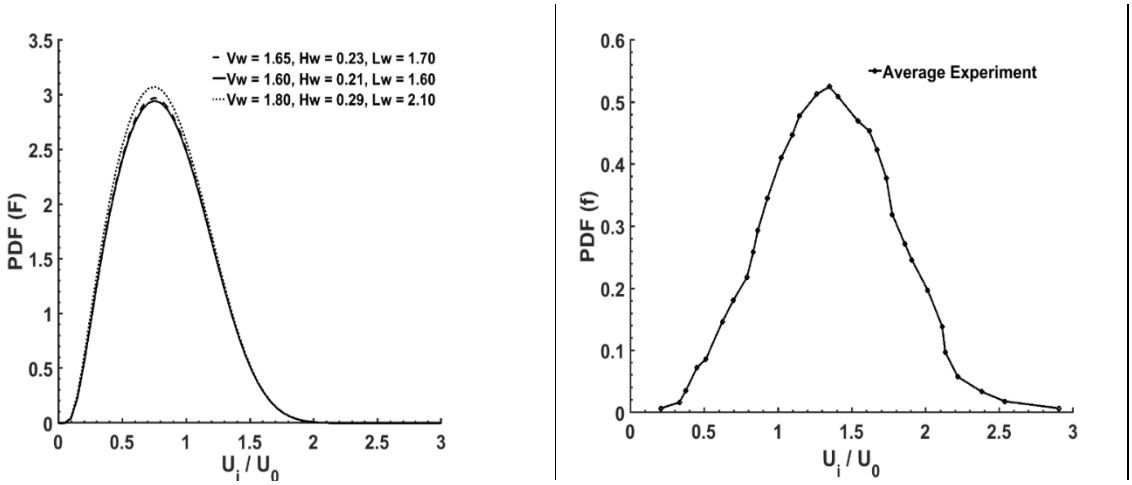

Fig. 6-30 Droplet velocity distributions for three different wave characteristics: a) Theoretical prediction model, b) Experimental model (Average of all three different wave characteristics).

A joint droplet size and velocity distribution is shown as discrete sequence data in Fig. (6-31). In most of the trial cases, the mean droplet size and velocity are nearly constant for large size droplets, in which they are not affected by drag force. Although this figure clearly shows the droplet size and velocity distributions, it is not suitable for comparing with the theoretical model.

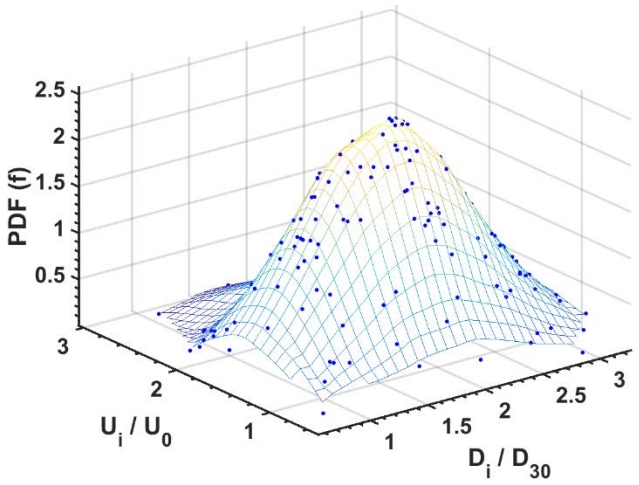

Fig. 6-31 A joint droplet size and velocity distribution for a sample spray arising from a wave impact.

Figure (6-32) shows a comparison between the current 2-dimensional theoretical MEP method and the 1-dimensional model as well as the experimental model, for a single wave with characteristics $V_w = 1.80\ m/s, A_w = 140\ mm$, and $L_w = 2.10\ m$ for the flat plate model. As the graph indicates the discrepancy between the 2-D and experimental model is very little and is less than 15% in comparison with the 1-D model.

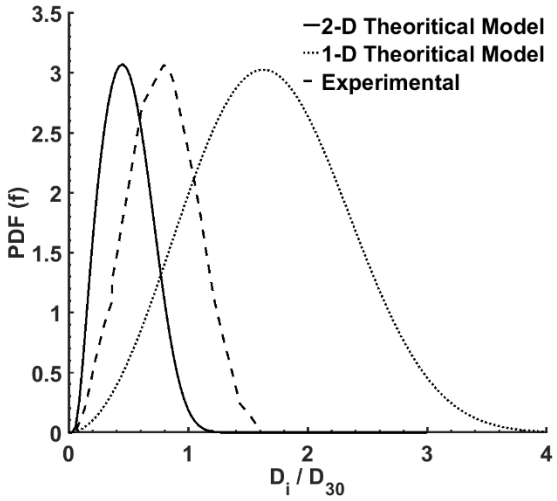

Fig. 6-32 A comparison between 1-D and 2-D theoretical MEP method and the experimental model for the lab-scaled flat plate model.

The theoretical model is applied to a large-scale data set reported by Ryerson, 1995 to evaluate the droplet size and velocity distributions for four different wave phase velocities (Fig. 6-33). From these figures, it can be concluded that higher wave phase velocities (inlet velocity) lead to a smaller range of droplet diameters and a sharper distribution. As previously mentioned, all the measured and predicted distributions show the same characteristics and the effect of drag force on small droplets, pushing them to lower velocities. However, large and medium-size droplets tend to keep their velocities but the effect of gravity on large droplet sizes should be further studied in future work.

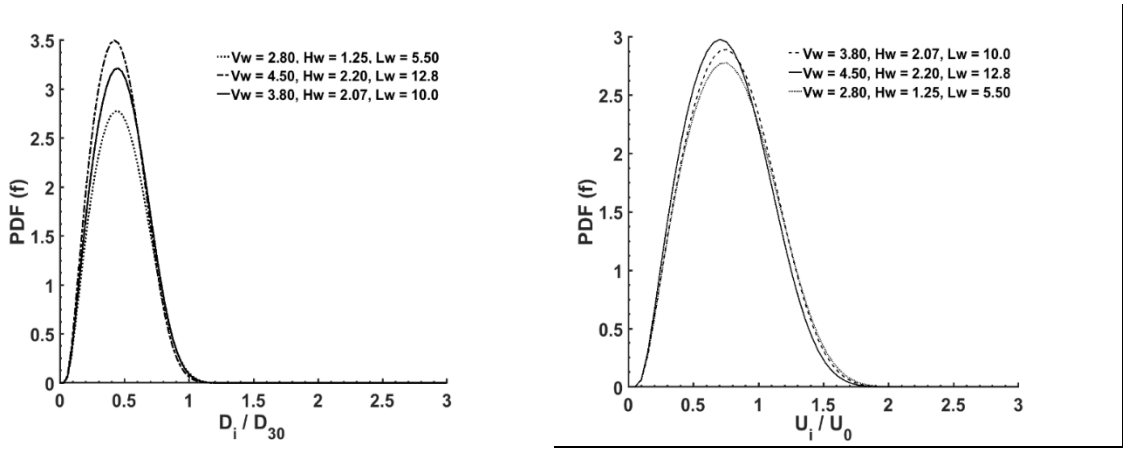

Fig. 6-33 Droplet size and velocity distribution based on the reported wave data by Ryerson, 1990 for four different wave characteristics.

6.3.3 MEP Sensitivity Analysis

All of the parameters that are represented before in the mathematical formulations are physically meaningful. The effect of several parameters such as the partition coefficient K_p, the kinetic energy source term $\bar{S}_{ke}$, and the D_{30}/D_{32} ratio for the surface energy constraint on the probability size distribution were investigated. Some of these parameters cannot be obtained from an examination of the liquid sheet and can only be obtained directly from the knowledge of spray. Fig. (6.34) shows the sensitivity analysis regarding the kinetic energy source term $\bar{S}_{ke}$, which is a correction for the sheet model. This parameter is directly related to the breakup process and acts to increase the distribution of velocity. A positive value of this source term leads to higher variance of velocity in comparison with zero or negative values.

Broadness of the droplet size distributions depends directly on the partition coefficient K_p and the D_{30}/D_{32} ratio for the surface energy constraint. Sensitivity analysis

of both parameters suggests that having both their values close to unity leads to narrower size distributions and they are not responsible for larger droplet size distributions. Figure (6-35) shows the study of both the partition coefficient and the D_{30}/D_{32} ratio.

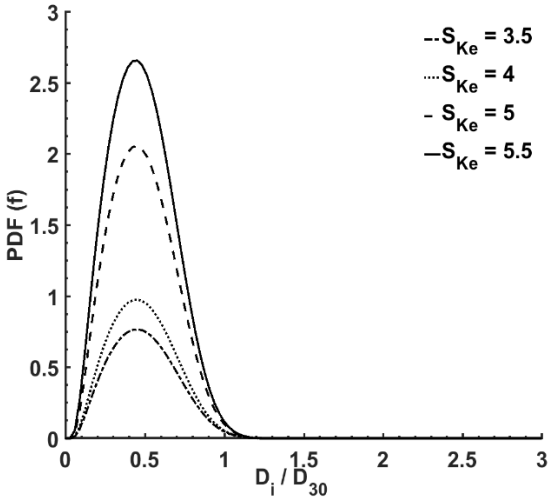

Fig. 6-34 Sensitivity analysis of the kinetic energy source term $\bar{S}_{ke}$.

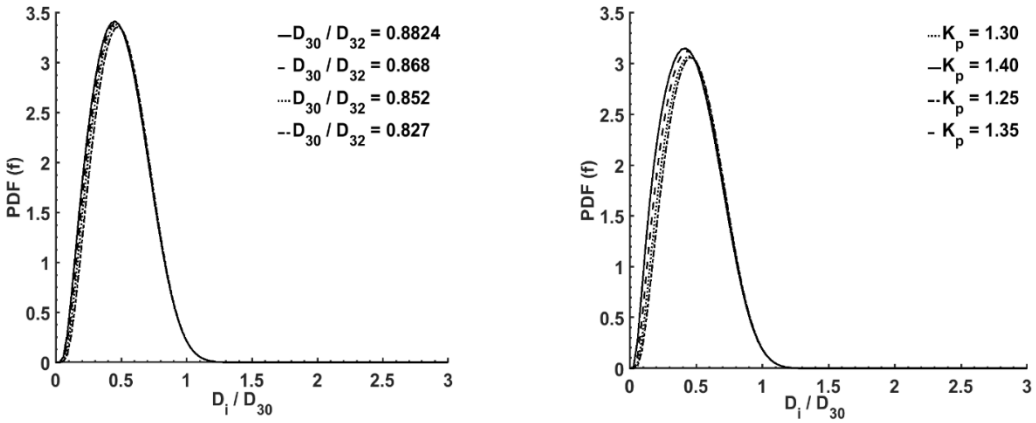

Fig. 6-35 Sensitivity analysis of the partition coefficient K_p and the D_{30}/D_{32} ratio for the surface energy constraint.

6.4 Analytical Approach Results

In this section, an analytical model to predict the final average droplet size within a spray cloud that is formed due to wave interactions with marine objects is introduced. The prediction model is compared with experimental measurements from the previously mentioned experiments. The effects of initial wave characteristics, the geometrical parameters of the impact condition and the water sheet thickness at the moment of impact, on the final average droplet diameter were investigated. A sensitivity analysis of most of the principal parameters was performed to show the high veracity of the prediction model.

The series of equations involving; wave input characteristics (Eqs. 5-1, 5-2 and 5-5, 5-6), maximum impact pressure considering the air entrapment pressure (Eqs. 5-8 and 5-9), the relation between maximum impact pressure and maximum wave run-up velocity (Eq. 5-10), and lastly, Eq. (5-11) and (5-12) representing the final average droplet and ligament diameter, leads to the creation of a comprehensive analytical model that predicts spray characteristics from the input wave characteristics. The effects of significant parameters on the final average droplet diameter have been investigated, and results from the prediction model are compared with the results of the experimental model.

Figure (6-36) shows the effect of various wave characteristic such as wave amplitude ξ_a and wavelength L_w on the final average droplet diameter. As this figure shows, increasing the wave amplitude and reducing the wavelength, which makes the input wave steeper and increases the wave phase velocity, thus reducing the droplet final average

diameter. This can be explained by the water sheet instability phenomena. As the rising water sheet velocity increases, the instability growth rate also increases, which leads to a smaller droplet diameter. Fig. (6-36) indicates that the final average droplet diameter for most input wave characteristics varies between 400 – 850 micrometers.

In addition to the wave characteristic parameters, the rising water sheet characteristics and the wave impact width at the moment of impact are important in predicting the final average droplet diameter. Figure (6-37) shows the dependency of the final average droplet diameter on these two parameters. Two wave characteristics were chosen as input wave characteristics for calculation of final average droplet diameter based on the variation of water sheet thickness τ_n and wave impact width W.

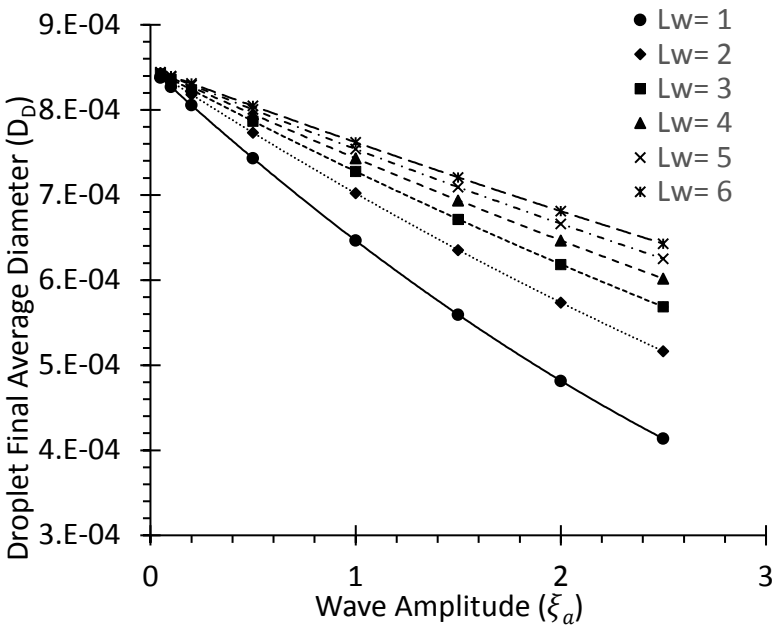

Fig. 6-36 Final average droplet diameter variation based on variation of input wave data characteristics

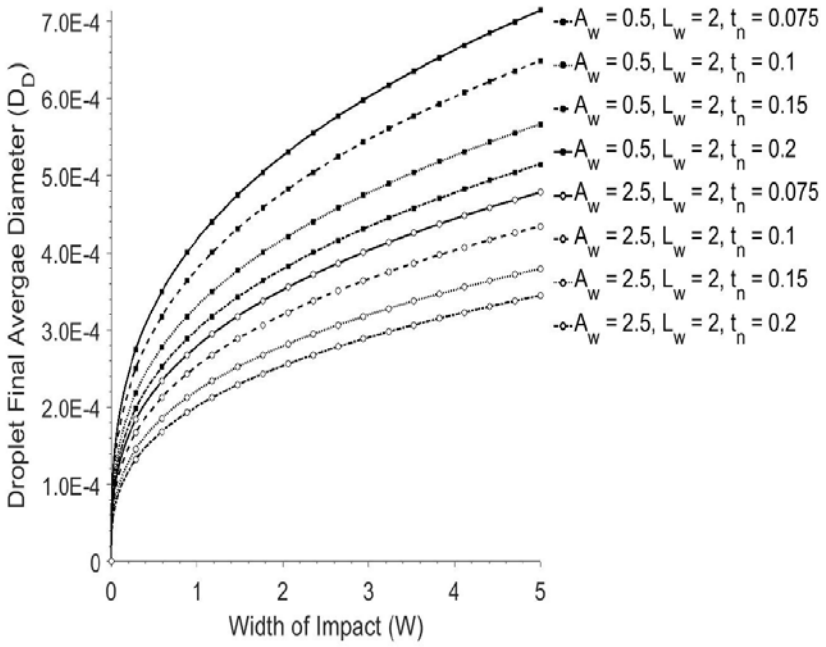

Fig. 6-37 Final average droplet diameter variation based on variation of water sheet thickness ($\tau_n = 0.075, 0.1, 0.15, 0.2$) and width of wave impact for two different wave amplitude $A_w = 0.5, 2.5$.

As Fig. (6-37) shows, the final average droplet diameter reduces as the water run-up sheet thickness increases. This indicates that the higher kinetic energy with higher wave phase velocity leads to an increase in instabilities inside the ligaments and water sheet, which generates smaller droplets. The effect of using both wave models on final average droplet diameter for one case study is shown in Fig. (6-38). As this figure indicates, the difference between the first order harmonic wave theory and the second-order Stokes wave theory is less than 3% in terms of droplet diameter, with the difference increasing as the width of impact increases.

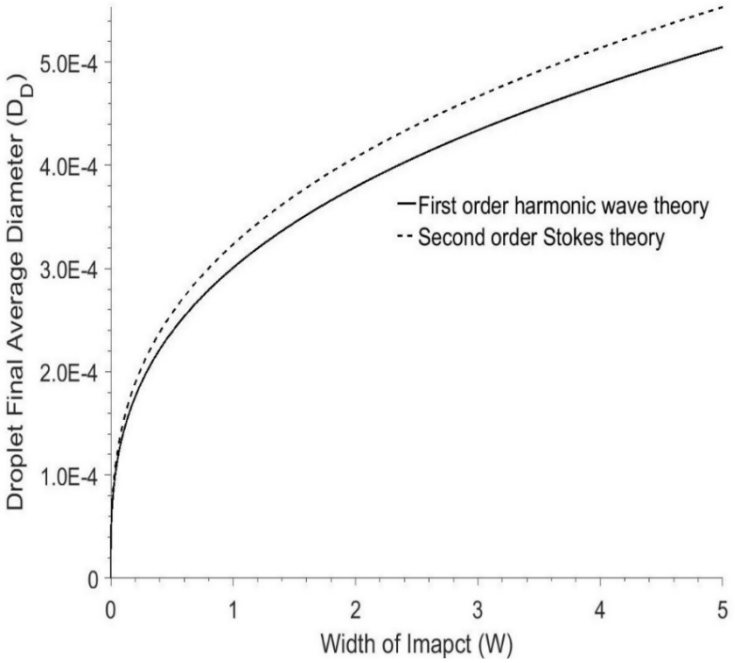

Fig. 6-38 Comparison between considering different wave theories (First-order harmonic wave theory and second-order Stokes theory) as an input wave characteristics.

Another factor in an estimation of final average droplet diameter is the spray parameter K, which is calculated as $K = C\tau_n W$. This spray parameter is a multiplication of both water sheet thickness and the width of wave impact. It is clear from Fig. (6-39) that an increase in wave maximum run-up velocity leads to smaller final average droplet diameter. In conditions where maximum wave run-up velocity is higher than $10\ m/s$ (real scale conditions), the spray parameter is not a significant parameter; however, it does become significant in cases with low maximum wave run-up velocity.

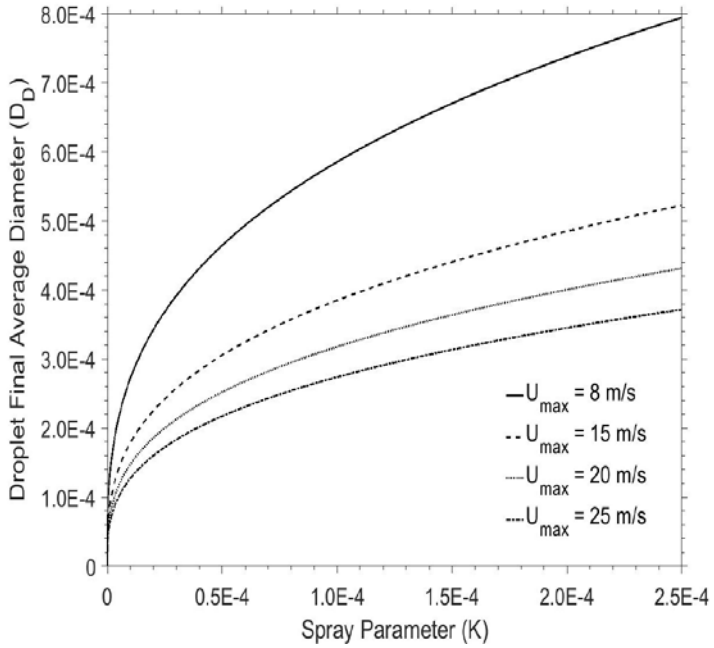

Fig. 6-39 Effect of maximum wave run-up velocity U_{max} and spray parameter K on the final average droplet diameter.

Some other variables, which affect the final average droplet diameter, and are calculated either based on empirical formulations or extracted from experimental data, are used to perform a further sensitivity analysis. The first variable of interest is the impact coefficient c_i, which appears in Eq. (5-10). This coefficient relates the maximum impact pressure to the maximum wave run-up velocity. Figure (6-40) shows the effect of the impact coefficient on final average droplet diameter for four different maximum impact pressures. As shown in this figure, higher impact pressure leads to smaller final average droplet diameter and the variation of impact coefficient is less significant in terms of the droplet diameter. However, for lower impact pressure, the final average droplet diameter increases and the effect of impact coefficient is more significant, and causes the final average droplet diameter to vary from 500 to 900 micrometres.

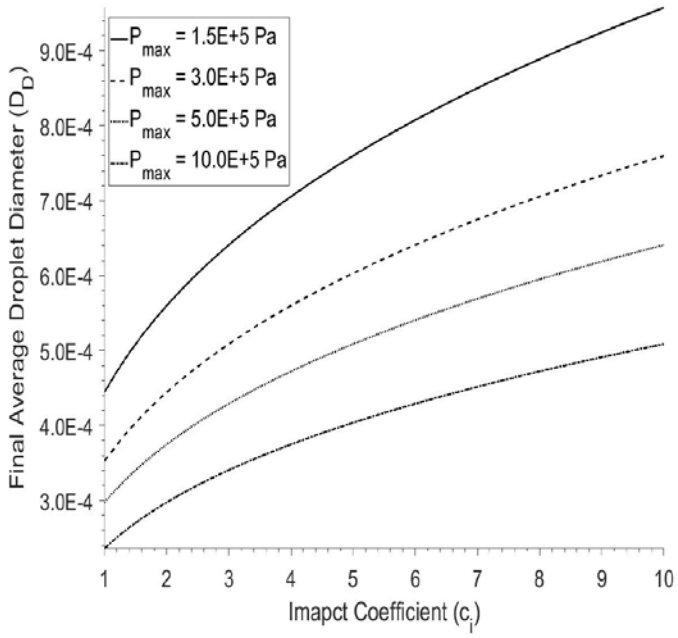

Fig. 6-40 Effect of impact coefficient c_i on the final average droplet diameter for four different maximum impact pressure p_{max}.

The remaining variables such as fluid properties (ρ_w, μ, σ) and the ratio of air pocket diameter to the diameter of water enclosing the air have negligible effects on the final average droplet diameter.

Results from the prediction model are compared with results extracted from the experiment. Figures (6-41) and (6-42) demonstrate the comparison between the average final droplet diameter of several trials of experiment and the final average droplet diameter from the prediction model for the flat-shaped plate and bow-shaped models, respectively. For the experimental data, three average values of maximum, average, and minimum of all trials are shown in four different case studies and, the comparison indicates a satisfactory agreement.

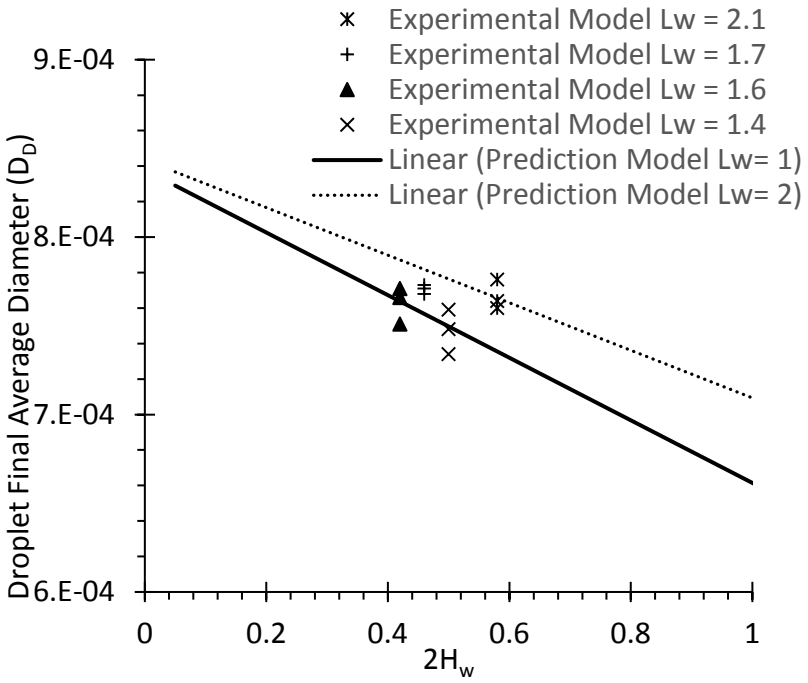

Fig. 6-41 A comparison of results between experimental data and prediction model for four different case studies in flat plate model.

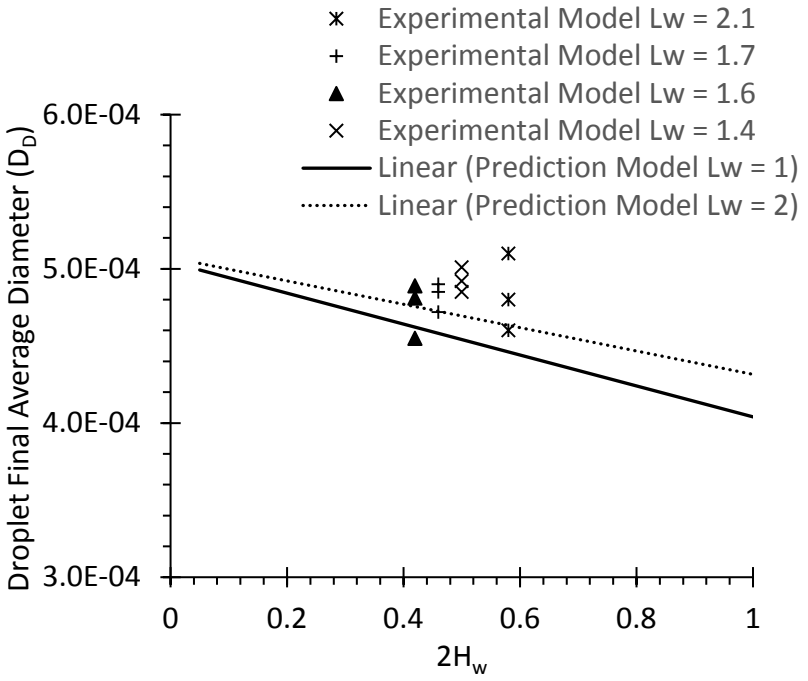

Fig. 6-42 A comparison of results between experimental data and prediction model for four different case studies in bow shaped model.

Figures (6-41) and (6-42), show that the prediction model for flat-shaped plate model predicts well in comparison with the experimental results and the differences reach a maximum of 10% of the final average droplet diameter. However, for the bow-shaped model the prediction model underpredicts the final average droplet diameter. As Fig. (6-41) shows, the experimental average of final average droplet diameter fall above the prediction lines with a maximum discrepancy of 18%. This can be related to the errors associated with measuring the droplet sizes in the experiment in which errors related to measuring the droplet size increase as the droplet sizes decrease.

Conclusions

The focus of this thesis is on developing and linking simulations of the complex individual process, identified as; wave slamming, free surface modeling, air entrainment, and sheet breakup, in order to increase the knowledge of the steps in the wave spray phenomena and develop an overall predictor of spray cloud characteristics. In the first chapter, existing field observations involved in the study of the LWC and spray height are reviewed. This shows a need for more observations with better and accurate measurements of the variables of spray clouds, such as droplet velocities, sizes, and locations. Full-scale measurements are useful in studying the process. Early measurements illustrated the importance of spray cloud formation, but these measured data were not sufficiently detailed to be used to validate the computational results or lab scale experimental data.

Next, research regarding the numerical, analytical and experimental studies and several methods of wave ship impact simulation were reviewed. Studies directly related to modeling the spray cloud that occurs upstream of a ship bow are limited in the literature, and most of the studies are focused on the wave impact pressure. It is concluded that the full direct numerical simulation of wave-ship interaction for the generation of spray clouds is not a viable option at this time, but the stages of this process can be modeled separately. However, even these separate process involved in spray cloud formation could be further developed. Even predicting and modeling wave slamming behavior with the bow is a complex problem. Phenomena, such as air entrainment,

compressibility effects, and predicting full-scale values from scaled experiments remain to be better developed.

The experimental and/or numerical methods associated with the particular parts of the wave spray process, such as wave-slamming, free surface capturing, and turbulence models are reviewed in the remaining section of this chapter. Some of these individual phenomena have specific solutions and corresponding lab experiments, but some were reviewed because of the similarity of the solutions. These similar methods and studies are suggested for adaptation to the present problem. The future of numerical prediction in this field is in CFD. However, the multi-scale nature of this problem makes calculation computationally expensive. The power and memory capability of new multi-processor computers makes modeling the phenomena possible; however, it still takes days to simulate the prediction of wave slamming incidents, droplet breakup, and a turbulence model with small computational cells in the domain.

The review shows the current trends in modeling and analyzing spray cloud formation arising from wave impact with objects at the sea surface in cold regions, which leads to icing on vessels and offshore structures. More precise considerations will be needed in studying each of these parts, which can then be built into an overall model. The present gaps in this field have been highlighted, and several appropriate methods and solutions were implemented in this thesis to increase the accuracy of prediction models in this field.

In the second chapter, the interaction of a flat-shaped plate and bow-shaped model with plunging breaking waves was carried out in a laboratory tow tank. As the interaction

proceeded, the water flow experienced several stages. First, a water sheet was produced, followed by its breaking up into droplets, and finally, a spray cloud. BIV and DPIV techniques were used to observe these behaviors during spray formation qualitatively. The DPIV results were used to develop a relationship between wave characteristics, pressure, and droplet velocities for three size ranges.

The results of the experiment showed that the highly transient process of spray formation causes a significant velocity difference between droplets that are immediately formed after a breakup and droplets that are located at a middle distance from the maximum spray height. The influence of drag force on smaller droplets, the influence of gravitational force on larger droplets, and the influence of both forces on medium droplets are predicted to be the most significant factors. Two regions above the impact area were considered for velocity measurements: one immediately above the impact area (FOV1), which contains the sheet breakup, and the other at the midway distance from the droplets' maximum height (FOV2). A reduction in velocity in these two areas is significant for both small and large droplets, but a decrease in velocity for medium droplets in these two regions, when they are compared to other droplet size classes, is not significant. This shows that the velocity of medium droplets remains nearly constant and that these droplets reached greater heights (FOV2 area) compared with other size droplets.

Another result of the experiment indicates that higher wave phase velocities ($1.5 < \mathrm{V_c} < 2.3\ \mathrm{m/s}$) produce higher impact pressure ($1.8 < \mathrm{P} < 2.5\ \mathrm{kPa}$). For instances for the case of $\mathrm{V_c} = 1.6$, this pressure leads to a higher velocity water sheet,

approximately $7\ \mathrm{m/s}$ or $4.40\mathrm{V_c}\ (\mathrm{m/s})$, and produces finer droplets. Similarly, a higher wave height creates higher impact pressure in both models. Wave impacts occurring at the moment of wave crest overturning increase the amount of spray and build an enormous impact pressure $(\mathrm{P} = 3\ \mathrm{kPa})$. This type of effect leads to a higher velocity sheet and finer droplets, which reach about $2\ \mathrm{m}$ above the tip of the model. Pressure measurements were performed for all trials in both models. The results of pressure measurements show that an increase in wave height and wave phase velocities both lead to an increase in pressure with increasing linear trends. An increase in wave heights $(0.2 - 0.3\ \mathrm{m})$ leads to higher pressure on flat-shaped plate model.

The qualitative results from both side and front views are similar, and the maximum velocity measured from both views is about $8\ \mathrm{m/s}$ or $4.40 \cdot \mathrm{V_c}\ (\mathrm{m/s})$, which was reported for small droplets $(300 - 700\ \mu\mathrm{m})$. Without the presence of airflow on top of the model, the direction of the spray flow pattern is observed as a triangular shape: one edge of the triangle is vertically parallel and attached to the object, and the other edge is vertical with an angle of 30 to 40 degrees with respect to the object.

In the later chapter, a three-dimensional coupled VOF and LSM is used to simulate deep water wave impact with an object and to investigate the behavior of wave impact at the moment of impact including the breakup length of arising water sheet. The numerical method provides results that are comparable with experimental results. However, due to a limitation in the size of the numerical mesh, some spray characteristics, such as droplet sizes and velocities in the spray cloud cannot be simulated. However, the numerical model

provides reasonable results for the velocity field of the water sheet in front of the model up to the stage that jet breakup occurs. The results of jet acceleration in front of the model are well matched with the results observed from the experiment.

Comprehensive mesh refinement was implemented to capture the behavior of the free surface near the model and to pick the best mesh sizes for precise prediction near the boundaries.

The length of water sheet breakup from the moment of wave impact has been measured experimentally and predicted numerically. These results are compared with an analytical model from linear stability analysis and good agreement between the results is achieved. The results predict that an increase in the Weber number of the water sheet leads to a decrease in breakup length. This behavior demonstrates that with higher sheet velocity the disturbances in the sheet flow grow faster, which destabilizes the water sheet earlier.

Pressure measurement was performed experimentally and predicted numerically, and comparison shows satisfactory agreement. The three types flow behavior, spray generation, water sheet formation, and both together are observed during the experiment for different wave phase velocities. The numerical simulation for similar wave inlet boundary conditions at different wave phase velocity at the moment of impact, predicts these types of flow behaviors, and the results agree well with the experimental data.

In chapter four, a predictive model for droplet size and velocity distributions within sprays at different stages of a breakup during wave impact has been introduced. The MEP method is applied to the problem of wave impact with a marine object for both lab scale models and full-scale impacts. This method is shown to be suitable for applications in which thermodynamic equilibrium accurately predicts droplet size and velocity distribution. The discrepancies between this prediction method and the results from the experiment can be attributed to previous assumptions that simplify the predictive model. The effects of horizontal velocity, gravity force, slamming force and turbulence is not currently considered in the predictive model. However, the results of the experiment and prediction model are in reasonable agreement with each other. The results of probability density functions between the predicted and experimental models have approximately 5% difference. However results of droplet size prediction have 15% differences, which is due to the experimental errors, uncertainties, and several assumptions that have been made in the governing equations.

The set of governing equations are iteratively solved using a modified Newton-Raphson method to yield the unknown Lagrangian multipliers. The governing equations and their derivatives have an integral and exponential form, which leads to convergence difficulties in calculating a solution. Although unique solutions for the equations are available, these solutions are highly sensitive to the initial values of Lagrange multipliers $(\lambda_0, \lambda_1, \lambda_2, \lambda_4)$. Reasonable initial guesses in this procedure can lead to faster convergence.

This procedure is applied to both primary regions of a breakup, first from the impact moment to the water sheet breakup, and second, from the moment of impact to the downstream of spray and droplet formation regions. Two models of drag forces were added to the momentum source term. The first model considered only the effect of drag force on the water sheet, and the second model was considered for the drag force on the droplets in the secondary region. The effect of the initial sheet velocity on the droplet size distribution was investigated, and the results show that an increase in the initial velocities can lead to narrower distribution along specific droplet sizes, and an increase in the peaks of distribution.

Futher, in this chapter, a 2-D analytical approach based on the MEP to predict the droplet size and velocity distributions of wave spray was introduced. The model considers the transition stages of wave impact, water sheet breakup, and spray formation. This model predicts consistent quantitative results of both droplet size and velocity distributions in a spray. Both droplet size and droplet velocity distributions show the same characteristics as the experimental data represents.

Further, the prediction model is in a satisfactory agreement (less than 20% discrepancy) with the experimental results that are collected with the DPIV technique from the spray production due to wave impact with a lab-scaled flat-shaped plate model. Moreover, the model prediction was applied to the large scale input data that are available at references for four different wave characteristics, which shows satisfactory results when it compared with the rough data that are presented in several articles.

Furthermore, the sensitivity analysis was performed to discuss the effect of each physical parameters on the given model.

As the scale of spray in front of the real scale marine objects is very complicated and chaotic, it is unnecessary and unreasonable to describe the processes of spray formation for each individual droplet. Only the overall quantities and their overall distributions can be significant. Furthermore, previous studies related to spray formation associated with wave spray were considered mono -size and –velocity assumptions for droplets and this current model can lead to better analysis of spray.

In this model concept, the effect of the inlet velocity profile, horizontal velocity, fluid phases properties, and the Weber number are significant in applying this model to various conditions. Weber number dependency requires the pre-estimation of the mass mean diameter of the spray, which indicates that a rough estimate of this value is crucial for finding the distribution of droplet sizes and velocities for modeling various types of spray.

Lastly, an analytical model to predict the final average droplet diameter of wave spray due to wave impact with an object is introduced. This model includes the effect of air compressibility during the air entrapment process of wave impact and relates the maximum wave impact pressure to the maximum wave run-up velocity. Further, the model considers the liquid water sheet disintegration and breakup, which relates the wave run-up maximum velocity to the final average droplet diameter. In general, this model predicts the final average droplet diameter by inputting wave characteristics to the

model and considering the physics of wave impact, wave entrapment, and water sheet breakup.

Results from the prediction model are compared with results measured from an experimental simulation. The experiments measured final average droplet diameter of a cloud of spray due to wave impact at lab-scale for two different bow-shaped and flat-shaped models using several image velocimetry techniques. The comparison between the experimental simulation and prediction model are in good agreement with the maximum of 10% discrepancy for the flat plate model and 18% for the bow-shaped plate model.

Effects of several parameters such as input wave characteristics (wavelength and amplitude), spray parameter K, impact coefficient C_i, and the parameters which depend on the geometry of impact, width of impact W and water sheet thickness t_n are studied and assessed for significance in terms of the final droplet diameter. Similarly, the effect of wave impact maximum pressure P_{max} due to the effect of air entrainment and wave run-up maximum velocity U_{max} was considered in terms of significance on the final average droplet diameter. In both cases the significance of the studied effects on the droplet diameter was found to be influenced by the wave velocity and resulting maximum pressure.

References

Abrahamsen, B.C., Faltinsen, O.M., 2013. “Scaling of entrapped gas pocket slamming event at dissimilar Euler number.” J. of Fluids and Structures, 40, 246-256.

Airy, G. B. (1845). "Tides and waves," Encyclopedia. Metropolitana, 5, Art. 525-528, London.

Altieri, A., Cryer, S. A., Acharya, L., 2014, “Mechanisms, experiment, and theory of liquid sheet breakup and drop size from agricultural nozzles,” Journal of Atomization and Sprays, V. 24 (8), pp. 695-721.

ANSYS Fluent 12.0 User’s Guide, Copyright by ANSYS, Inc, (2009).

Ariyarathne, K., Chang, K-A., Mercier, R., 2012. “Green water impact pressure on a three-dimensional model structure.” Exp. Fluids. 53, 1879-1894.

Ashcroft, J., 1985. Potential Ice and Snow Accretion on North Sea Rigs and Platforms. Marine Technical Note No. 1. British Meteorological Office, Bracknell.

Ashgriz, N., Poo, J.Y., 1991. FLAIR: flux line segment model for advection and interface reconstruction. J. Comput. Phys. 92, 449–468.

Bagnold, R. A., 1939, “Interim report on wave-pressure research,” Proc. Inst. Civ. Engrs. Vol. 12, pp. 201-226.

Bhattacharyya, R., 1978. “Dynamics of Marine Vehicles.” Ocean Engineering, John Wiley, and Sons, NY.

Bilanin, A. J., 1991, “Proposed Modification to Ice Accretion/Icing Scaling Theory,” Continuum Dynamics, Inc. Vol. 28, No. 6, Princeton, New Jersey 08543.

Blackmore, P.A., Hewson, P.J., 1984, “Experiments on full-scale wave impact pressures,” Coastal Eng., Vol. 8, pp. 331-346.

Bodaghkhani, A., Dehghani, S.R., Muzychka, S.Y., Colbourne, B., 2016. Understanding spray cloud formation by wave impact on marine objects. Cold Regions Science and Technology, 192, 114-136.

Bodaghkhani, A., Muzychka, Y.S., Colbourne, B., 2017. A scaling model for droplet characteristics in a spray cloud arising from wave interactions with marine objects. In: ASME. International Conference on Offshore Mechanics and Arctic Engineering. Ocean Engineering Vol. 7A (V07AT06A050).

Bogaert, H., Leonard, S., Brosset, L., Kaminski, M., 2010. “Sloshing and scaling: results from Sloshel project.” Proceedings of 20th International Offshore and Polar Engineering Conference, June 20-26 2010, Beijing, China.

Borisenkov, Y.P., Panov, V., 1972. Basic Results and Prospects of Research on Hydro meteorological Conditions of Shipboard Icing, from Issled. Fiz. Prir. Obledeneniya, Leningrad. CRREL. Draft Translation TL411, 1974.

Borisenkov, Y.P., Pchelko, I.G., 1975. Indicators for Forecasting Ship Icing. USACRREL Draft Translation. No. 481.

Borue, V., Orszag, S.A., Staroselsky, I., 1995. Interaction of surface waves with turbulence: direct numerical simulations of turbulent open-channel flow. Journal of Fluid Mechanics 286, 1–23.

Bradford, S.F., 2000. Numerical simulation of surf zone dynamics. J. Waterw. Port Coast. Ocean Eng. 126 (1), 1–13.

Bredmose, H., Peregrine, D.H., Bullock, G.N., 2009. “Violent breaking wave impacts. Part 2: modeling the effect of air”. J. Fluid Mech, 641: 389-430.

Bredmose, H., Bullock, G. N., Hogg, A. J., 2015, “Violent breaking wave impacts. Part 3. Effects of scale and aeration”, J. Fluid Mech., Vol. 765, pp. 82-113.
Brocchini, M., Peregrine, D.H., 2001a. The Dynamics of Strong Turbulence at Free Surfaces. Part 1. Description, J. Fluid Mech 449, 225–254.
Brocchini, M., Peregrine, D.H., 2001b. The Dynamics of Strong Turbulence at Free Surfaces. Part 2. Free Surface Boundary Conditions, J. Fluid Mech 449, 255–290.
Brosset, L., Mravak, Z., Kaminski,M., Collins, S., Finnigan, T., 2009. Overview of Sloshel Project. Proceedings of the Nineteenth International Offshore and Polar Engineering Conference, Osaka, Japan, June 21–26.
Brown, R.D., Roebber, P., 1985. The scope of the ice accretion problem in Canadian waters related to offshore energy and transportation. Canadian Climate Centre Report 85–13 unpublished manuscript, 295 pp.
Brucker, K.A., O'Shea, T.T., Dommermuth, D., 2010. Numerical Simulations of Breaking Waves—Weak Spilling to Strong Plunging. Proc. of the 28th Symp. On Naval Hydrodynamics, Pasadena, CA.
Bullock, G. N., Crawford, A. R., Hewson, P. J., Wlakden, M. J. A., Bird, P. A. D., 2001, “The influence of air and scale on wave impact pressures,” Coast. Eng. Vol. 42, pp. 291-312.
Bullock, G.N., Obhrai, C., Peregrine, D.H., Bredmose, H., 2007. Violent breaking wave impacts. Part 1: results from large-scale regular wave tests on vertical and sloping walls. Coast. Eng. 54 (8), 602–617.
Cao, X.K., Sun, Z.G., Li, W.F., Liu, H.F., Yu, Z.H., 2007. A new breakup regime of liquid drops identified in a continuous and uniform air jet flow. Phys. Fluids 19, 057103.
Carrica, P.M., Drew, D., Bonetto, F., Lahey Jr., R.T., 1999. A polydisperse model for bubbly two-phase flow around a surface ship. Int. J. Multiphase Flow 25, 257–305.
Carrica, P.M., Wilson, R.V., Stern, F., 2005. An Unsteady Single-Phase Level Set Method for Viscous Free Surface Flows. IIHR Technical Report No. 444, Iowa City IA 52242–1585 USA.
Chan, E.S., Melville, W.K., 1984. Breaking wave forces on surface-piercing structures. In: Oceans '84, Washington, D.C. pp. 565–570.
Chan, E.S., Melville, W.K., 1987. Plunging wave forces on surface-piercing structures. In: Proc. 6th Intl. Offshore Mech. and Arctic Eng. Symposium. vol. 2. ASME, Houston, TX, pp. 61–72.
Chan, E.S., Melville, W.K., 1988. Deep-water plunging wave pressures on a vertical plane wall. Proc. R. Soc. Lond. A417, 95–131.
Chan, S., 1994. Mechanism of deep water plunging-wave impacts on vertical structures. Coast. Eng. 22, 115–133.
Chang, K.A., Liu, P.L.F., 1998. Velocity, acceleration and vorticity under a breaking wave. Phys. Fluids 10, 327–329.
Chang, K.A., Liu, P.L.F., 1999. Experimental investigation of turbulence generated by breaking waves in water of intermediate depth. Phys. Fluids 11, 3390–3400.
Chang, K.A., Liu, P.L.F., 2000. Pseudo turbulence in PIV breaking-wave measurements. Exp. Fluids 29, 331–338.
Chang, K.A., Lim, H.J., Su, C.B., 2003. Fiber optic reflectometer for velocity and fraction ratio measurements in multiphase flows. Rev. Sci. Instrum. 74, 3559–3565.
Chang, K.A., Ariyarathne, K., Mercier, R., 2011. Three-dimensional green water velocity on a model structure. Exp. Fluids 51 (2), 327–345.
Colagrossi, A., Lugni, C., Brocchini, M., 2010. A study of violent sloshing wave impacts using an improved SPH method. J. Hydraul. Res. 48 (S1), 94–104.

Chorin A. J., "Numerical solution of Navier-Stokes equations." Mathematics of Computation. 22. 745–762, (1968).

Chorin, A.J., 1980. Flame advection and propagation algorithms. J. Comput. Phys. 35, 1–11.

Christensen, E.D., Deigaard, R., 2001. Large eddy simulation of breaking waves. Coastal Engineering 42, 53–86.

Chuang, W.L., Chang, K.A., Mercier, R., 2015. Green water velocity due to breaking wave impingement on a tension leg platform. Exp. Fluids 56, 139.

Chung, K.K., Lozowski, E.P., 1998. A three-dimensional time-dependent icing for a stern trawler. J. Ship Res. 42, 266–273.

Chung, K.K., Lozowski, E.P., 1999. A three-dimensional time-dependent icing model for a stern trawler. J. Ship Res. 42, 266–273.

Cuomo, G., Allsop, W., Bruce, T., Pearson, J., 2010a, "Breaking wave loads at vertical seawalls and breakwaters," Coast. Eng., Vol. 57, pp. 424-439.

Cuomo, G., Allsop, W., Takahashi, S., 2010b, "Scaling wave impact pressures on vertical walls," Coast. Eng., Vol. 57, pp. 604–609.

Cura Hochbaum, A., Shumann, C., 1999. Free Surface Viscous Flow around Ship Models. 7th Int. Conf. Numerical Ship Hydrodynamics, Nantes, France.

Dehghani, S.R., Muzychka, Y.S., Naterer, G.F., 2016a. Droplet trajectories of wave-impact sea-spray on a marine vessel. Cold Reg. Sci. Technol. 127, 1-9.

Dehghani, S.R., Naterer, G.F., 2016b. Droplet size and velocity distributions of wave-impact sea-spray over a marine vessel. Cold Reg. Sci. Technol. 132, 60-67.

Dehghani-Sanij, A.R., Dehghani, S. R., Naterer, G.F., Muzychka, Y. S., 2017b. "Marine Icing Phenomena on Vessels and Offshore Structures: Prediction and Analysis," Ocean Engineering, Vol. 143, pp. 1-23.

Dehghani-Sanij, A.R., Dehghani, S. R., Naterer, G.F., Muzychka, Y. S., 2017a. "Sea Spray Icing Phenomena on Marine Vessels and Offshore Structures: Review and Formulation." Ocean Engineering, Vol. 132, pp. 25-39.

Derakhti, M., Kirby, J.T., "Bubble entrainment and liquid-bubble interaction under unsteady breaking waves," J. Fluid Mech. 761, 464-506, (2014).

Di Mascio, A., Broglia, R., Muscari, R., 2004. A Single-Phase Level Set Method for Solving Viscous Free Surface Flows. Submitted to Int. J. Num. Meth. Fluids.

Ding, Z., Ren, B., Wang, Y., Ren, X., 2008. Experimental study of unidirectional irregular wave slamming on the three-dimensional structure in the splash zone. Ocean Eng. 36 (16), 1637–1646.

Dombrowski, N., Johns, W. R., 1963, "The aerodynamic instability and disintegration of viscous liquid sheets," Chem. Eng. Sci., Vol. 18, pp. 203–214.

Dommermuth, D.G., O'Shea, T.T., Wyatt, D.C., Sussman, M., Weymouth, G.D., Yue, D.K., Adams, P., Hand, R., 2006. The Numerical Simulation of Ship Waves Using Cartesian-grid and Volume-of-fluid Methods. Proc. of the 26th Symposium on Naval Hydrodynamics, Rome, Italy.

Dommermuth, D.G., O'Shea, T.T., Wyatt, D.C., Ratcliffe, T., Weymouth, G.D., Hendrikson, K.L., Yue, D.K., Sussman, M., Adams, P., Valenciano, M., 2007. An Application of Cartesian-grid and Volume-of-fluid Methods to Numerical Ship Hydrodynamics. Proceedings of the 9th International Conference on Numerical Ship Hydrodynamics, Ann Arbor, Michigan.

Drazen, D.A., Melville, W.K., Lenain, L., 2008. Inertial scaling of dissipation in unsteady breaking waves. J. Fluid Mech. 611, 307–332.

Enright, D., Fedkiw, R., Ferziger, J., Mitchell, I., 2002. A hybrid particle level set method for improved interface capturing. J. Comput. Phys. 183, 83–116.
Faltinsen, O.M., 2005. Hydrodynamics of High-Speed Marine Vehicles. Cambridge University Press, New York.
Fenton, J. D., "A fifth-order Stokes theory for steady waves," J. Waterway Port Coastal and Ocean Engineering, 111, 216-234, (1985).
Fenton, J. D., "Nonlinear Wave Theories, the Sea, Vol. 9: Ocean Engineering Science," Eds. B. Le Méhauté and D. M. Hanes, Wiley, New York, (1990).
Ferreira, V.G., Mangiavacchi, N., Tome, M.F., Castelo, A., Cuminato, J.A., McKee, S., 2004. Numerical simulation of turbulent free surface flow with two-equation k – Ɛ eddy-viscosity models. Int. J. Numer. Methods Fluids 44, 347–375.
Floryan, J.M., Rasmussen, H., 1989. Numerical methods for viscous flows with moving boundaries. Appl. Mech. Rev. 42, 32341.
Forest, T.W., Lozowski, E.P., Gagnon, R., June 2005. Estimating Marine Icing on Offshore Structures using RIGICE04. IWAIS XI, Montréal.
Fraser, R. P., Eisenklam, P., Dombrowski, N., Hasson, D., 1962, "Drop formation from rapidly moving liquid sheets," AIChE J., Vol. 8, No. 5, pp. 672–680.
Fu, T.C., Ratcliffe, T., O'Shea, T.T., Brucker, K.A., Graham, R.S., Wyatt, D.C., Dommermuth, D.G., 2010. A Comparison of Experimental Measurements and Computational Predictions of a Deep-V Planing Hull. Proceedings of the 28th Symposium on Naval Hydrodynamics, Pasadena, California, USA.
Fullerton, A.M., Fu, T.C., Brewton, S., 2010. A comparison of measured and predicted wave-impact pressures from breaking and non-breaking waves. In: Proc of the 28th International Conference on Naval Hydrodynamics, Pasadena, California.
Fullerton, A. M., Fu, T. C., Ammeen, E., 2009, "Distribution of Wave Impact Forces from Breaking and Non-breaking Waves," Proceedings of the 28th International Conference on Ocean, Offshore, and Arctic Engineering, Honolulu, Hawaii.
Gerrits, J., Veldman, A.E.P., 2000. Numerical Simulation of Coupled Liquid–Solid Dynamics. Proceedings of the ECCOMAS, Barcelona, Spain.
Greco, M., 2001. A Two-dimensional Study of Green-Water Loading Ph. D. Thesis Dept. Marine Hydrodynamics. NTNU, Norway.
Greco, M., Landrini, M., Faltinsen, O.M., 2004. Impact flows and loads on ship-deck structures. J. of Fluids and Structures 19 /3.
Greco, M., Colicchio, G., Faltinsen, M., 2007. Shipping of water on a two-dimensional structure, part 2. J. Fluid Mech. 571, 371–399.
Greco, M., Lugni, C., 2012. 3D seakeeping analysis with water on deck and slamming. Part 1: Numerical solver. J. of Fluids and Structures 33.
Greco, M., Bouscasse, B., Lugni, C., 2012. 3D seakeeping analysis with water on deck and slamming. Part 2: Experiments and physical investigations. J. of Fluids and Structures 33.
Greco, M., Colicchio, G., Lugni, C., Faltinsen, O. M., 2013. "3D domain decomposition for violent wave-ship interaction," International Journal of Numerical methods in engineering, 95:661-684.
Greenhow, M., Vinje, T., Brevig, P., Taylor, J., 1982. A theoretical and experimental study of capsize of Salter's duck in extreme waves. J. Fluid Mech. 118, 221–239.

Greenhow, M., Lin, W.M., 1985. Numerical simulation of non-linear free-surface flows generated by wedge entry and wavemaker motion. Proc. 4 Int. Conf. Num. Ship Hydro. pp. 94–106 Washington.

Guedes Soares, C., Pascoal, R., Antao, E.M., Voogt, A.J., Buchner, B., 2004. An Approach to Calculate the Probability of Wave Impact on an FPSO Bow. Proceedings of the 23st OMAE Conference, ASME, New York, Paper OMAE—51575.

Govender, K., Mocke, G.P., Alport, M.J., 2002. Video-imaged surf zone wave and roller structures and flow fields. J. Geophys. Res. 107, 3072.

Han, J., Tryggvason, G., 2001. Secondary breakup of axisymmetric liquid drops. II. Impulsive acceleration. Phys. Fluids 13, 1554–1565.

Harvie, D.J.E., Fletcher, D.F., 2000. A new volume of fluid advection algorithm: the stream scheme. J. Comput. Phys. 162, 1–32.

Hendrickson, K., Shen, L., Yue, D. K. P., Dommermuth, D. G., Adams, P., 2003. "Simulation of Steep Breaking Waves and Spray Sheets around a Ship: The Last Frontier in Computational Ship Hydrodynamics," User Group Conference, Proceedings, 200-205.

Hirt, C.W.; Nichols, B.D., 1981, "Volume of fluid (VOF) method for the dynamics of free boundaries," Journal of Computational Physics, V. 39 (1), pp. 201–225.

Horjen, I., 2013. Numerical modeling of two-dimensional sea spray icing on vessel mounted cylinders. Cold Reg. Sci. Technol. 93, 20–35.

Horjen, I., Carstens, T., 1990. Numerical Modelling of the Sea Spray Icing on Vessels. Proc. 10th Int. POAC Conf., Lulea, Sweden vol. 3, pp. 694–704.

Horjen, I., Vefsnmo, S., 1984. Mobile platform stability (MOPS) subproject 02-icing. In: MOPS Report No. 15. Norwegian Hydrodynamic Laboratories (STF60 A 284002, 56 pp.).

Horjen, I., Vefsnmo, S., 1985. A Kinematic and Thermodynamic Analysis of Sea Spray (in Norwegian), Offshore Icing—Phase II. STF60 F85014. Norway, Norwegian Hydrodynamic Laboratory (NHL).

Horjen, I., Vefsnmo, S., 1986a. Computer Modelling of Sea Spray Icing on Marine Structures. In: Proc. Symp. On Automation for Safety in Shipping and Offshore Operations, Trondheim. Elsevier, pp. 315–323.

Horjen, I., Vefsnmo, S., 1986b. Calibration of ICEMOD Extension to a Time-dependent Model. Norwegian Hydrodynamic Laboratories Report STF60 F86040.

Horjen, I., Vefsnmo, S., 1987. Time-Dependent Sea Spray Icing on Ships and Drilling Rigs—a Theoretical Analysis. Norwegian Hydrodynamic Laboratories Report STF60F87130.

Howison, S.D., Ockendon, J.R., Wilson, S.K., 1991. Incompressible water-entry problems at small deadrise angles. J. Fluid Mech. 222, 215–230.

Hu, C., Kashiwagi, M., Kitadai, A., 2006. Numerical Simulation of Strongly Nonlinear Wave-Body Interactions with Experimental Validation. Proc. 16th Int. Offshore and Polar Eng. Conf. vol. 4. ISOPE, San Francisco, pp. 420–427.

Hu, C., Kashiwagi, M., 2009, "Two-dimensional numerical simulation and experiment on strongly nonlinear wave-body interactions," J. Mar. Sci. Technol. V. 14 (2), pp. 200-213.

Huh, K.Y., Lee, E., Koo, J.Y., 1988. Diesel spray atomization model considering nozzle exit turbulence conditions. Atomiz. Sprays, 8: 453–469.

Iafrati, A., Mascio, A.D., Campana, E.F., 2001. A level set technique applied to unsteady free surface flows. Int. J. Numer. Methods Fluids 35, 281–297.

Jaynes, E.T., 1957. Information Theory and Statistical Mechanics, Phys. Rev., vol. 106, pp. 620-630.

Jazayeri, S. A., Li, X., 1997. Nonlinear breakup of liquid sheets, 8th Annual Int. Energy Week, vol.8, pp. 389-393.

Kapsenberg, G.K., 2011. Slamming of ships: where are we now? Phil. Trans. R. Soc. A 369, 2892–2919. http://dx.doi.org/10.1098/rsta.2011.0118.

Katchurin, L.G., Gashin, L.I., Smirnov, I.A., 1974. Icing Rate of Small Displacement Fishing Vessels under Various Hydro-Meteorological Conditions. Meteorologiya I Gidrologiya. Moscow, No.3, pp. 50–60.

Kees, C.E., Akkerman, I., Farthing,M.W., Bazilevs, Y., 2011. A conservative level set method suitable for variable-order approximations and unstructured meshes. J. Comput. Phys. 230, 4536–4558.

Kelbaliyev, G., Ceylan, K., 2007. Development of new empirical equations for estimation of drag coefficient, shape deformation, and rising velocity of gas bubbles or liquid drops. Chem. Eng. Commun. 194, 1623–1637.

Kim, W.T., Mitra, S.K., Li, X., Prociw, L.A., Hu, T.C.J., 2003. A predictive model for the initial droplet size and velocity distributions in sprays and comparison with experiments. Part. Syst. Charact., 20, 135-149.

Kim, D., Im, J., Koh, H., Yoon, Y., 2007, "Effect of ambient gas density on spray characteristics of swirling liquid sheets," J. Propul. Power. V. 23, pp. 603–611.

Kleefsman, K. M. T., Fekken, G., Veldman, A. E. P., Iwanowski, B., Buchner, B., 2005, "A volume of fluid based simulation method for wave impact problems," J. Comput. Phys. V. 206, pp. 363-393.

Kline, S.J., McClintock, F.A., 1953. Describing the uncertainties in single-sample experiments. Mech. Eng. 3–8.

Komori, S., Nagata, K., Kanzaki, T., Murakami, Y., 1993. Measurements of Mass Flux in a Turbulent Liquid Flow with a Chemical Reaction. AIChE Journal 39, 1611–1620.

Korobkin, A.A., Scolan, Y.M., 2003. Three-dimensional theory of water impact—part 2. Linearized Wagner problem. J. Fluid Mech.

Korobkin, A.A., 2004. Analytical models of water impact. Eur. J. Appl. Math 15, 821–838.

Kulyakhtin, A., Shipilova, O., Libby, B., Loset, S., 2012. Full-Scale 3D CFD Simulation of Spray Impingement on a Vessel Produced by Ship-Wave Interaction. The 21st IAHR International Symposium on Ice, Dalian, China, p. 11291141.

Kulyakhtin, A., Tsarau, A., 2014. A time-dependent model of marine icing with application of computational fluid dynamics. Cold Reg. Sci. Technol. 104-105, 33–44.

Kuzniecov, V.P., Kultashev, Y.N., Panov, V.V., Tiurin, A.P., Sharapov, A.V., 1971. Field investigations of ship icing in the Japan Sea in 1969. Theoretical and Experimental Investigation of the Conditions of Ship Icing. Gidrometeoizdat, Leningrad, pp. 57–69.

Lafaurie, B., Nardone, C., Scardovelli, R., Zaleski, S., Zanetti, G., 1994. Modelling, merging and fragmentation in multiphase flows with SURFER. J. Comput. Phys. 113, 134–147.

Lee, C.H., Reitz, R.D., 2000. An experimental study of the effect of gas density on the distortion and breakup mechanism of drops in high speed gas stream. Int. J. Multiph. Flow 26, 229–244.

Leonard, B. P., Mokhtari, S., 1990. "ULTRA-SHARP Nonoscillatory Convection Schemes for High-Speed Steady Multidimensional Flow," NASA Lewis Research Center, NASATM1-2568 (ICOMP-90-12).

Leonard, B. P., 1979, "A stable and accurate convective modeling procedure based on quadratic upstream interpolation," Comput. Methods Appl. Mech. Eng. V. 19, pp. 59-98.

LeTouzé, D., Colagrossi, A., Colicchio, G., 2006, “Ghost technique for right angles applied to the solution of benchmarks 1 and 2,” In Proceedings of 1st SPHERIC Workshop, Rome, Italy.

Li, X., Tankin, R.S., 1987. Droplet size distribution: a derivation of a Nukiyama-Tanasawa type distribution function. Comb. Sci. Technol., 56, 65-76. 16.

Li, X., Tankin, R.S., 1988. Derivation of droplet size distribution in sprays by using information theory. Comb. Sci. Technol., 60, 345-357.

Li, X., Tankin, R. S., 1991. On the Temporal Instability of a Two-Dimensional Viscous Liquid Sheet, J. Fluid Mech., vol. 17, pp. 291-305.

Lin, P.Z., Liu, P.L.-F., 1998a. A numerical study of breaking waves in the surf zone. J. Fluid Mech. 359, 239–264.

Lin, P.Z., Liu, P.L.-F., 1998b. Turbulence transport, vorticity dynamics, and solute mixing under plunging breaking waves in surf zone. J. Geophys. Res. 103, 15677–15694.

Longuet-Higgins, M.S., 1974. Breaking Waves in Deep or Shallow Water. Proc. 10th Symop. On Naval Hydrodynamics. Off. Of Naval Res., pp. 597–605.

Lozowski, E., Zakrzewski, W.P., 1990. An Integrated Ship Spraying/Icing Model. Milestone Report No. 2. Contract Report by the University of Alberta, Edmonton, to USA Cold Regions Research and Engineering Laboratory.

Lozowski, E.P., Zakrzewski, W.P., 1993. Topside Ship Icing System. Final Report to the US Army Cold Regions Research and Engineering Laboratory.

Lozowski, E.P., Szilder, K., Makkonen, L., 2000. Computer simulation of marine ice accretion. Philos. Trans. R. Soc. Lond. Ser. A 358, 2811–2845.

Lugni, C., Miozzi, M., Brocchini, M., Faltinsen, O. M., 2010, “Evolution of the air cavity in a depressurized wave impact, I. The kinematic flow field”, Phys. Fluids, Vol. 22, 056101.

Marsooli, R., Wu, W., 2014. 3-D Finite volume method of dam-break flow over uneven beds based on VOF method. Advances in Water Resources 70, 104–117.

Mei, C.C., 1978. Numerical methods in water-wave diffraction and radiation. Annu. Rev. Fluid Mech. 10, 393–416.

Mei, X., Liu, Y., Yue, D.K.P., 1999. On the water impact of general two-dimensional sections. Appl. Ocean Res. 21, 1–15.

Melville, W.K., 1994. Energy dissipation in breaking waves. J. Phys. Oceanogr. 42 (10), 2041–2049.

Melville, W.K., 1996. The role of surface-wave breaking in air–sea interaction. Annu. Rev. Fluid Mech. 28, 279–321.

Melville, W.K., Veron, F., White, C.J., 2002. “The velocity field under breaking waves: coherent structures and turbulence.” J. Fluid. Mech. 454, 203-233.

Moraga, F.J., Carrica, P.M., Drew, D.A., Lahey Jr., R.T., 2008. A sub-grid air entrainment model for breaking bow waves and naval surface ships. Compute. Fluids 37, 281–298.

Muzik, I., Kirby, A., 1992. Spray over-topping rates for Tarsiut Island: model and field study results”, Can. J. Civ. Eng. Vol. 19, 469–477.

Nicholas, B.D., Hirt, C.W., 1975. Proceedings First Intern. Conf. Num. Ship Hydrodynamics, Gaithersburg, Md, October.

Nukiyama, S., Tanasawa, T., 1939. Experiments on the atomization of liquids in an air stream. Report 3: on the droplet-size distribution in an atomized jet. Trans Soc. Mech. Engrs. Jpn, 5, pp. 62–67.

Ogilvie, F., 1963. First and second order forces on a cylinder submerged under a free-surface. J. Fluid Mech. 16, 451–472.

Olsson, E., Kreiss, G., 2005. A conservative level set method for two phase flow. J. Compute. Phys. 210, 225–246.
Olsson, E., Kreiss, G., Zahedi, S., 2007. A conservative level set method for two phase flow II. J. Compute. Phys. 225, 785–807.
Osher, S., Sethian, J. A., 1988, "Fronts Propagating with Curvature-dependent Speed: Algorithms Based on Hamilton-Jacobi Formulations," J. Comput. Phys., V. 79, pp. 12-49.
Peregrine, D., 2003.Water-wave impact on walls. Annual Review of Fluid Mechanics Vol. 35, 23–43.
Qian, L., Causon, D.M., Mingham, C.G., Ingram, D.M., 2006. A free-surface capturing method for two fluid flows with moving bodies. Proc. R. Soc. A 462, 21–42.
Ran, Q., Tong, J., Shao, S., Fu, X., Xu, Y., 2015. Incompressible SPH scourmodel for movable bed dam break flows. Advances in Water Resources 82, 39–50.
Ray, S.F., 2002. Applied Photographic Optics: Lenses and Optical Systems for Photography, Film, Video, Electronic and Digital Imaging, 3rd edn. Focal Press Oxford.
Rayleigh, L., 1917, "On periodic irrotational waves at the surface of deep water," Philosophical Magazine, Series 6, 33 (197): 381–389.
Rayleigh, Lord, 1879, "On the capillary phenomena of jets," Proc. R. Soc. London, Vol. 29, pp. 71–97.
Ren, B.,Wang, Y., 2004. Numerical simulation of random wave slamming on structures in the splash zone. Ocean Eng. 31 (5–6), 547–560.
Rider, W.J., Kothe, D.B., 1998. Reconstructing volume tracking. J. Comput. Phys. 141, 112–152.
Roebber, P., Mitten, P., 1987, "Modeling and Measurement of Icing in Canadian Waters," Canadian Climate Centre Report, pp. 87–15.
Romagnoli, R., 1988. Ice Growth Modelling for Icing Control Purposes of offshore Marine Units Employed by the Petroleum Industry. Proc. Int. Association for Hydraulic Research Symposium on Ice, Sapporo, pp. 486–497.
Rosin, P., Rammler, E., 1993. The laws governing the fineness of powdered coal. J. Inst. Fuel, 7:29-36.
Ryerson, C., 1990. Atmospheric icing rates with elevation on northern New England Mountains. U.S.A, Arctic and Alpine Research 22 (1), 90–97.
Ryerson, C. C., 1995, "Superstructure spray and ice accretion on a large U.S. Coast Guard Cutter", Atmospheric Research Vol. 36, pp. 321 -337.
Ryerson, C., 2013, "Icing Management for Coast Guard Assets. Cold Regions Research and Engineering Laboratory," ERDC/CRREL TR-13-7.
Ryu, Y., Chang, K.A., Lim, H.J., 2005. "Use of bubble image velocimetry for measurement of plunging wave impinging on structure and associated green water." Meas. Sci. Technol. 16(10), 1945-1953.
Ryu, Y.G., Chang, K.A., Mercier, R., 2007a. Run-up and green water velocities due to breaking wave impinging and overtopping. Exp. Fluids 43 (4), 555–567.
Ryu, Y., Chang, K.A., Mercier, R., 2007b. Application of dam-break flow to green water prediction. Appl. Ocean Res. 29 (3), 128–136.
Sarpkaya, T., 1986. Trailing-Vortex Wakes on the Free Surface, Proceedings of the 16th Symposium on Naval Hydrodynamics. National Academy Press, Washington, D. C., pp. 38–50.
Scardovelli, R., Zaleski, S., 1999. Direct numerical simulation of free-surface and interfacial flow. Annu. Rev. Fluid Mech. 31, 567–603.

Scolan, Y.M., Korobkin, A.A., 2001. Three-dimensional theory of water impact-part 1. Inverse Wagner problem. J. Fluid Mech. 440, 293–326.
Sellens, R.W., Brzustowski, T.A., 1985. A prediction of the drop-size distribution in a spray from first principles. Atom. Spray Tech., 1, 89-102.
Sellens, R.W., Brzustowski, T.A., 1986. A simplified prediction of droplet velocity distribution in a spray. Comb. Flame, 65, 273-279.
Sharapov, A.V., 1971. On the Intensity of Superstructure Icing of Small Vessels (MFV Type). Theoretical and Experimental Investigations of the Conditions of Ship Icing. Gidrometeoizdat, Leningrad, pp. 95–97 (in Russian).
Shannon, C. E., 1948. A Mathematical Theory of Communication, Bell System Tech. J., pp. 379-623.
Shipilova, O., Kulyakhtin, A., Tsarau, A., Libby, B., Moslet, P.O., Loset, S., 2012. Mechanism and dynamics of marine ice accretion on vessel archetypes. Offshore Technol. Conf.
Song, Y.K., Chang, K-A., Ryu, Y., Kwon, S.H., 2013. "Experimental study on flow kinematics and impact pressure in liquid sloshing." Exp. Fluids 54(9), 1-20.
Squire, H. B., 1953, "Investigation of the Instability of a Moving Liquid Film, Br. J. Appl. Phys., vol. 4, pp. 167-169.
Stokes, G. G. (1880). "Mathematical and Physical Papers, Volume I." Cambridge University Press. pp. 197–229.
Sussman, M., Puckett, E., 2000. A coupled level set and volume-of-fluid method for computing 3d and axisymmetric incompressible two phase flows. J. Comput. Phys. 162, 301–337.
Sussman, M., Smereka, P., Osher, S., 1994. A level-set approach for computing solutions to incompressible two-phase flow. J. Comput. Phys. 114, 146–159.
Sutherland, P., Melville, W.K., 2013. Field measurements and scaling of ocean surface wave-breaking statistics. Geophys. Res. Lett. 40, 3074–3079.
Takahashi, S., Tanimoto, K., Miyanaga, S., 1985, "Uplift wave forces due to compression of enclosed air layer and their similitude law," Coast. Eng. Japan Vol. 28, pp. 191- 206.
Ting, F.C.K., Kirby, J.T., 1995. Dynamics of surf-zone turbulence in a strong plunging breaker. Coastal Engineering 24, 177–204.
Ting, F.C.K., Kirby, J.T., 1996. Dynamics of surf-zone turbulence in a spilling breaker. Coastal Engineering 27, 31–160.
Tornberg, A.K., Enhquist, B., 2000. A finite element based level set method for multiphase flow applications. Comput. Vis. Sci. 3, 93–101.
Tsai, W.T., 1998. A numerical study of the evolution and structure of a turbulent shear layer under a free surface. J. Fluid Mech. 354, 239.
Tsai, W.T., Yue, D.K.P., 1996. Computation of nonlinear free surface flows. Annu. Rev. Fluid Mech. 28, 249–278.
Voogt, A.J., Buchner, B., 2004.Wave Impact Excitation on Ship-Type Offshore Structures in Steep Fronted Waves. Proceedings OMAE Speciality Conference on Integrity of Floating Production, Storage & Offloading (FPSO) Systems, Houston, TX, August– September, Paper OMAE-FPSO'04–0062.
Wagner, H., 1932. Uber Stoss- und Gleitvorgange an der Oberflache von Flussigkeiten. ZAMM 12, 193–215 (In German).
Wang, Y.X., Ren, B., 1999. Study on wave slamming by turbulent model. J. Hydrodyn. Dyn. Ser. A 14 (4), 409–417.

Waniewski, T.A., Brennen, C.E., Raichlen, F., 2001. Measurement of air entrainment by bow waves. J. Fluids Eng. 123, 57–63.
Watanabe, Y., Ingram, D.M., 2015. Transverse instabilities of ascending planar jets formed by wave impacts on vertical walls. Proc. R. Soc. A 471, 20150397.
Watanabe, Y., Ingram, D.M., 2016. Size distribution of sprays produced by violent wave impacts on vertical sea walls. Proc. R. Soc. A 472, 20160423.
Willert, C.E., Gharib, M., 1991. Digital particle image velocimetry. Exp. Fluids 10, 181-193.
White, F.M. Viscous Fluid Flow, 2nd ed.; McGraw-Hill: New York, NY, USA, 1991.
Xuelin, L., Bing, R., Yongxue, W., 2009. Numerical Study of the Irregular Wave Impacting. Proceedings of the 19th International Offshore and Polar Engineering Conference, Osaka, Japan, pp. 510–517.
Youngs, D. L., 1982, "Time-Dependent Multi-Material Flow with Large Fluid Distortion," In book: Numerical Methods in Fluid Dynamics, Publisher: Academic Press, Editors: K. W. Morton and M. J. Baines, pp. 273-285.
Youngs, D.L., 1987. An Interface Tracking Method for a 3D Eulerian Hydrodynamics Code. Technical Report AWRE/44/92/35. Atomic Weapons Research Establishment.
Yue, W., Lin, C.L., Patel, V.C., 2003. Numerical Investigation of Turbulent Free Surface Flows Using Level Set Method and Large Eddy Simulation. IIHR Technical Report No. 435, Iowa City, Iowa 52242–1585.
Zakrzewski, W.P., 1986. Icing of Fishing Vessels. Part 1: Splashing a Ship with Spray. Proceedings of the 8th Int. IAHR Symposium on Ice, Iowa City, August 18–22 vol. 2, pp. 179–194.
Zakrzewski, W.P., 1987. Splashing a ship with collision-generated spray. Cold Reg. Sci. Technol. 14, 65–83.
Zakrzewski, W.P., Lozowski, E.P., Muggeridge, D., 1988. Estimating the extent of the spraying zone on a sea-going ship. Ocean Eng. 15, 413–430.
Zhao, R., Faltinsen, O., 1993. Water entry of two-dimensional bodies. J. Fluid Mech. 246, 593–612.
Zhao, R., Faltinsen, O., Aarsnes, J., 1996. Water Entry of Arbitrary two-Dimensional Sections with and without Separation. Proc. 21st Symposium on Naval Hydrodynamics. National Academy Press 1997, Washington, DC, pp. 118–133 (Trondheim, Norway).
Zhao, Q., Armfield, S., Tanimoto, K., 2004. Numerical simulation of breaking waves by a multi-scale turbulence model. Coast. Eng. 51, 53–80.

Appendices 1 – Matlab Codes

MEP Code – 1D

```
clc
clear
syms lambda i j lambda0 lambda1 lambda2 lambda3
lambda=[lambda0;lambda1;lambda2;lambda3];  %initial values
Sm=0;
Se=0;
Smu=-3.057*10^(-5);
n=15;                    %upper limit for u summation
m=15;                    %upper limit for d summation
Dmax=1.5*10^(-3);
Dmin=0.1*10^(-3);
D30=0.000537;            %sigma md/M
Umax=8;
Umin=0;
U0=2.2;
l=15;                 %segmentation of integral to summation for d
p=15;                 %segmentation of integral to summation for u
d=(Dmin+(Dmax-Dmin)*i/l)/D30;
u=(Umin+(Umax-Umin)*j/p)/U0;
delu=(Umax-Umin)/p;
deld=(Dmax-Dmin)/l;
Ro=998.2;                %fluid density
sigma=0.0736;
We=Ro*U0^2*D30/sigma;  %weber number
B=12/We;
H=1;
Q=d^3*u^2/H+B*d^2/H;
ln = @log;


% First Four Functions
g1=symsum(symsum(-3*d^5*exp(-lambda(1)-lambda(2)*d^3-lambda(3)*d^3*u-
lambda(4)*Q)*delu*deld,j,1,n),i,1,m)-1-Sm;
g2=symsum(symsum(-3*d^5*Q*exp(-lambda(1)-lambda(2)*d^3-lambda(3)*d^3*u-
lambda(4)*Q)*delu*deld,j,1,n),i,1,m)-1-Se;
g3=symsum(symsum(-3*d^2*u*exp(-lambda(1)-lambda(2)*d^3-lambda(3)*d^3*u-
lambda(4)*Q)*delu*deld,j,1,n),i,1,m)-1-Smu;
g4=symsum(symsum(-3*d^2*exp(-lambda(1)-lambda(2)*d^3-lambda(3)*d^3*u-
lambda(4)*Q)*delu*deld,j,1,n),i,1,m)-1;
g=[g1;g2;g3;g4];

% Jacobian Matrix
G1=symsum(symsum(-3*d^5*exp(-lambda(1)-lambda(2)*d^3-lambda(3)*d^3*u-
lambda(4)*Q),j,1,n),i,1,m);
G2=symsum(symsum(-3*d^8*exp(-lambda(1)-lambda(2)*d^3-lambda(3)*d^3*u-
lambda(4)*Q),j,1,n),i,1,m);
G3=symsum(symsum(-3*d^8*u*exp(-lambda(1)-lambda(2)*d^3-lambda(3)*d^3*u-
lambda(4)*Q),j,1,n),i,1,m);
```

```
G4=symsum(symsum(-3*d^5*Q*exp(-lambda(1)-lambda(2)*d^3-lambda(3)*d^3*u-
lambda(4)*Q),j,1,n),i,1,m);
G5=symsum(symsum(-3*d^5*u*exp(-lambda(1)-lambda(2)*d^3-lambda(3)*d^3*u-
lambda(4)*Q),j,1,n),i,1,m);
G6=symsum(symsum(-3*d^8*u*exp(-lambda(1)-lambda(2)*d^3-lambda(3)*d^3*u-
lambda(4)*Q),j,1,n),i,1,m);
G7=symsum(symsum(-3*d^8*u^2*exp(-lambda(1)-lambda(2)*d^3-
lambda(3)*d^3*u-lambda(4)*Q),j,1,n),i,1,m);
G8=symsum(symsum(-3*d^5*u*Q*exp(-lambda(1)-lambda(2)*d^3-
lambda(3)*d^3*u-lambda(4)*Q),j,1,n),i,1,m);
G9=symsum(symsum(-3*d^2*Q*exp(-lambda(1)-lambda(2)*d^3-lambda(3)*d^3*u-
lambda(4)*Q),j,1,n),i,1,m);
G10=symsum(symsum(-3*d^5*Q*exp(-lambda(1)-lambda(2)*d^3-lambda(3)*d^3*u-
lambda(4)*Q),j,1,n),i,1,m);
G11=symsum(symsum(-3*d^5*u*Q*exp(-lambda(1)-lambda(2)*d^3-
lambda(3)*d^3*u-lambda(4)*Q),j,1,n),i,1,m);
G12=symsum(symsum(-3*d^2*Q^2*exp(-lambda(1)-lambda(2)*d^3-
lambda(3)*d^3*u-lambda(4)*Q),j,1,n),i,1,m);
G13=symsum(symsum(-3*d^2*exp(-lambda(1)-lambda(2)*d^3-lambda(3)*d^3*u-
lambda(4)*Q),j,1,n),i,1,m);
G14=symsum(symsum(-3*d^5*exp(-lambda(1)-lambda(2)*d^3-lambda(3)*d^3*u-
lambda(4)*Q),j,1,n),i,1,m);
G15=symsum(symsum(-3*d^5*u*exp(-lambda(1)-lambda(2)*d^3-lambda(3)*d^3*u-
lambda(4)*Q),j,1,n),i,1,m);
G16=symsum(symsum(-3*d^2*Q*exp(-lambda(1)-lambda(2)*d^3-lambda(3)*d^3*u-
lambda(4)*Q),j,1,n),i,1,m);
J=[G1 G2 G3 G4;G5 G6 G7 G8; G9 G10 G11 G12; G13 G14 G15 G16];

N=100;              %number of iterations
epsilon = 1e-4;     %tolerance
maxval = 10000;     %divergence value
%lambda_init=[6.7715;-0.2495;0.2964;-0.1833]; % The last answer with
resolution of 1e-4
%lambda_init=[0.5;-0.015;0.0015;-0.001];  %started with this and get
answer
lambda_init=[0.9;0.1;-0.005;0.01];

while (N>0)

   JJ= eval(subs(J, lambda, lambda_init));
   lambda_new=lambda_init - inv(JJ)* eval(subs(g, lambda, lambda_init));
   lambda_new(1)=ln(symsum(symsum(exp(-lambda_new(2)*d^3-
lambda_new(3)*d^3*u-lambda_new(4)*Q),j,1,n),i,1,m));
   lambda_new=subs(lambda_new, lambda_new(1,1), lambda_new(1));
   abs(abs(eval(subs(g, lambda, lambda_new)))-abs(eval(subs(g, lambda,
lambda_init))))

   if abs(abs(eval(subs(g, lambda, lambda_new)))-abs(eval(subs(g,
lambda, lambda_init))))< epsilon
       lambda_init=lambda_new;
       iter = 100-N;
       return;
    end
```

```
   if abs(eval(subs(g, lambda, lambda_new)))>maxval
      iter=100-N;
      disp(['iteration= ', num2str(iter)]);
      error ('Solution diverges');
      abort;
   end

    N=N-1;
    lambda_init=lambda_new
    norm(eval(subs(g, lambda, lambda_new)))

end;
error(' No convergence after iterations.');
abort;
```

%PDF

```
clc
clear
%syms d u
lambda=[3.6529;2.1035; -3.0007;1.2549];
vmax=3.65;
vmin=1.15;
D30=0.000537;           %sigma md/M
U0=2.2;
Ro=998.2;               %fluid density
sigma=0.0736;
We=Ro*U0^2*D30/sigma;   %weber number
B=12/We;
H=1;
%d=0:0.01:3;
%u=0:0.01:3;
d=linspace(0,4);
u=linspace(0,4);
[d,u]=meshgrid(d,u);
Q=(d.^3.*u.^2/H)+(B.*d.^2/H);
f=3.*d.^2.*exp(-lambda(1)-lambda(2).*d.^3-lambda(3).*d.^3.*u-
lambda(4).*Q);
mesh(d,u,f)
```

%Plots

```
ambda=[3.6529;2.1035;-3.0007;1.2549];
vmax=3.65;
vmin=1.15;
D30=0.000537;           %sigma md/M
U0=2.2;
Ro=998.2;               %fluid density
sigma=0.0736;
We=Ro*U0^2*D30/sigma;   %weber number
B=12/We;
d=0:0.01:4
```

```
A=(vmax+lambda(3)/(2*lambda(4)))*(lambda(4)*d.^3).^0.5;
B=(vmin+lambda(3)/(2*lambda(4)))*(lambda(4)*d.^3).^0.5;
%AA=erf(A)
%BB=erf(B)
x=(3/2).*(pi.*d/lambda(4)).^0.5.*(erf(A)-erf(B)).*exp(-lambda(1)-
lambda(4).*B.*d.^2-[lambda(2)-(lambda(3).^2/(4.*lambda(4)))].*d.^3);
plot(d,x)

lambda=[3.6529;2.1035; -3.0007;1.2549];
vmax=3.65;
vmin=1.15;
D30=0.000537;          %sigma md/M
U0=2.2;
Ro=998.2;              %fluid density
sigma=0.0736;
We=Ro*U0^2*D30/sigma;  %weber number
B=12/We;
H=1;
%d=0:0.01:3;
%u=0:0.01:3;
d=linspace(0,4);
u=linspace(0,4);
[d,u]=meshgrid(d,u);
Q=(d.^3.*u.^2/H)+(B.*d.^2/H);
f=3.*d.^2.*exp(-lambda(1)-lambda(2).*d.^3-lambda(3).*d.^3.*u-
lambda(4).*Q);
contour(d,u,f,20,'ShowText','on')
```

MEP – 2D

```
clc
clear
syms lambda i j k lambda0 lambda1 lambda2 lambda3 lambda4 lambda5
lambda=[lambda0;lambda1;lambda2;lambda3;lambda4;lambda5];  %initial
values

n=5;                  %upper limit for u summation
m=5;                  %upper limit for d summation
l=5;                  %upper limit for v summation

Dmax=2000*10^(-6);
Dmin=100*10^(-6);
D30=750*10^(-6);         %sigma md/M
D32=850*10^(-6);

Umax=15;
Umin=0;
Vmax=15;
Vmin=0;
z=20;          %Water sheet breakup degree
U=10;
```

```
U0=U*0.93;
V0=U*0.34;

p=10;                %segmentation of integral to summation for d
q=10;                %segmentation of integral to summation for u
r=10;                %segmentation of integral to summation for v

d=(Dmin+(Dmax-Dmin)*i/p)/D30;
u=(Umin+(Umax-Umin)*j/q)/U0;
v=(Vmin+(Vmax-Vmin)*k/r)/V0;

uu=U0/U;
vv=V0/U;
%uu=1;
%vv=1;

delu=(Umax-Umin)/p;
deld=(Dmax-Dmin)/q;
delv=(Vmax-Vmin)/r;

%Ro=998.2;              %fluid density
%sigma=0.0736;
%We=Ro*U^2*D30/sigma;    %weber number
%B=12/We;
%H=1;
%Q=d^2*u^2/H+B*d^2/H;

ln = @log;
T=0.1;

Roa=1.2041;
Rol=1000;
Mo=8.9e-4;
L=0.8;

Rey= Rol*U0*L/Mo;
Rex= Rol*V0*L/Mo;

if Rey > 1e3
    Cdy=1.328/sqrt(Rey);
end

if 1< Rey < 1e3
    Cdy=(1.328/sqrt(Rey))+2.3/Rey;
end

if Rex > 1e3
    Cdx=1.328/sqrt(Rex);
end

if 1< Rex < 1e3
    Cdx=(1.328/sqrt(Rex))+2.3/Rex;
```

```
end

b=1;
c=1.40;
Lb=L/3;
t=T;

Sm=0;
Smu=(Roa/Rol)*Cdy*0.5*(b+c)*Lb/(b*t);
Smv=(Roa/Rol)*Cdx*0.5*(b+c)*Lb/(b*t);
%Smu=1;
%Smv=1;
Ske=0;
Ss=D30/D32;
%Ss=1;

% First six Functions
g1=symsum(symsum(symsum(d^3*exp(-lambda(1)-lambda(2)*d^2-lambda(3)*d^3-
lambda(4)*d^3*u-lambda(5)*d^3*v-
lambda(6)*d^3*(u^2+v^2))*delu*deld*delv,k,1,l),i,1,n),j,1,m)-1-Sm;
g2=symsum(symsum(symsum(d^3*u*exp(-lambda(1)-lambda(2)*d^2-
lambda(3)*d^3-lambda(4)*d^3*u-lambda(5)*d^3*v-
lambda(6)*d^3*(u^2+v^2))*delu*deld*delv,k,1,l),i,1,n),j,1,m)-uu-Smu;
g3=symsum(symsum(symsum(d^3*v*exp(-lambda(1)-lambda(2)*d^2-
lambda(3)*d^3-lambda(4)*d^3*u-lambda(5)*d^3*v-
lambda(6)*d^3*(u^2+v^2))*delu*deld*delv,k,1,l),j,1,m),i,1,n)-vv-Smv;
g4=symsum(symsum(symsum(d^3*(u^2+v^2)*exp(-lambda(1)-lambda(2)*d^2-
lambda(3)*d^3-lambda(4)*d^3*u-lambda(5)*d^3*v-
lambda(6)*d^3*(u^2+v^2))*delu*deld*delv,k,1,n),j,1,n),i,1,n)-uu^2-vv^2-
Ske;
g5=symsum(symsum(symsum(d^2*exp(-lambda(1)-lambda(2)*d^2-lambda(3)*d^3-
lambda(4)*d^3*u-lambda(5)*d^3*v-
lambda(6)*d^3*(u^2+v^2))*delu*deld*delv,k,1,l),i,1,n),j,1,m)-Ss;
g6=symsum(symsum(symsum(exp(-lambda(1)-lambda(2)*d^2-lambda(3)*d^3-
lambda(4)*d^3*u-lambda(5)*d^3*v-
lambda(6)*d^3*(u^2+v^2))*delu*deld*delv,k,1,l),i,1,n),j,1,m)-1;
g=[g1;g2;g3;g4;g5;g6];

%for i=1:5
% for j=1:5
%   for k=1:5
%       g1=d^3*exp(-lambda(1)-lambda(2)*d^2-lambda(3)*d^3-
lambda(4)*d^3*u-lambda(5)*d^3*v-lambda(6)*d^3*(u^2+v^2))*delu*deld*delv-
1-Sm;
%       g2=d^3*u*exp(-lambda(1)-lambda(2)*d^2-lambda(3)*d^3-
lambda(4)*d^3*u-lambda(5)*d^3*v-lambda(6)*d^3*(u^2+v^2))*delu*deld*delv-
uu-Smu;
%       g3=d^3*v*exp(-lambda(1)-lambda(2)*d^2-lambda(3)*d^3-
lambda(4)*d^3*u-lambda(5)*d^3*v-
lambda(6)*d^3*(u^2+v^2))*delu*deld*delv,k,1,l),i,1,n),j,1,m)-vv-Smv;
%       g4=d^3*(u^2+v^2)*exp(-lambda(1)-lambda(2)*d^2-lambda(3)*d^3-
lambda(4)*d^3*u-lambda(5)*d^3*v-
lambda(6)*d^3*(u^2+v^2))*delu*deld*delv,k,1,l),i,1,n),j,1,m)-uu^2-vv^2-
Ske;
```

```
%       g5=d^2*exp(-lambda(1)-lambda(2)*d^2-lambda(3)*d^3-
lambda(4)*d^3*u-lambda(5)*d^3*v-
lambda(6)*d^3*(u^2+v^2))*delu*deld*delv,k,1,l),i,1,n),j,1,m)-1/(3*T)-Ss;
%       g6=exp(-lambda(1)-lambda(2)*d^2-lambda(3)*d^3-lambda(4)*d^3*u-
lambda(5)*d^3*v-
lambda(6)*d^3*(u^2+v^2))*delu*deld*delv,k,1,l),i,1,n),j,1,m)-1;
%
%   end
% end
%end

% Jacobian Matrix
G1=symsum(symsum(symsum(-d^3*exp(-lambda(1)-lambda(2)*d^2-lambda(3)*d^3-
lambda(4)*d^3*u-lambda(5)*d^3*v-
lambda(6)*d^3*(u^2+v^2)),k,1,l),j,1,n),i,1,m);
G2=symsum(symsum(symsum(-d^5*exp(-lambda(1)-lambda(2)*d^2-lambda(3)*d^3-
lambda(4)*d^3*u-lambda(5)*d^3*v-
lambda(6)*d^3*(u^2+v^2)),k,1,l),j,1,n),i,1,m);
G3=symsum(symsum(symsum(-d^6*exp(-lambda(1)-lambda(2)*d^2-lambda(3)*d^3-
lambda(4)*d^3*u-lambda(5)*d^3*v-
lambda(6)*d^3*(u^2+v^2)),k,1,l),j,1,n),i,1,m);
G4=symsum(symsum(symsum(-d^6*u*exp(-lambda(1)-lambda(2)*d^2-
lambda(3)*d^3-lambda(4)*d^3*u-lambda(5)*d^3*v-
lambda(6)*d^3*(u^2+v^2)),k,1,l),j,1,n),i,1,m);
G5=symsum(symsum(symsum(-d^6*v*exp(-lambda(1)-lambda(2)*d^2-
lambda(3)*d^3-lambda(4)*d^3*u-lambda(5)*d^3*v-
lambda(6)*d^3*(u^2+v^2)),k,1,l),j,1,n),i,1,m);
G6=symsum(symsum(symsum(-d^6*(v^2+u^2)*exp(-lambda(1)-lambda(2)*d^2-
lambda(3)*d^3-lambda(4)*d^3*u-lambda(5)*d^3*v-
lambda(6)*d^3*(u^2+v^2)),k,1,l),j,1,n),i,1,m);
G7=symsum(symsum(symsum(-d^3*u*exp(-lambda(1)-lambda(2)*d^2-
lambda(3)*d^3-lambda(4)*d^3*u-lambda(5)*d^3*v-
lambda(6)*d^3*(u^2+v^2)),k,1,l),j,1,n),i,1,m);
G8=symsum(symsum(symsum(-d^5*u*exp(-lambda(1)-lambda(2)*d^2-
lambda(3)*d^3-lambda(4)*d^3*u-lambda(5)*d^3*v-
lambda(6)*d^3*(u^2+v^2)),k,1,l),j,1,n),i,1,m);
G9=symsum(symsum(symsum(-d^6*u*exp(-lambda(1)-lambda(2)*d^2-
lambda(3)*d^3-lambda(4)*d^3*u-lambda(5)*d^3*v-
lambda(6)*d^3*(u^2+v^2)),k,1,l),j,1,n),i,1,m);
G10=symsum(symsum(symsum(-d^6*u^2*exp(-lambda(1)-lambda(2)*d^2-
lambda(3)*d^3-lambda(4)*d^3*u-lambda(5)*d^3*v-
lambda(6)*d^3*(u^2+v^2)),k,1,l),j,1,n),i,1,m);
G11=symsum(symsum(symsum(-d^6*u*v*exp(-lambda(1)-lambda(2)*d^2-
lambda(3)*d^3-lambda(4)*d^3*u-lambda(5)*d^3*v-
lambda(6)*d^3*(u^2+v^2)),k,1,l),j,1,n),i,1,m);
G12=symsum(symsum(symsum(-d^6*u*(v^2+u^2)*exp(-lambda(1)-lambda(2)*d^2-
lambda(3)*d^3-lambda(4)*d^3*u-lambda(5)*d^3*v-
lambda(6)*d^3*(u^2+v^2)),k,1,l),j,1,n),i,1,m);
G13=symsum(symsum(symsum(-d^3*v*exp(-lambda(1)-lambda(2)*d^2-
lambda(3)*d^3-lambda(4)*d^3*u-lambda(5)*d^3*v-
lambda(6)*d^3*(u^2+v^2)),k,1,l),j,1,n),i,1,m);
G14=symsum(symsum(symsum(-d^5*v*exp(-lambda(1)-lambda(2)*d^2-
lambda(3)*d^3-lambda(4)*d^3*u-lambda(5)*d^3*v-
lambda(6)*d^3*(u^2+v^2)),k,1,l),j,1,n),i,1,m);
```

```
G15=symsum(symsum(symsum(-d^6*v*exp(-lambda(1)-lambda(2)*d^2-
lambda(3)*d^3-lambda(4)*d^3*u-lambda(5)*d^3*v-
lambda(6)*d^3*(u^2+v^2)),k,1,l),j,1,n),i,1,m);
G16=symsum(symsum(symsum(-d^6*v*u*exp(-lambda(1)-lambda(2)*d^2-
lambda(3)*d^3-lambda(4)*d^3*u-lambda(5)*d^3*v-
lambda(6)*d^3*(u^2+v^2)),k,1,l),j,1,n),i,1,m);
G17=symsum(symsum(symsum(-d^6*v^2*exp(-lambda(1)-lambda(2)*d^2-
lambda(3)*d^3-lambda(4)*d^3*u-lambda(5)*d^3*v-
lambda(6)*d^3*(u^2+v^2)),k,1,l),j,1,n),i,1,m);
G18=symsum(symsum(symsum(-d^6*v*(v^2+u^2)*exp(-lambda(1)-lambda(2)*d^2-
lambda(3)*d^3-lambda(4)*d^3*u-lambda(5)*d^3*v-
lambda(6)*d^3*(u^2+v^2)),k,1,l),j,1,n),i,1,m);
G19=symsum(symsum(symsum(-d^3*(v^2+u^2)*exp(-lambda(1)-lambda(2)*d^2-
lambda(3)*d^3-lambda(4)*d^3*u-lambda(5)*d^3*v-
lambda(6)*d^3*(u^2+v^2)),k,1,l),j,1,n),i,1,m);
G20=symsum(symsum(symsum(-d^5*(v^2+u^2)*exp(-lambda(1)-lambda(2)*d^2-
lambda(3)*d^3-lambda(4)*d^3*u-lambda(5)*d^3*v-
lambda(6)*d^3*(u^2+v^2)),k,1,l),j,1,n),i,1,m);
G21=symsum(symsum(symsum(-d^6*(v^2+u^2)*exp(-lambda(1)-lambda(2)*d^2-
lambda(3)*d^3-lambda(4)*d^3*u-lambda(5)*d^3*v-
lambda(6)*d^3*(u^2+v^2)),k,1,l),j,1,n),i,1,m);
G22=symsum(symsum(symsum(-d^6*u*(v^2+u^2)*exp(-lambda(1)-lambda(2)*d^2-
lambda(3)*d^3-lambda(4)*d^3*u-lambda(5)*d^3*v-
lambda(6)*d^3*(u^2+v^2)),k,1,l),j,1,n),i,1,m);
G23=symsum(symsum(symsum(-d^6*v*(v^2+u^2)*exp(-lambda(1)-lambda(2)*d^2-
lambda(3)*d^3-lambda(4)*d^3*u-lambda(5)*d^3*v-
lambda(6)*d^3*(u^2+v^2)),k,1,l),j,1,n),i,1,m);
G24=symsum(symsum(symsum(-d^6*(v^2+u^2)^2*exp(-lambda(1)-lambda(2)*d^2-
lambda(3)*d^3-lambda(4)*d^3*u-lambda(5)*d^3*v-
lambda(6)*d^3*(u^2+v^2)),k,1,l),j,1,n),i,1,m);
G25=symsum(symsum(symsum(-d^2*exp(-lambda(1)-lambda(2)*d^2-
lambda(3)*d^3-lambda(4)*d^3*u-lambda(5)*d^3*v-
lambda(6)*d^3*(u^2+v^2)),k,1,l),j,1,n),i,1,m);
G26=symsum(symsum(symsum(-d^4*exp(-lambda(1)-lambda(2)*d^2-
lambda(3)*d^3-lambda(4)*d^3*u-lambda(5)*d^3*v-
lambda(6)*d^3*(u^2+v^2)),k,1,l),j,1,n),i,1,m);
G27=symsum(symsum(symsum(-d^5*exp(-lambda(1)-lambda(2)*d^2-
lambda(3)*d^3-lambda(4)*d^3*u-lambda(5)*d^3*v-
lambda(6)*d^3*(u^2+v^2)),k,1,l),j,1,n),i,1,m);
G28=symsum(symsum(symsum(-d^5*u*exp(-lambda(1)-lambda(2)*d^2-
lambda(3)*d^3-lambda(4)*d^3*u-lambda(5)*d^3*v-
lambda(6)*d^3*(u^2+v^2)),k,1,l),j,1,n),i,1,m);
G29=symsum(symsum(symsum(-d^5*v*exp(-lambda(1)-lambda(2)*d^2-
lambda(3)*d^3-lambda(4)*d^3*u-lambda(5)*d^3*v-
lambda(6)*d^3*(u^2+v^2)),k,1,l),j,1,n),i,1,m);
G30=symsum(symsum(symsum(-d^5*(v^2+u^2)*exp(-lambda(1)-lambda(2)*d^2-
lambda(3)*d^3-lambda(4)*d^3*u-lambda(5)*d^3*v-
lambda(6)*d^3*(u^2+v^2)),k,1,l),j,1,n),i,1,m);
G31=symsum(symsum(symsum(-exp(-lambda(1)-lambda(2)*d^2-lambda(3)*d^3-
lambda(4)*d^3*u-lambda(5)*d^3*v-
lambda(6)*d^3*(u^2+v^2)),k,1,l),j,1,n),i,1,m);
G32=symsum(symsum(symsum(-d^2*exp(-lambda(1)-lambda(2)*d^2-
lambda(3)*d^3-lambda(4)*d^3*u-lambda(5)*d^3*v-
lambda(6)*d^3*(u^2+v^2)),k,1,l),j,1,n),i,1,m);
```

```
G33=symsum(symsum(symsum(-d^3*exp(-lambda(1)-lambda(2)*d^2-
lambda(3)*d^3-lambda(4)*d^3*u-lambda(5)*d^3*v-
lambda(6)*d^3*(u^2+v^2)),k,1,l),j,1,n),i,1,m);
G34=symsum(symsum(symsum(-d^3*u*exp(-lambda(1)-lambda(2)*d^2-
lambda(3)*d^3-lambda(4)*d^3*u-lambda(5)*d^3*v-
lambda(6)*d^3*(u^2+v^2)),k,1,l),j,1,n),i,1,m);
G35=symsum(symsum(symsum(-d^3*v*exp(-lambda(1)-lambda(2)*d^2-
lambda(3)*d^3-lambda(4)*d^3*u-lambda(5)*d^3*v-
lambda(6)*d^3*(u^2+v^2)),k,1,l),j,1,n),i,1,m);
G36=symsum(symsum(symsum(-d^3*(u^2+v^2)*exp(-lambda(1)-lambda(2)*d^2-
lambda(3)*d^3-lambda(4)*d^3*u-lambda(5)*d^3*v-
lambda(6)*d^3*(u^2+v^2)),k,1,l),j,1,n),i,1,m);
J=[G1 G2 G3 G4 G5 G6;G7 G8 G9 G10 G11 G12;G13 G14 G15 G16 G17 G18; G19
G20 G21 G22 G23 G24;G25 G26 G27 G28 G29 G30;G31 G32 G33 G34 G35 G36];

N=300;              %number of iterations
epsilon = 2e-4;     %tolerance
maxval = 10000;     %divergence value
lambda_init=[-3.59;-0.5;0.33;0.46;0.94;-0.48];


while (N>0)

   JJ= eval(subs(J, lambda, lambda_init));
   C=eval(subs(g, lambda, lambda_init));
   C=vpa(C,5);
   lambda_new=lambda_init-inv(JJ)*C;
   lambda_new(1)=ln(symsum(symsum(symsum(exp(-lambda_new(2)*d^2-
lambda_new(3)*d^3-lambda_new(4)*d^3*u-lambda_new(5)*d^3*v-
lambda_new(6)*d^3*(u^2+v^2))*delu*delv*deld,k,1,l),j,1,n),i,1,m));
   lambda_new=subs(lambda_new, lambda_new(1,1), lambda_new(1));
   lambda_new=vpa(lambda_new);
   A=abs(abs(eval(subs(g, lambda, lambda_new)))-abs(eval(subs(g, lambda,
lambda_init))));
   A=vpa(A);

   if A < epsilon
       lambda_init=lambda_new;
       iter = 300-N;
      return;
   end

   if abs(eval(subs(g, lambda, lambda_new)))> maxval
     iter=300-N;
     disp(['iteration= ', num2str(iter)]);
     error ('Solution diverges');
     abort;
  end

    N=N-1;
    lambda_init=lambda_new
    norm(eval(subs(g, lambda, lambda_new)))
```

```
end;
error(' No convergence after iterations.');
abort;
```

%Second Version

```
clc
clear
syms lambda i j k lambda0 lambda1 lambda2 lambda3 lambda4 lambda5
lambda6
lambda=[lambda0;lambda1;lambda2;lambda3;lambda4;lambda5;lambda6];
%initial values

n=5;                    %upper limit for u summation
m=5;                    %upper limit for d summation
l=5;                    %upper limit for v summation
Dmax=3000*10^(-6);
Dmin=50*10^(-6);
D30=750*10^(-6);        %sigma md/M
D32=850*10^(-6);

%-------------------------------------------------------------------------
---

p0= 101325;         %atmospheric pressure
gamma=1.4;          %air gamma
mo=1.794*10^(-3); %water viscosity at 0
sigma=0.07564;      %water surface tension at 0
roa=1.225;          %Air density
row=1025;           %water density
wA=0.58 ;           %Wave amplitude
Lw=2.10 ;           %Wave length
g=9.81;             %gravity acceleration
%Vwave=sqrt(g*Lw/(2*pi))    %Wave Velocity
Vwave=1.80;
K=2*pi/Lw;          %Wavenumber
B=0.31;             %ratio of diameter of liquid regions that enclose air
pocket to diameter of air pocket kw^2/D^2
%not=(-row*(gamma-1)/(2*p0))*(A-1)*(k*wA*Vwave).^2;
fun=@(x) (x/p0).^((gamma-1)/gamma)+(gamma-1)*(x/p0).^(-1/gamma)-gamma-(-
row*(gamma-1)/(2*p0))*(B-1)*(K*wA*Vwave).^2;
x0=[100000 4000000];
pmax=fzero(fun,x0);
ci=5.1;
Umax=(sqrt(pmax/(ci*row)));

%-------------------------------------------------------------------------
---

Umax1=10;
Umin=0;
Vmax=10;
Vmin=0;
```

```
z=20;          %Water sheet breakup degree
%U=2.5;
U0=Umax*cosd(z);
V0=Umax*sind(z);
p=10;                %segmentation of integral to summation for d
q=10;                %segmentation of integral to summation for u
r=10;                %segmentation of integral to summation for v
d=(Dmin+(Dmax-Dmin)*i/p)/D30;
u=(Umin+(Umax1-Umin)*j/q)/U0;
v=(Vmin+(Vmax-Vmin)*k/r)/V0;
uu=Vwave/U0;
vv=Vwave/V0;
delu=(Umax1-Umin)/p;
deld=(Dmax-Dmin)/q;
delv=(Vmax-Vmin)/r;

ln = @log;
T=0.1;

%-------------------------------------------------------------------------

Roa=1.225;
Rol=1025;
Mo=1.794*10^(-3);
L=6;
Rey= Rol*U0*L/Mo;
Rex= Rol*V0*L/Mo;
if Rey > 1e3
    Cdy=1.328/sqrt(Rey);
end
if 1< Rey < 1e3
    Cdy=(1.328/sqrt(Rey))+2.3/Rey;
end
if Rex > 1e3
    Cdx=1.328/sqrt(Rex);
end
if 1< Rex < 1e3
    Cdx=(1.328/sqrt(Rex))+2.3/Rex;
end

%-------------------------------------------------------------------------

b=1.5;
c=2.10;
Lb=L/4;
t=T;
Sm=0;
Smu=(Roa/Rol)*Cdy*0.5*(b+c)*Lb/(b*t);
Smv=(Roa/Rol)*Cdx*0.5*(b+c)*Lb/(b*t);
Ske=3.5;
Ss=D30/D32;
Ss=0.8824;
Kp=1.3;
```

```
%-------------------------------------------------------------------

% First six Functions
f=exp(-lambda(1)-lambda(2)*d^2-lambda(3)*d^3-lambda(4)*d^3*u-
lambda(5)*d^3*v-lambda(6)*d^3*(u^2+v^2)-lambda(7)*d^(-1));
g1=symsum(symsum(symsum(d^3*f*delu*deld*delv,k,1,l),i,1,n),j,1,m)-1-Sm;
g2=symsum(symsum(symsum(d^3*u*f*delu*deld*delv,k,1,l),i,1,n),j,1,m)-uu-
Smu;
g3=symsum(symsum(symsum(d^3*v*f*delu*deld*delv,k,1,l),i,1,n),j,1,m)-vv-
Smv;
g4=symsum(symsum(symsum(d^3*(u^2+v^2)*f*delu*deld*delv,k,1,l),i,1,n),j,1
,m)-uu^2-vv^2-Ske;
g5=symsum(symsum(symsum(d^2*f*delu*deld*delv,k,1,l),i,1,n),j,1,m)-Ss;
g6=symsum(symsum(symsum(f*delu*deld*delv,k,1,l),i,1,n),j,1,m)-1;
g7=symsum(symsum(symsum(d^(-1)*f*delu*deld*delv,k,1,l),i,1,n),j,1,m)-Kp;
g=[g1;g2;g3;g4;g5;g6;g7];

% ---- Jacobian Matrix -------------------------------------------------

G1=symsum(symsum(symsum(-d^3*f,k,1,l),j,1,n),i,1,m);
G2=symsum(symsum(symsum(-d^5*f,k,1,l),j,1,n),i,1,m);
G3=symsum(symsum(symsum(-d^6*f,k,1,l),j,1,n),i,1,m);
G4=symsum(symsum(symsum(-d^6*u*f,k,1,l),j,1,n),i,1,m);
G5=symsum(symsum(symsum(-d^6*v*f,k,1,l),j,1,n),i,1,m);
G6=symsum(symsum(symsum(-d^6*(v^2+u^2)*f,k,1,l),j,1,n),i,1,m);
G7=symsum(symsum(symsum(-d^(-1)*d^3*f,k,1,l),j,1,n),i,1,m);

G8=symsum(symsum(symsum(-d^3*u*f,k,1,l),j,1,n),i,1,m);
G9=symsum(symsum(symsum(-d^5*u*f,k,1,l),j,1,n),i,1,m);
G10=symsum(symsum(symsum(-d^6*u*f,k,1,l),j,1,n),i,1,m);
G11=symsum(symsum(symsum(-d^6*u^2*f,k,1,l),j,1,n),i,1,m);
G12=symsum(symsum(symsum(-d^6*u*v*f,k,1,l),j,1,n),i,1,m);
G13=symsum(symsum(symsum(-d^6*u*(v^2+u^2)*f,k,1,l),j,1,n),i,1,m);
G14=symsum(symsum(symsum(-d^(-1)*d^3*u*f,k,1,l),j,1,n),i,1,m);

G15=symsum(symsum(symsum(-d^3*v*f,k,1,l),j,1,n),i,1,m);
G16=symsum(symsum(symsum(-d^5*v*f,k,1,l),j,1,n),i,1,m);
G17=symsum(symsum(symsum(-d^6*v*f,k,1,l),j,1,n),i,1,m);
G18=symsum(symsum(symsum(-d^6*v*u*f,k,1,l),j,1,n),i,1,m);
G19=symsum(symsum(symsum(-d^6*v^2*f,k,1,l),j,1,n),i,1,m);
G20=symsum(symsum(symsum(-d^6*v*(v^2+u^2)*f,k,1,l),j,1,n),i,1,m);
G21=symsum(symsum(symsum(-d^(-1)*d^3*v*f,k,1,l),j,1,n),i,1,m);

G22=symsum(symsum(symsum(-d^3*(v^2+u^2)*f,k,1,l),j,1,n),i,1,m);
G23=symsum(symsum(symsum(-d^5*(v^2+u^2)*f,k,1,l),j,1,n),i,1,m);
G24=symsum(symsum(symsum(-d^6*(v^2+u^2)*f,k,1,l),j,1,n),i,1,m);
G25=symsum(symsum(symsum(-d^6*u*(v^2+u^2)*f,k,1,l),j,1,n),i,1,m);
G26=symsum(symsum(symsum(-d^6*v*(v^2+u^2)*f,k,1,l),j,1,n),i,1,m);
G27=symsum(symsum(symsum(-d^6*(v^2+u^2)^2*f,k,1,l),j,1,n),i,1,m);
G28=symsum(symsum(symsum(-d^(-1)*d^3*(v^2+u^2)*f,k,1,l),j,1,n),i,1,m);

G29=symsum(symsum(symsum(-d^2*f,k,1,l),j,1,n),i,1,m);
```

```
G30=symsum(symsum(symsum(-d^4*f,k,1,l),j,1,n),i,1,m);
G31=symsum(symsum(symsum(-d^5*f,k,1,l),j,1,n),i,1,m);
G32=symsum(symsum(symsum(-d^5*u*f,k,1,l),j,1,n),i,1,m);
G33=symsum(symsum(symsum(-d^5*v*f,k,1,l),j,1,n),i,1,m);
G34=symsum(symsum(symsum(-d^5*(v^2+u^2)*f,k,1,l),j,1,n),i,1,m);
G35=symsum(symsum(symsum(-d^(-1)*d^2*f,k,1,l),j,1,n),i,1,m);

G36=symsum(symsum(symsum(-f,k,1,l),j,1,n),i,1,m);
G37=symsum(symsum(symsum(-d^2*f,k,1,l),j,1,n),i,1,m);
G38=symsum(symsum(symsum(-d^3*f,k,1,l),j,1,n),i,1,m);
G39=symsum(symsum(symsum(-d^3*u*f,k,1,l),j,1,n),i,1,m);
G40=symsum(symsum(symsum(-d^3*v*f,k,1,l),j,1,n),i,1,m);
G41=symsum(symsum(symsum(-d^3*(u^2+v^2)*f,k,1,l),j,1,n),i,1,m);
G42=symsum(symsum(symsum(-d^(-1)*f,k,1,l),j,1,n),i,1,m);

G43=symsum(symsum(symsum(-d^(-1)*f,k,1,l),j,1,n),i,1,m);
G44=symsum(symsum(symsum(-d^(-1)*d^2*f,k,1,l),j,1,n),i,1,m);
G45=symsum(symsum(symsum(-d^(-1)*d^3*f,k,1,l),j,1,n),i,1,m);
G46=symsum(symsum(symsum(-d^(-1)*d^3*u*f,k,1,l),j,1,n),i,1,m);
G47=symsum(symsum(symsum(-d^(-1)*d^3*v*f,k,1,l),j,1,n),i,1,m);
G48=symsum(symsum(symsum(-d^(-1)*d^3*(u^2+v^2)*f,k,1,l),j,1,n),i,1,m);
G49=symsum(symsum(symsum(-d^(-1)*d^(-1)*f,k,1,l),j,1,n),i,1,m);

J=[G1 G2 G3 G4 G5 G6 G7;G8 G9 G10 G11 G12 G13 G14;G15 G16 G17 G18 G19
G20 G21;G22 G23 G24 G25 G26 G27 G28;G29 G30 G31 G32 G33 G34 G35;G36 G37
G38 G39 G40 G41 G42;G43 G44 G45 G46 G47 G48 G49];

%-------------------------------------------------------------------------

N=50;               %number of iterations
epsilon = 1e-4;     %tolerance
maxval = 10000;     %divergence value
lambda_init=[-0.15;0.15;-0.25;0.48;0.6;-0.2;0.25];

while (N>0)

   JJ= eval(subs(J, lambda, lambda_init));
   C=eval(subs(g, lambda, lambda_init));
   C=vpa(C,5);
   lambda_new=lambda_init-inv(JJ)*C;
   lambda_new(1)=ln(symsum(symsum(symsum(exp(-lambda_new(2)*d^2-
lambda_new(3)*d^3-lambda_new(4)*d^3*u-lambda_new(5)*d^3*v-
lambda_new(6)*d^3*(u^2+v^2)-lambda_new(7)*d^(-
1))*delu*delv*deld,k,1,l),j,1,n),i,1,m));
   lambda_new=subs(lambda_new, lambda_new(1,1), lambda_new(1));
   lambda_new=vpa(lambda_new);
   A=abs(abs(eval(subs(g, lambda, lambda_new)))-abs(eval(subs(g, lambda,
lambda_init))));
   A=vpa(A);

   if A < epsilon
       lambda_init=lambda_new;
       iter = 300-N;
```

```
      return;
   end

   if abs(eval(subs(g, lambda, lambda_new)))> maxval
     iter=300-N;
     disp(['iteration= ', num2str(iter)]);
     error ('Solution diverges');
     abort;
  end

    N=N-1;
    lambda_init=lambda_new
    norm(eval(subs(g, lambda, lambda_new)))

end;
error('No convergence after iterations.');
abort;

clc
clear
%syms v

%Flat plate results
%lambda=[-4.41;0.16;-0.42;0.57;0.86;-0.27;0.30];
%lambda=[-4.40;0.17;-0.43;0.57;0.86;-0.27;0.31];
%lambda=[-4.39;0.17;-0.43;0.57;0.85;-0.27;0.31];

%Large Scale Results
lambda=[-4.42;0.078;-0.46;0.67;1.15;-0.41;0.28];
%lambda=[-4.39;0.06;-0.51;0.73;1.36;-0.54;0.28];
%lambda=[-4.39;0.5;-0.53;0.74;1.42;-0.56;0.28];
%lambda=[-4.36;0.05;-0.53;0.78;1.49;-0.62;0.28];

%Sensitivity 1
%lambda=[-4.41;0.16;-0.42;0.57;0.86;-0.27;0.30];
%lambda=[-4.51;0.26;-0.46;0.57;0.86;-0.27;0.34];
%lambda=[-4.61;0.36;-0.50;0.57;0.86;-0.27;0.38];
%lambda=[-4.78;0.52;-0.56;0.57;0.85;-0.27;0.45];

%Sensivtiity 2
%lambda=[-4.41;0.16;-0.42;0.57;0.86;-0.27;0.30];
%lambda=[-4.12;-0.09;-0.32;0.57;0.86;-0.27;0.18];
%lambda=[-4.56;0.29;-0.47;0.57;0.86;-0.27;0.36];
%lambda=[-4.27;0.03;-0.37;0.57;0.86;-0.27;0.24];

%Sensitivity 3
%lambda=[-4.41;0.16;-0.42;0.57;0.86;-0.27;0.30];
%lambda=[-4.40;0.13;-0.44;0.59;0.91;-0.28;0.30];
%lambda=[-4.36;0.07;-0.47;0.62;1.00;-0.31;0.29];
%lambda=[-4.34;0.04;-0.48;0.63;1.05;-0.32;0.28];

ln = @log;
```

```
d=linspace(0,2);
u=linspace(0,3);
v=linspace(0,3);
%v=2;
[d,u]=meshgrid(d,u);
f=exp(-lambda(1)-lambda(2).*d.^2-lambda(3).*d.^3-lambda(4).*d.^3.*u-
lambda(5).*d.^3.*v-lambda(6).*(u.^2+v.^2)-lambda(7).*d.^(-1));
figure
mesh(u,d,f)
%figure
%scatter3(d,u,f)
%ax=gca;
%cb = colorbar;                % create and label the colorbar
%cb.Label.String = 'Droplet Diameter';
%figure
%plot(u,f)
%axis([0 2 0 1])
%F=max(f);
%D=max(d);
%figure
%plot(u,F)
%axis([0 3 0 3.5e4])
```

%Graphs

```
lambda=[3.6529;2.1035;-3.0007;1.2549];
vmax=3.65;
vmin=1.15;
D30=0.000537;         %sigma md/M
U0=2.2;
Ro=998.2;              %fluid density
sigma=0.0736;
We=Ro*U0^2*D30/sigma;  %weber number
B=12/We;
d=0:0.01:4
A=(vmax+lambda(3)/(2*lambda(4)))*(lambda(4)*d.^3).^0.5;
B=(vmin+lambda(3)/(2*lambda(4)))*(lambda(4)*d.^3).^0.5;
%AA=erf(A)
%BB=erf(B)
x=(3/2).*(pi.*d/lambda(4)).^0.5.*(erf(A)-erf(B)).*exp(-lambda(1)-
lambda(4).*B.*d.^2-[lambda(2)-(lambda(3).^2/(4.*lambda(4)))].*d.^3);
plot(d,x)
```

Analytical Approach Code

```
clc
clear
syms K towb rown
p0= 101325;       %atmospheric pressure
gamma=1.4;        %air gamma
mo=1.787*10^(-3); %water viscosity at 0
sigma=0.07564;    %water surface tension at 0
roa=1.225;        %Air density
```

```
row=1025;         %water density
wA=2.5;           %Wave amplitude
Lw=1  ;           %Wave lenght
g=9.81;           %gravity acceleration
Vwave=sqrt(g*Lw/(2*pi))    %Wave Velocity
k=2*pi/Lw;        %Wavenumber
A=0.31;           %ratio of diameter of liquid regions that enclose air
pocket to diameter of air pocket kw^2/D^2
%--------------------------------
fun=@(x) (x/p0).^((gamma-1)/gamma)+(gamma-1)*(x/p0).^(-1/gamma)-gamma-(-
row*(gamma-1)/(2*p0))*(A-1)*(k*wA*Vwave).^2;
x0=[100000 50000000];
pmax=fzero(fun,x0)
%--------------------------------
%a=0.5;
%d=4;
%i=90;
%C=a^2*(coth(d)+a*cos(i))^2*cos(i)+(9/16)*a^2*((coth(d))^2-
1)^2*((coth(d))^2+1)^2+a^2*(1+coth(d)*a*cos(i))^2*(sin(i))^2+(9/4)*a^2*(
coth(d))^2*sin(2*i)^2*((coth(d))^2-1)^2;
%fun=@(x) (x/p0).^((gamma-1)/gamma)+(gamma-1)*(x/p0).^(-1/gamma)-gamma-
(2.5)*row*(gamma-1)*C/p0;
%x0=[100000 50000000];
%plot(x, fun)
%pmax=fzero(fun,x0)

ci=5.1;
Umax=sqrt(pmax/(ci*row));

W= 0.2 ;          %impact width
town=0.5;         %thickness of sheet at the moment of impact
K=(town*W/2);     %Spray parameter

%Umax=5;
Dl=0.9614*[K^2*sigma^2/(roa*row*Umax^4)]^(1/6)*[1+2.6*mo*(K*roa^4*Umax^7
/(72*row^2*sigma^5))^(1/3)]^(1/5);
dd=1.8093*[K^2*sigma^2/(roa*row*Umax^4)]^(1/6)*[1+2.6*mo*(K*roa^4*Umax^7
/(72*row^2*sigma^5))^(1/3)]^(1/5)*[1+3*mo/(row*sigma*Dl)^(1/2)]^(1/6)
%fplot(@(K)
1.8093*[K^2*sigma^2/(roa*row*Umax^4)]^(1/6)*[1+2.6*mo*(K*roa^4*Umax^7/(7
2*row^2*sigma^5))^(1/3)]^(1/5)*[1+3*mo/(row*sigma*Dl)^(1/2)]^(1/6),
[[1e-08 5e-04]])

%epsilon=0.8;
%tow=0.02;
%k0=epsilon*tow;
%E= 0.5; %ln(h/h0) empirically
%towb=[1/(2*E^2)]^(1/3)*[k0*roa^2*Umax^2/(row*sigma)]^(1/3); %breakup
thickness

%W= 0.7 ;          %impact width
%town=0.5;         %thickness of sheet at the moment of impact
%K=(town*W/2);     %Spray parameter
```

```
%DlD=0.9614*[K^2*sigma^2/(row*roa*Umax^4)]^(1/6)*[1+2.6*mo*(K*roa^4*Umax
^7/(72*row^2*sigma*5))^(1/3)]^(1/5) %Ligament diameter
%figure
%fplot(@(W)
0.9614*[(((town*W/4)*0.001)^2*sigma^2/(row*roa*Umax^4)]^(1/6)*[1+2.6*mo*(
((town*W/4)*0.001)*roa^4*Umax^7/(72*row^2*sigma*5))^(1/3)]^(1/5), [0 5])
%hold on
%town=0.075;
%fplot(@(W)
0.9614*[(((town*W/4)*0.001)^2*sigma^2/(row*roa*Umax^4)]^(1/6)*[1+2.6*mo*(
((town*W/4)*0.001)*roa^4*Umax^7/(72*row^2*sigma*5))^(1/3)]^(1/5), [0 5])
%hold on
%town=0.10;
%fplot(@(W)
0.9614*[(((town*W/4)*0.001)^2*sigma^2/(row*roa*Umax^4)]^(1/6)*[1+2.6*mo*(
((town*W/4)*0.001)*roa^4*Umax^7/(72*row^2*sigma*5))^(1/3)]^(1/5), [0 5])
%hold on
%town=0.15;
%fplot(@(W)
0.9614*[(((town*W/4)*0.001)^2*sigma^2/(row*roa*Umax^4)]^(1/6)*[1+2.6*mo*(
((town*W/4)*0.001)*roa^4*Umax^7/(72*row^2*sigma*5))^(1/3)]^(1/5), [0 5])
%hold on
%town=0.20;
%fplot(@(W)
0.9614*[(((town*W/4)*0.001)^2*sigma^2/(row*roa*Umax^4)]^(1/6)*[1+2.6*mo*(
((town*W/4)*0.001)*roa^4*Umax^7/(72*row^2*sigma*5))^(1/3)]^(1/5), [0 5])

%figure
%W=0.25;
%fplot(@(town)
0.9614*[(((town*W/4)*0.001)^2*sigma^2/(row*roa*Umax^4)]^(1/6)*[1+2.6*mo*(
(town*W/2)*roa^4*Umax^7/(72*row^2*sigma*5))^(1/3)]^(1/5), [0 0.3])
%hold on
%W=0.5;
%fplot(@(town)
0.9614*[(((town*W/4)*0.001)^2*sigma^2/(row*roa*Umax^4)]^(1/6)*[1+2.6*mo*(
(town*W/2)*roa^4*Umax^7/(72*row^2*sigma*5))^(1/3)]^(1/5), [0 0.3])
%hold on
%W=1;
%fplot(@(town)
0.9614*[(((town*W/4)*0.001)^2*sigma^2/(row*roa*Umax^4)]^(1/6)*[1+2.6*mo*(
(town*W/2)*roa^4*Umax^7/(72*row^2*sigma*5))^(1/3)]^(1/5), [0 0.3])
%hold on
%W=2;
%fplot(@(town)
0.9614*[(town*W/2)^2*sigma^2/(row*roa*Umax^4)]^(1/6)*[1+2.6*mo*((town*W/
2)*roa^4*Umax^7/(72*row^2*sigma*5))^(1/3)]^(1/5), [0 0.3])
%hold on
%W=3;
%fplot(@(town)
0.9614*[(town*W/2)^2*sigma^2/(row*roa*Umax^4)]^(1/6)*[1+2.6*mo*((town*W/
2)*roa^4*Umax^7/(72*row^2*sigma*5))^(1/3)]^(1/5), [0 0.3])
%hold on
```

```
%town=4;
%fplot(@(town)
0.9614*[(town*W/2)^2*sigma^2/(row*roa*Umax^4)]^(1/6)*[1+2.6*mo*((town*W/
2)*roa^4*Umax^7/(72*row^2*sigma*5))^(1/3)]^(1/5), [0 0.3])

%W= 1 ;          %impact width
%town=0.1;       %thickness of sheet at the moment of impact
%K=(town*W/4)*0.001;    %Spray parameter
%DlD=0.9614*[K^2*sigma^2/(row*roa*Umax^4)]^(1/6)*[1+2.6*mo*(K*roa^4*Umax
^7/(72*row^2*sigma*5))^(1/3)]^(1/5) %Ligament diameter
%DdD=[3*pi/sqrt(2)]^(1/3)*DlD*[1+3*mo/(row*sigma*DlD)^(1/2)]^(1/6)
%subs([3*pi/sqrt(2)]^(1/3)*DlD*[1+3*mo/(row*sigma*DlD)^(1/2)]^(1/6),
DlD);
%fplot(@(K) DlD, [-0.5, 0.5])
%DdF=0.9614*[K^2*sigma^2/(row*roa*Umax^4)]^(1/6)

%hold on
%W=0.7
%fplot(@(towb)
0.9614*[(towb*W/2)^2*sigma^2/(row*roa*Umax^4)]^(1/6)*[1+2.6*mo*((towb*W/
2)*roa^4*Umax^7/(72*row^2*sigma*5))^(1/3)]^(1/5), [0 5])
```